

Syracuse University

SURFACE at Syracuse University

Dissertations - ALL

SURFACE at Syracuse University

Winter 12-22-2021

Utilizing Parity Violating Electron Scattering As a Probe to Measure the Neutron Radius of 208-pb

David Eric King
Syracuse University

Follow this and additional works at: <https://surface.syr.edu/etd>



Part of the [Nuclear Commons](#)

Recommended Citation

King, David Eric, "Utilizing Parity Violating Electron Scattering As a Probe to Measure the Neutron Radius of 208-pb" (2021). *Dissertations - ALL*. 1464.

<https://surface.syr.edu/etd/1464>

This Dissertation is brought to you for free and open access by the SURFACE at Syracuse University at SURFACE at Syracuse University. It has been accepted for inclusion in Dissertations - ALL by an authorized administrator of SURFACE at Syracuse University. For more information, please contact surface@syr.edu.

Abstract

The Lead Radius Experiment 2 (PREX-II) and Calcium Radius Experiment (CREX) carried out in Hall A of the Thomas Jefferson National Accelerator Facility were designed to measure the neutron skins of ^{208}Pb and ^{48}Ca nuclei by measuring the parity-violating asymmetry A_{PV} of the elastic scattering of polarized electrons on ^{208}Pb and ^{48}Ca targets. In order to achieve a precision measurement of the neutron skins of ^{208}Pb and ^{48}Ca it is imperative to maintain precise control over many experimental parameters—one of which is a precision measurement of the electron beam polarization (which is the largest contributor to experimental error making control a high priority). The results of the Møller polarimetry measurements taken over the PREX-II experiment averaged $89.7\% \pm 0.1\%$ (stat) $\pm 0.89\%$ (syst) while results from the CREX experiment were in remarkable agreement with the Compton Polarimetry results. The PREX-II experimental results returned an $A_{PV} = 550 \pm 16$ (stat) ± 8 (sys) ppb corresponding to a ^{208}Pb neutron skin thickness of 0.283 ± 0.071 fm.

This dissertation will detail the author's work towards ensuring precision Møller polarimetry measurements for the PREX-II and CREX experiments, a review of associated systematics, and Møller polarimetry analysis results for PREX-II and CREX. A brief review of the PREX-II general experimental analysis and results are also provided as well as additional work done in the development efforts for the anticipated future SoLID experiments.

Utilizing Parity Violating Electron Scattering as a
Probe to Measure the Neutron Radius of ^{208}Pb

by

D. Eric King Jr.

B.S., Stockton University, 2013

M.S., Stockton University, 2015

Dissertation

Submitted in partial fulfillment of the requirements for the degree of
Doctor of Philosophy in Physics

Syracuse University

December 2021

Copyright © D. Eric King Jr., 2021

All Rights Reserved

Acknowledgements

I'd like to thank my advisor Dr. Paul Souder for giving me the incredible opportunity to work with him and learn from him. I am extremely grateful for the advice and guidance he has given to me on the path to becoming a researcher as well as the positive environment which he maintains while doing so—the value of which cannot be understated in a world so often full of harsh pressures and negativity. I will feel forever indebted to him. Of course, Paul is but the latest critical waypoint in the journey that is my life.

My family is my bedrock and has helped build the foundation for who I am today. I'm profoundly lucky to have come from a family of who have always believed in me and have always encouraged me to do more. Without the love and support of my family, over the course of my entire life, I would never had the confidence to make the next step. I'm thankful for mother and father listening to my myriad of complaints over the past few years and always offering positive encouragement and for the daily phone calls and laughs with my mother who made the more trying moments of this journey more tolerable. My sister has always thoroughly encouraged me to push the envelope every time I suggested that I wanted to do more than I was; whenever I need her, she has always been there for me. I'm hopeful that my example of pushing myself to do more will have an impact on my niece who I believe has so much potential.

I also need to acknowledge Simona Malace for her guidance and suggestions during my time at JLab along with the invaluable laughs that made bad days good days, and Donald Jones for his guidance, suggestions, assistance and kindness in our working group which has been invaluable over the past few years.

This work is funded in part by the United States Department of Energy (DOE) under grant DE-FG02-84ER40146.

The results of all simulation computational work contained in this thesis was performed on the Syracuse University HTC Grid and funded in part by NSF award ACI-1341006.

Contents

Abstract	i
Acknowledgements	iv
1 Introduction	1
1.1 The Atomic Nucleus	1
1.2 Nuclear Decay	3
1.3 Parity Symmetry	4
1.4 Parity Violation	5
1.5 The Weak Force	7
1.6 The Standard Model	9
1.7 Measuring the Atomic Nucleus	10
1.7.1 Utilizing Parity Violation	11
1.8 Particle Scattering	12
1.9 Elastic Scattering	13
1.10 Form Factors	13
1.11 Helicity	15

1.12	Parity-violating Asymmetry	16
1.13	Extracting the Neutron Skin	19
1.14	Motivation for Measuring the Neutron Skin	20
2	Lab and Experimental Design	23
2.1	CEBAF	23
2.1.1	Linacs	24
2.1.2	Arcs	24
2.1.3	Polarized Electron Source	25
2.1.4	Helicity Control	26
	Pockels Cell	26
	Half-wave Plate	27
	Wien Filter	27
	Unwanted Helicity-Correlated Beam Effects	28
	PITA Effect	28
2.1.5	Beam Position Monitors	29
2.1.6	Wire Scanners / Harps	30
2.1.7	Energy Measurements	31
2.1.8	Beam Current Monitors	31
2.1.9	Charge Feedback System	32
2.1.10	Fast Feedback System	32
2.1.11	Mott Polarimeter	33
2.2	Hall A	34

2.2.1	Compton Polarimeter	34
2.2.2	Møller Polarimeter	36
2.2.3	Rasterization	36
2.2.4	Hall A High Resolution Spectrometer (HRS)	36
2.2.5	Data Acquisition Systems	37
2.2.6	Beam Modulation Coils / Energy Vernier / Dithering	37
2.3	PREX/CREX Specific Experimental Equipment	38
2.3.1	PREX-II/CREX Targets	39
2.3.2	Collimation and Sieve	39
2.3.3	Septum	40
2.3.4	Quartz Detectors	40
3	Møller Polarimetry	44
3.1	JLab Hall-A Møller Polarimeter	45
3.1.1	Helmholtz Holding Field	45
3.1.2	Quadrupoles	46
3.1.3	Møller Dipole	46
3.1.4	Møller Detector	47
3.2	Møller Scattering Physics	48
3.2.1	The Levchuk Effect	53
3.3	Møller Polarimetry	55
3.4	Hall-A Møller Polarimetry Simulation	55
3.4.1	Møller Generator	56

3.4.2	Transport	57
3.5	Calculating Analyzing Power	57
3.6	Møller Polarimetry Optics	58
3.6.1	PREX-II Optics	59
3.6.2	CREX Optics	66
3.7	Optics Summary	67
4	Møller Polarimetry Results	70
4.1	Møller Data Taking	70
4.2	Statistical Goals	71
4.3	MOLANA	73
4.4	Møller Data Analysis	75
4.4.1	Accidentals	75
4.4.2	Charge Normalization and BCM Pedestal	76
	Pedestal Measurements During PREX-II and CREX	76
4.4.3	Dead Time	78
	Determining the Dead Time Constant	79
4.4.4	Data Cuts	81
4.5	Validating Møller Analysis Corrections	82
4.5.1	Dead Time Correction Analytic Expectation	83
	Deadtime Calculated v. Analytic Expectation	84
4.5.2	Charge Normalization and Pedestal Subtraction	85
	Charge Corrections Validation	87

4.5.3	Accidental Correction	87
	Accidental Correction Validation	89
4.6	Spin Dances	89
4.7	Møller Polarimetry Results	90
4.7.1	PREX-II	91
	Half-wave Plate State Difference	91
	4 μ m Fe Foil Irregularity	92
	Final Polarization Values	95
4.7.2	CREX	97
	Overall Møller-to-Compton Comparison	98
4.8	Møller Polarimetry Systematics	102
4.8.1	Analyzing Power Systematics	102
	Quad 1 Sensitivity	102
	PREX-II Q1 Sensitivity	102
	Quad 2/4 Sensitivity	103
	Dipole Sensitivity	105
	Levchuk / Radiative Model Uncertainty	108
	Beam Orbit Studies	110
	Lead Block Bleedover	111
	Phi Acceptance	112
4.8.2	General Systematics	113
	Deadtime	114

Bleed through	114
dP/P (Spin Precession)	115
Accidentals	116
Charge Normalization	117
Slit Dependence	118
Current Dependence a.k.a. High Current Extrapolation	119
Null Asymmetry	120
PITA Variation	120
July Running	122
4.8.3 Systematics Summary	122
5 PREX-II Experimental Results	126
5.1 Scattering Angle Determination	126
5.1.1 Water Cell	126
5.1.2 Sieve Calibration	127
5.1.3 Central Angle Results	127
5.2 Q^2 measurements	128
5.3 Raw Detector Asymmetry	129
5.4 Beam Asymmetry Correction	129
5.5 Beam Polarization Measurement	130
5.6 Transverse Asymmetry Measurement	130
5.7 Target Diamond Coating	131
5.8 Acceptance Function	132

5.9	A_{PV} Corrections Summary	133
5.10	PREX-II Experimental Result	134
5.11	Experimental Impact on Physics	135
6	Discussion	137
6.1	Møller Polarimetry	137
6.2	Neutron Skin Measurements	139
7	GEM Alignment for SoLID	141
7.1	SoLID Spectrometer	142
7.1.1	Description	142
7.1.2	Gaseous Electron Multiplier Detectors	143
7.1.3	Measurement of the Momentum of the Scattered Electron	143
7.2	GEM Calibration Method	144
7.3	Sources of Photons and their Energy Spectra	145
7.4	Signals in the GEM's from the Photons	146
7.5	Spatial Distribution of Photons in a Pencil Beam	147
7.6	Collimator Design	148
7.7	Results	150
8	Conclusion	155
8.1	Møller Polarimetry	155
8.2	Neutron Skin Measurements	157
A	Polarization Data Summaries	159

A.1	PREX-II Spin Dance Results	159
A.2	CREX Spin Dance Results	160
A.3	PREX-II Cu Foil Measurements	160
A.4	CREX Cu Foil Measurements	160
A.5	Foil Jogging Study	161
A.6	PREX-II Asymmetry Scan	161
A.7	CREX Asymmetry Scan	162
A.8	PREX-II Beam Polarization Measurements	162
A.9	CREX Beam Polarization Measurements	163
Bibliography		164
	Cited References	164

List of Figures

1.1	Depiction of the Wu experiment and parity violation. On the left, the experiment with performed in the “original coordinate” system where Cobalt atoms are aligned in magnetic field caused by passing of current through solenoid wires (in this case in the downward direction on the page). On the right, we have the “mirrored” coordinate system; the magnetic fields passing through the solenoid coils would be opposite that of the original coordinate system so in an experimental setting reversing the current and field through the coils has the same effect as a parity inversion. If parity were respected the the direction of beta emission would have been the same. This was the first strong evidence that the weak force violated parity. <i>Image from Wikimedia Commons [17]</i>	6
1.2	The Standard Model showing the three generations (I, II, III) of quarks and leptons, the gluons (there are actually 8 flavors), the photon, the Z_0 and W_{\pm} bosons and the Higgs. <i>Image from Wikimedia Commons [28]</i>	10
1.3	A comparison of charge distribution density functions and their corresponding form factors for a variety of charge distributions.	15
1.4	Helicity/Particle-Handedness of particles with particular spin and direction of travel. A negative helicity (left-handedness) occurs when spin direction and momentum directions are anti-parallel and a positive helicity (right-handedness) occurs when spin direction and momentum direction are parallel.	16
1.5	Feynman diagrams for electron-nucleon scattering for photon and Z_0 interaction.	17

1.6	The relationship of the (a) neutron skin R_{np} and parity-violating asymmetry A_{PV} , and (b) nuclear symmetry energy L and A_{PV} for various nuclear EOS with a linear regression fit over all models to show relationships. Figures adopted with permission from [44].	22
2.1	Mock-up of the Jefferson Lab Accelerator.	24
2.2	Mock up of polarized electron production within the photocathode. σ^+ and σ^- are left and right circularly polarized electrons which come into contact with the photocathode which have spin states ± 1 . The energy gap E_g is 1.52 eV while the spin-orbit splitting Δ_{so} is 0.34 eV. In this arrangement care must be taken such that the source laser energy exceeds the energy gap E_g but avoids excitement of the $p_{1/2}$ band. Figure adapted from [46].	25
2.3	Rapid helicity control. Applied changes to the Pockels cell voltage, idealized here as a square wave, result in changes to photon polarization which results in changes to electron helicity.	27
2.4	Diagram of Jefferson Lab Hall A Compton Polarimeter. Two dipoles D1 and D2 divert the electron beam from the main beam line to the laser table optics cavity. Dipoles D3 and D4 return the electron beam back to the main beam line. Compton back-scattered photons are detected at the photon detector while Compton scattered electrons are detected at the Electron detector.	34
2.5	Basic Schematic of PREX/CREX Setup. (Not drawn to scale.)	38
2.6	Post-experiment photo of PREX-II ^{208}Pb targets. Left-target shows signs of minor thermal wear in the shape of the raster. Right-target shows a target which reached thermal failure.	40

2.7	Schematic of PREX-II setup prior to electron scatters entering into the first HRS quadrupoles. The electron beam (blue dashed line) strikes the target; scattered beam electrons (denoted by dark blue bands) potentially pass through the sieve and are collimated prior to entering the septum which bends the electrons, selected for an $\approx 5^\circ$ scattering angle, outwards to accommodate the minimum separation angle of the HRS system $\approx 12^\circ$	41
2.8	Basic Schematic of PREX/CREX experimental apparatus with visualization of the target arms containing the main target ladder and optics target ladder.	41
2.9	Left panel: Basic CAD schematic of the sieve/collimator component of the PREX-II/CREX experiment. Sieve plates can be rotated in and out of the scattered beam as necessary to aid in event reconstruction. Right-panel: Photo of sieve/collimator apparatus.	42
2.10	Images of PREX-II/CREX integrating detectors. Silicon light guides are attached to orange-colored PMTs. [Images courtesy of Dustin McNulty].	43
3.1	Mock up of the Jefferson Lab Hall A Møller polarimeter (not drawn to scale).	45
3.2	The Jefferson Lab Hall-A Møller polarimeter detector. The detector is contained in a shielded box (lead bricks filling box not shown) to protect it from backgrounds. Electrons successfully transported through the spectrometer enter through the box window, strike the lead-fiber bricks (yellow, actually composed of four blocks) and scintillation light is collected by eight PMTs (green).	47
3.3	Møller polarimeter high-voltage control panel GUI with PMT selection settings for CREX optics which utilized the lower 6PMTs.	49
3.4	Møller polarimeter PMT signals from ADC data. High-voltage for the PMTs are individually set in order to align the Møller peaks to the same channel (here 300).	49
3.5	Left arm and right arm PMT signal sums. Threshold cuts set at channel 180.	50

3.6	Møller scattering Feynman tree-level diagrams. Both t-channel and u-channel are required since we have two identical fermions scattering. Both γ and Z_0 interactions are shown for completeness although the weak Z_0 contribution is negligible compared to γ contribution.	50
3.7	Møller scattering diagrams. Left-panel: center-of-mass representation; Right-panel: laboratory frame representation.	51
3.8	Møller analyzing powers A_{zz}, A_{xx} and A_{yy} plotted as a function of θ^* . The analyzing powers reach maximum value when the center-of-mass scattering angle is 90° . A_{zz} maxes out at $\frac{7}{9}$ while the A_{xx} and A_{yy} components max out at $\pm\frac{1}{9}$	52
3.9	Rendering of Hall-A Møller Polarimeter in MOLPOL.	56
3.10	Disfavored 8PMT PREX-II Q1 asymmetry and rate scan. Vertical axis marks the detuning of the Q1 magnet in percent. Horizontal axis bars represent a 0.25% change off of the uncorrected analyzing power (blue line) at the point marked 0% detuning. It can be seen that corrected analyzing power (orange line) is not flat which is not optimal. The difference between the orange and blue lines is primarily due to the Levchuk effect.	59
3.11	MolPol cemetery scatter plot sample image of PREX-II 8 PMT optics solution run with Geant4 performing transportation only without any scattering effects for the electron which traveled down the right arm of the polarimeter. Axes represent the θ_{COM} and ϕ_{COM} generated in the MolPol monte carlo. Scatter plot is colored by region in which Møller electron was last detected passing through a flux plane. Regions are marked in text on scatter plot for clarity.	60

3.12	<p><i>Top panel:</i> MolPol cemetery scatter plot of PREX-II 8 PMT optics solution at rate maximum with the Levchuk effect turned in the Møller electron generator. Green scatter plot points are electrons which received a Levchuk angle modification large enough to cause them to collide with the outer wall of the dipole box. <i>Bottom panel:</i> Highlighted location on PREX-II 8 PMT optics asymmetry curve.</p>	61
3.13	<p><i>Top panel:</i> MolPol cemetery scatter plot of PREX-II 8 PMT optics solution at a magnet setting $\approx 3\%$ over-tuned from rate maximum with the Levchuk effect turned in the Møller electron generator. Green scatter plot points are electrons which received a Levchuk angle modification large enough to cause them to collide with the outer wall of the dipole box. <i>Bottom panel:</i> Highlighted location on PREX-II 8 PMT optics asymmetry scan curve.</p>	62
3.14	<p>Disfavored PREX-II 8 PMT optics solution—Left panel: Coincidence and single hits overlay; Middle panel: Intensity of coincidence hits on detector; Right panel: Uncorrected analyzing power. The dashed lines on the left and center panels indicate individual PMT domains.</p>	64
3.15	<p>Favored PREX-II 2 PMT optics solution. <i>Left panel:</i> Coincidence and single hits overlay; <i>Center panel</i> Intensity of coincidence hits on detector; <i>Right panel:</i> Uncorrected analyzing power. The dashed lines on the left and center panels indicate individual PMT domains.</p>	64
3.16	<p>PREX-II Q1 asymmetry and rate scan utilizing only two of the photomultiplier tubes of the detector. Horizontal bars represent a 0.25% change off of the uncorrected analyzing power at 0% detuning. It can be seen that at our optimal tuning point the analyzing power is essentially flat and correction to the analyzing power is around -0.1%.</p>	66

3.17	PREX-II dipole asymmetry and rate scan utilizing only two of the photomultiplier tubes. Horizontal bars represent a 0.25% change in analyzing power off of the uncorrected analyzing power at the 0% detuning position.	67
3.18	CREX optics utilizing all 8 PMTs of the Møller detector. Limited region of flat analyzing power made this a non-ideal solution.	68
3.19	CREX optics utilizing only six PMTs of the Møller detector. Reduction of active detector area results in a large flat region of analyzing power with respect to quadrupole tuning making it an ideal optics solution.	68
3.20	CREX 6PMT optics solution—Left panel: Coincidence and single hits overlay; Middle panel: Intensity of coincidence hits on detector; Right panel: Uncorrected analyzing power.	68
3.21	CREX dipole scan simulation results. Dipole has region of relatively flat rate that corresponds to region of flat analyzing power.	69
4.1	Asymmetry data of Group 1071 taken on 4 μ m foil during the PREX-II experiment. Measurements including beam down time and small gaps in between individual runs (25 in total here at a helicity-flip frequency of 240 Hz) typically took on the order of 60 minutes.	72
4.2	Asymmetry data of Group 3046 taken during the CREX experiment. Measurements including beam down time and small gaps in between individual runs (6 runs in total here at a helicity-flip frequency of 120 Hz) typically took on the order of 20 minutes.	72
4.3	MOLANA data analysis chain.	74
4.4	Pedestal data obtained during PREX-II Møller polarimetry measurements.	77
4.5	Pedestal data obtained during CREX Møller polarimetry measurements.	77

4.6	Deadtime measurements during the PREX-II experiment used to determine the dead time constant of the detector package.	80
4.7	Comparison of computed dead time correction vs. analytic expectation for the dead time correction PREX-II and CREX. Each point represents the correction made to an individual Møller data run.	85
4.8	Comparison of computed correction vs. analytic expectation for PREX-II and CREX charge asymmetry and pedestal corrections. Each point represents a single Møller polarimetry data run. The fit shown is for a first order polynomial as we should see a one-to-one relationship between the quantities.	87
4.9	Comparison of computed correction vs. analytic expectation for PREX-II and CREX accidental corrections. Each point represents a single Møller polarimetry data run. The fit shown is for a first order polynomial as we should see a one-to-one relationship between the quantities. The analytically expected and computed corrections are consistent indicating the the implementation of the accidental correction in the new analysis code is correct.	89
4.10	Graphical summary of PREX-II and CREX spin dance measurements taken. Polarization values with statistical errors (calculated from the analysis software written by the author) are are fit to a cosine curve in ROOT $f(\theta) = x_1 \cos(\theta - x_2)$	90
4.11	All taken PREX-II Møller polarimetry measurements organized by Møller polarimetry Group number.	91
4.12	ompton polarimetry measurements separated by iHWP state and Wien flip state. For the purpose of comparing polarimetry measurements the Compton polarimeter results suggested that the HWP-IN/HWP-OUT difference seen by the Møller polarimeter was real with a statistical significance of $\approx 2.5\sigma$. [Compton data plot courtesy of Allison Zec.]	93

4.13	Mott polarimeter measurements taken on 9/5/2019 verified with reasonable precision that the HWP-IN/HWP-OUT difference first noticed by Møller polarimetry was real and not statistical in nature.	93
4.14	PREX-II Møller sign-corrected polarimetry measurements taken on the $4\mu m$ iron foil separated by half-wave plate state and wien filter state. The error-weighted data was fit with a zeroth-order polynomial to arrive at average polarizations for each half-wave plate state across both Wien filter configurations.	94
4.15	PREX-II Møller sign-corrected polarimetry measurements taken on the $10\mu m$ iron foil separated by half-wave plate state. The error-weighted data was fit with a zeroth-order polynomial to arrive at average polarizations for each wave state.	94
4.16	Polarization measurements made during foil jogging systematics studies on $4\mu m$ and $10\mu m$ foils demonstrating possible inconsistency with measurements taken on the $4\mu m$ foil. Polarization values for the above plot are located in section A.5.	94
4.17	PREX-II sign-corrected polarimetry data taken on the $4\mu m$ and $10\mu m$ foils in the HWP-IN state. The error-weighted data were fit with a zeroth-order polynomial to capture a mean polarization. A difference of $\approx 1\%$ is demonstrated.	96
4.18	PREX-II sign-corrected polarimetry data taken on the $4\mu m$ and $10\mu m$ foils in the HWP-OUT state. The error-weighted data were fit with a zeroth-order polynomial to capture a mean polarization. A difference of $\approx 1\%$ is demonstrated.	96
4.19	Photo of $4\mu m$ foil taken after the PREX-II experiment had concluded. Foil wrinkling is clearly visible.	96
4.20	Photo of $10\mu m$ foil taken after the PREX-II experiment had concluded. Foil appears to be in excellent shape.	96

4.21	10 μm -to-4 μm foil polarization ratios from data which was taken consecutively. Ratios were error weighted and the errors propagated. The error-weighted ratio data was then fit to a zeroth-order polynomial to get a conversion ratio for days which there was no 10 μm foil measurements.	97
4.22	Final PREX-II Møller polarimetry results.	97
4.23	Overlay of measurements made by the Compton Polarimeter and Møller polarimeter during the period before the COVID shutdown.	100
4.24	Overlay of measurements made by the Compton Polarimeter and Møller polarimeter during the period after the COVID shutdown. First Møller polarimetry measurements	100
4.25	Comparison of Møller polarimetry measurements against error-weighted averages of any Compton polarimetry 'snails' which concluded in a ± 2 day period around the Møller measurements; there are a total of 10 Møller measurements which had associated Compton measurements. This comparison data was then averaged across half-wave plate states over the course of the whole experiment, over pre-COVID measurements only and post-COVID measurements only. Averages are plotted as constant lines are bounded by 1σ error bars which are lightly shaded.	101
4.26	Ratios of Møller polarimetry measurements and error-weighted averages of any Compton polarimetry 'snails' which concluded in a ± 2 day period around the Møller measurements; there are a total of 10 Møller measurements which had associated Compton measurements. Compton-to-Møller ratios were taken from the available 10 pairs of data points. The mean Compton-to-Møller ratio was 0.9995 ± 0.0008	101

4.27	PREX-II dipole rate scan summary. Each point was an individual run. Run was fit with second-order polynomials immediately after data was being taken to provide guidance on locating rate maximum. Black band is predicted simulation curve shifted by 0.7A to line up average dipole scan peaks.	105
4.28	Fits of PREX-II dipole rate scans. A summary of this fit data can be seen in table 4.7. Møller coincidence rates are normalized to the recorded BCM recorded charge rate adjusted for pedestal. This data was utilized to place a limit on how well the rate peak was identified for the purpose of setting a systematic. . . .	107
4.29	Asymmetry data taken during PREX-II experiment on 8/10/2019. Measured asymmetries shown on right-hand vertical axis and correspond to analyzing powers on left-hand vertical; scaling factor calculated as prescribed in eq. (3.12). Vertical error bars equal to statistical error on asymmetry scan measurements and statistical error on standard daily polarization measurement used for converting the measured asymmetry to analyzing power added in quadrature.	109
4.30	Detailed asymmetry data taken during CREX experiment on 2/8/2020. Measured asymmetries shown on right-hand vertical axis and correspond to analyzing powers on left-hand vertical; scaling factor calculated as prescribed in eq. (3.12). Error bars equal to statistical error on asymmetry scan measurements and statistical error on standard daily polarization measurement used for converting the measured asymmetry to analyzing power added in quadrature.. . . .	110
4.31	Summary of rate scans performed in August 2019 during the PREX-II experiment. Simulation predicted rate is shown against magnet current. Measurements taken on 8-4-2019 are highlighted in gold circles while all other measurements are simply marked.	111

4.32	Plots of ADC data for the left arm of the Møller calorimeter (Blocks 0-3) from a commissioning run for PREX-II utilizing the 8PMT configuration. Off-axis scatter plots of PMTs 0/1, 1/2, and 2/3 are of interest and show small amounts inter-block energy bleedover. In this optical setup the 0/1 block boundary would be expected to have the largest amount. On-axis plots are histograms of signal distributions recorded by the ADC for each PMT.	112
4.33	Visual depiction of shower-bleedover systematic simulation study for the 2PMT PREX-II optics setup (CREX optics included only one sensitive edge). Region of "possible acceptance" limited to one Molière radius.	113
4.34	Møller polarimetry dead time correction percentages per data run for the PREX-II and CREX experiments.	115
4.35	Møller polarimetry charge normalization correction percentages per data run for the PREX-II and CREX experiments.	117
4.36	Møller polarimetry charge normalization correction percentages per data run for the PREX-II and CREX experiments.	118
4.37	Data from a 2007 Hall C study performed to help place limits on systematics concerns about current-dependent polarization changes. The study used three methods for controlling the beam current delivered to the experimental hall. Polarization measurements were taken for each method and zeroth-order fits (left-panel) and first-order polynomial fits (right-panel) were made to the data. [Image of data courtesy of David Gaskell]	119
4.38	Møller asymmetry for Cu foil measurements taken during PREX-II; bins marked by date taken. Measurements are HWP/Wien sign-corrected. . .	121
4.39	Møller asymmetry for Cu foil measurements taken during CREX; bins marked by date taken. Measurements are HWP/Wien sign-corrected. . .	121

5.1	Example of data taken on the watercell target during CREX (RHRS arm data shown). Hydrogen scattering peak marked on left at $P = 2.163(24)$ GeV and Oxygen marked on right at $P = 2.179(5)$ GeV. Difference between scattering peaks is $16.126(24)$ MeV [Image courtesy of Siyu Jian [76]]	127
5.2	Sample data of sieve data angular reconstruction of θ_{targ} vs. ϕ_{targ} [black] vs. simulation expectations [red]. Axes values shown are deviations from expected central angles.	128
5.3	Transverse Scattering Diagrams. Left-panel: Single photon exchange between the electron and target nucleus; Right-panel: A double-photon exchange with the target nucleus. Figure taken from [79].	131
5.4	PREX-II acceptance function $\epsilon(\theta)$. Figure taken from supplemental materials of [75]	133
6.1	Comparison of CREX asymmetry data against simulation results from MolPol using the generally used modified hydrogen wavefunction model (labeled ‘Hydrogenic’ in the graphic above) to generate the momentum spectrum for the bound iron electrons and the momentum spectrum for the bulk-iron electrons generated from Hartree-Fock calculations.	138
7.1	SoLID detector configuration for the PVDIS experiment.	142
7.2	Electron cascade within a GEM detector. Between the drift and charge collection cathodes are thin polymer foils which are metal coated on both sides with a high density of holes drilled into the foil. The application of a large potential applied to the foil creates electric field lines such that ionized electrons are directed through the drilled holes and acquire sufficient energy while traveling in the field to cause additional ionizing collisions within the gas causing an electron cascade directed towards charge collection wires. The more numerous the internal GEM foils the larger the cascade. Image adapted from [90]	144

7.3	Gamma spectrum from 11GeV beam on 1mm thick carbon target detected between 15° and 40° off the beam axis. Compton scattered beam bremsstrahlung, bremsstrahlung from Møller scattered electrons are shown as well as a small contribution of gammas labeled “others” from secondary interactions.	146
7.4	Spectrum of gammas which resulted in an interaction in GEMs 1 through 5. .	147
7.5	Pulse energy deposit vs distance of centroid of energy deposit from entrance point of photon on the GEM detector.	148
7.6	Spatial spread of energy deposits in GEM from thin pencil beam composed of spectrum shown in fig. 7.3. Energy deposits are divided into four categories—backgrounds resulting from events which originated in the air in front of the GEM, events which occur within the ArCO ₂ gas and forward scattered events from the copper anode and backscattered events from the first internal GEM foil.	149
7.9	Signal and background energy densities from 4cm x 4cm square of incident gammas of spectrum shown in fig. 7.3 on 10mm radius W collimator which is 30mm thick with 1mm hole centered at origin. Left panel shows area of projection for center and right panel histograms. Center panel histogram shows event density along projection stacked by source volume for event. Right panel shows deposited energy in area of projection.	150
7.7	Square beam of gammas, 2cm x 2cm, incident on 2cm thick lead plate with 1mm hole centered at origin. Signal to background ratio ≈ 2	151
7.8	Square beam of gammas, 2cm x 2cm, incident on 6cm thick lead plate with 1mm hole centered at origin. Signal to background ratio ≈ 20 ; an order of magnitude improvement from 2cm thick lead plate.	152
7.10	Energy deposition by gamma rays produced from beam on Carbon target in the five GEM detectors of the SoLID spectrometer in the PVDIS setup with magnetic field on. A rather clean signal is seen in each GEM.	153

7.11	Energy deposition by gamma rays produced from beam on Carbon target in the five GEM detectors of the SoLID spectrometer in the PVDIS setup with magnetic field on. A rather clean signal is seen in each GEM.	154
8.1	Comparison of CREX asymmetry data against simulation results from MolPol using the generally used modified hydrogen wavefunction model (labeled ‘Hydrogenic’ in the graphic above) to generate the momentum spectrum for the bound iron electrons and the momentum spectrum for the bulk-iron electrons generated from Hartree-Fock calculations.	156

List of Tables

1.1	Electromagnetic and weak charge values for fermions. First-order values for the weak charges for protons and neutrons can be derived from summing over the constituent quarks.	18
3.1	Summary table of optics settings for the PREX-II and CREX experiments. Values given are for the pole tip field and are in units of Tesla. Both Q1 and Dipole settings are nominally recommended settings and are ultimately set by rate scan results.	67
4.1	Summary of dead time rate measurement runs taken during PREX-II. . .	80
4.2	Wien settings for PREX-II and CREX prior to and after spin dance Møller polarimetry measurements.	90
4.3	Calculated weighted arithmetic means of matched Møller and Compton measurements. Errors are absolute percent. Difference of the means is Compton minus Møller.	99
4.4	Select summary of simulation data for PREX Q1 optics simulated asymmetry scan. Targeted diagnostic tuning point was 3% over the identified rate maximum—the $\delta A_{zz}/A_{zz}$ are relative to that tuning point.	103

4.5	Select summary of simulation data for CREX Q1 optics simulated asymmetry scan. Values that are $\pm 10\%$ detuned off of the targeted set point at 20.8% were interpolated from the simulation data and are shown in blue; these values are the basis for the systematic assignment.	104
4.6	Summary of PREX-II Q2/Q4 sensitivity simulation results. Maximum change in analyzing power highlighted in blue.	104
4.7	PREX-II dipole scan second-order polynomial fit $f(x) = Ax^2 + Bx + C$ parameters and errors as performed in ROOT along with fit maximum $\text{fit}^{\max} = -\frac{B}{2A}$ and $\text{fit}_{\text{error}}^{\max}$ equal to the errors added in quadrature. Dipole Scan 1035 was a scan performed while altering the B.dl of the MBC1H01 (horizontal) corrector magnet to see if we could induce significant rate changes (45% loss) observed on 8/4/2019. Dipole scan 1069 was an end-of-shift check using the $4\mu\text{m}$ foil to check against dipole scan 1060 performed with the $10\mu\text{m}$ foil earlier in the day.	106
4.8	Select summary of simulation data for PREX-II dipole optics scan. A -1.5% mistuning has a potential 0.05% asymmetry uncertainty impact.	108
4.9	Select summary of simulation data for CREX dipole optics scan.	108
4.10	Summary of bleed through measurements recorded during Møller polarimetry measurements during the CREX experiment.	116
4.11	Summary of Møller polarimetry analyzing power systematics for the PREX-II experiment.	124
4.12	Summary of Møller polarimetry systematics the PREX-II experiment.	124
4.13	Summary of Møller polarimetry analyzing power systematics for the CREX experiment.	125
4.14	Summary of Møller polarimetry systematics the CREX experiment.	125

5.1	Summary table of polarization measurements provided to the PREX-II experiment [errors shown are absolute (Polarization %)].	130
5.2	Summary of corrections to the asymmetry along with systematic uncertainties. Total uncertainty in beam polarization is the largest source of error at 5.2ppb. Adapted from [75].	134
A.1	Summary of PREX-II Møller polarimetry spin dance measurements taken on July 24, 2019.	159
A.2	Summary of CREX Møller polarimetry spin dance measurements taken on January, 7 2020.	160
A.3	Summary of PREX-II Møller polarimetry Cu foil null asymmetry measurements.	160
A.4	Summary of CREX Møller polarimetry Cu foil null asymmetry measurements.	161
A.5	Summary of PREX-II Møller polarimetry foil jogging systematic study measurements.	161
A.6	Summary of PREX-II Møller polarimetry asymmetry scan measurements taken on 8/10/2019. Percent detuned off of optimal optics setting in shown.	161
A.7	Summary of CREX Møller polarimetry asymmetry scan measurements taken on 2/8/2020. Percent detuned off of optimal optics setting in shown.	162
A.8	Summary of PREX-II Moller Polarimetry Group Measurements.	162
A.8	Summary of PREX-II Moller Polarimetry Group Measurements.	163
A.9	Summary of CREX Møller Polarimetry Group Measurements	163

Chapter 1

Introduction

This introduction will give a broad overview on how our understanding of the atomic nucleus and particle physics has developed with a focus on electroweak physics and the physics behind parity-violating particle scattering. All of this serves to highlight the scientific motivation for the PREX and CREX experiments whose parity-violating asymmetry measurements will be used for a high-precision calculation of the neutron skin of ^{208}Pb and ^{40}Ca . The focus of this thesis will be of my contributions made towards the measurement of the parity-violating electron scattering asymmetry.

1.1 The Atomic Nucleus

Over two millennia ago, Greek philosophers hypothesized that our world was made of tiny indivisible tiny solid objects make up all of the physical matter in the universe; these pieces of matter were called “atomon”. This hypothesis, however, was not the work of physical experimentation but was philosophical in context and purely a matter of reason—the big things which make up the world we live in could be decomposed into smaller and smaller things until we reach the most basic building blocks of our world. It was also believed that these small things could be combined in different ways to create all of the different objects and materials that were observed in the world. This conceptual view

of the world served as the dominant model for centuries. Society learned it could separate metals from minerals through various physical and chemical processes and alchemists tried in vain, through early chemistry, to transmute elemental materials such as lead into gold. It was unclear as to why it was possible to separate materials into their elemental components but yet impossible to transform those base materials, through other means, into different materials.

At the end of the 19th century J. J. Thomson discovered the existence of the negatively charged electron [1]. This was the first scientific declaration that the atoms that make up our world were comprised of smaller, more fundamental, particles. At least, they certainly contained small negatively charged particles. Less than a decade after this discovery Thomson proposed his colloquially known “plum pudding” model of the atomic nucleus which proposed that the atom was effectively a ball of positive charge with negatively charged electrons stuck within it [2]. This was a huge step forward in our understanding of nuclear structure as it turned the idea that the fundamental building block of our universe was the atom completely on its head. Thomson went on to win a Nobel Prize in Physics; the prize, however, was for the “great merits of his theoretical and experimental investigations on the conduction of electricity by gases”.

In 1911, Earnest Rutherford demonstrated through gold foil scattering experiments that the positive charge in an atom was not evenly distributed throughout, as per Thomson’s model, but very concentrated at the center of the atom [3]. Rutherford supposed that the electrons were randomly distributed in orbits around this nucleus—the center of the atom was coined this name decades beforehand by Faraday as the “nucleus”. He followed on these revelations, in 1914, with additional observations—not solely his—on the charge of the nucleus in relation to its mass [4]. Shortly afterwards, modifications were made to this ongoing working model of the atom by Niels Bohr who suggested—in an effort to incorporate Planck’s quantum theory and Einstein’s photoelectric effect—that the electrons were not randomly distributed around the nucleus but rather were arranged in discrete circular orbits around the nucleus [5].

Less than a decade after demonstrating that the positive charge of an atom was densely packed at the nucleus Rutherford again, in 1919, furthered our knowledge of nuclear structure by announcing his discovery of hydrogen nuclei being ejected from nitrogen which were subject to alpha radiation [6]. Rutherford declared that hydrogen nuclei were present in all matter; not long afterwards, Rutherford named these hydrogen nuclei the “proton”.

Finally, it was Erwin Schrödinger [7] who demonstrated through quantum mechanics that electrons did not revolve in circular orbits but rather “buzzed” around in harmonically arranged electron clouds; at least, he demonstrated such for a basic hydrogen atom.

It was clear, as Rutherford noted in his 1914 paper [4], that there was something inherently wrong with the idea that only protons resided in the nucleus as there were differences in the relationship between atoms’ masses and their charges which indicated that an additional source of mass existed. Something else was sharing space with the proton inside of the nucleus. In 1932, James Chadwick while experimenting with beryllium atoms subjected to alpha radiation discovered the emission of electrically neutral particles being emitted with a mass approximately that of a proton; Chadwick called this emitted particle a “neutron” [8]. With the discovery of the neutron a basic modern understanding of the atomic structure was complete—a nucleus containing protons and neutrons surrounded by a cloud of electrons in harmonic clouds. This idea was seized upon by physicists who worked to come up with a theoretical description of the nucleus which contained both protons and neutrons.

1.2 Nuclear Decay

Nuclear decays played an integral role in the discoveries that led to our understanding of the atomic nucleus—in terms of protons, neutrons and electrons. There are three types of radioactive decays of the atomic nucleus: alpha decay (the emission of a helium nucleus) which were crucial to Rutherford’s original gold foil experiments; beta decay (the

emission of an electron) which led to uneasy questions about missing mass in the process of the decay; and gamma rays (high energy photons). The names *alpha* and *beta* were designated by Rutherford in 1899 [9] and later in 1902 Rutherford added *gamma* [10]; although gamma rays were discovered by chemist Paul Villard while studying radium and described as "very penetrating" radiation and later were merely categorized and given description by Rutherford.

George Gamow described in 1928 the quantum mechanical tunneling process that allows alpha decay to occur [11]. In 1933, Enrico Fermi introduced his theory of beta decay that theoretically resolved outstanding questions regarding missing mass [12, 13] and was build upon ideas developed by Wolfgang Pauli. Fermi's work is today considered to be an effective field theory for the weak interaction.

1.3 Parity Symmetry

Symmetries exist across all of physics and perhaps are best known in classical mechanics with their relation to the Lagrangian and Action. In 1918, Emily Noether published her profoundly impactful paper on symmetries and conserved quantities; her two revelations [14], which are now famously addressed as Noether's Theorems, tell us that for each symmetry in nature there is an underlying conserved quantity—invariance to translations in space implies a conservation of linear momentum; invariance to rotation implies a conservation of angular momentum and invariance to time implies a conservation of energy.

Parity symmetry refers to the invariance of physics under the reversal of the coordinate system. Letting \mathcal{P} be an operator that inverts coordinates:

$$\begin{aligned}\mathcal{P}(\vec{r}) &= -\vec{r} \\ \mathcal{P}(\vec{p}) &= -\vec{p} \\ \mathcal{P}(\vec{L}) &= \mathcal{P}(\vec{r}) \times \mathcal{P}(\vec{p}) = \vec{L}\end{aligned}\tag{1.1}$$

The parity transformation, while it reverses quantities such as \vec{r} and \vec{p} , leaves quantities

such as angular momentum \vec{L} unchanged. Hence, mirroring a universe would change the direction of momentum of an object but not the object's angular momentum leaving angular momentum conserved under a parity transformation.

While aforementioned symmetries exist in continuous systems there also exist symmetries in discrete systems as well; parity is one of them. In particle physics, symmetries constrain the set of all imaginable particle interactions to the set of all physically possible particle interactions; thus, a thorough understanding of them, including the breaking of, was of great interest. The prevailing and safe assumption in the early years of experimental particle physics was that parity was always conserved.

1.4 Parity Violation

In 1956, the prospect of parity violation in particle physics was suggested by Lee and Yang in what they referred to as weak interactions and describe as “decay interactions for the mesons and hyperons, and various Fermi interactions”[15]. Lee and Yang addressed what they describe as the “rather puzzling” situation of the decays of the Θ^+ and τ^+ mesons whose masses and lifetimes suggested they were indeed identical particles but couldn't have been identical particles if parity conservation were to be held true. Together they outlined the basics for an experiment that would test for parity violation using beta decays.

In 1957, their theoretical prediction was confirmed in the now famous ^{60}Co experiment which was rigorously designed and tested by Chien-Shiung Wu [16]. In demonstrating that there was there was a directional preference in the beta decay of ^{60}Co in the direction opposite of spin, Wu's experiment proved that parity was not conserved in beta decays.

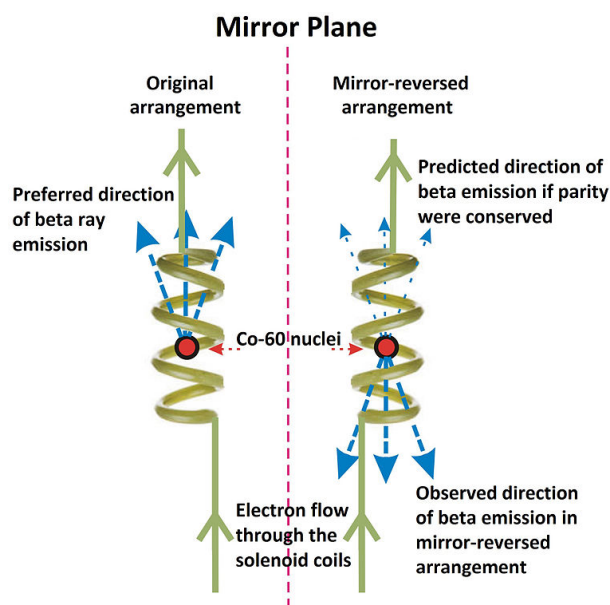


Figure 1.1: Depiction of the Wu experiment and parity violation. On the left, the experiment with performed in the “original coordinate” system where Cobalt atoms are aligned in magnetic field caused by passing of current through solenoid wires (in this case in the downward direction on the page). On the right, we have the “mirrored” coordinate system; the magnetic fields passing through the solenoid coils would be opposite that of the original coordinate system so in an experimental setting reversing the current and field through the coils has the same effect as a parity inversion. If parity were respected the the direction of beta emission would have been the same. This was the first strong evidence that the weak force violated parity. *Image from Wikimedia Commons [17]*

1.5 The Weak Force

Enrico Fermi made the first attempt at strictly describing beta decay, known now to be a weak force interaction, as an interaction without a mediating boson [12]. However, the experimental results of Wu which gave strong credence to Lee and Yang's work provided strong motivation to come up with a better description of beta decays in an axial-vector formulation—which would more fully explain the parity-violating observations.

These fuller mathematical and physical descriptions of the weak force were not made until the 1960's. Sheldon Lee Glashow [18], Steven Weinberg [19] and Abdus Salam [20] independently developed ideas which described the weak force in terms of quantum field theory—in what is now known as Weinberg-Glashow-Salam (WGS) theory and commonly referred to as Electroweak theory—which unites electromagnetism and the weak force. Glashow provided the $SU(2) \times U(1)$ framework for the electroweak interaction description which resulted in massless force carriers while Weinberg and Salam integrated Peter Higgs' symmetry breaking scalar potential field [21] into the theory to provide masses to the force carriers.

Electroweak theory states that the electromagnetic force and the weak force, at one time united, underwent a spontaneous symmetry-breaking phase transition. Prior to this breaking the electroweak force consists of the neutral B_0 vector boson of the weak hypercharge gauge field and the neutral W_0 and charged W_1 & W_2 bosons of the weak isospin gauge fields all of which are massless. After symmetry breaking the neutral B^0 and W^0 neutral bosons are mixed through a single parameter θ_W known as the Weinberg Angle (or weak mixing angle)—this parameter represents the specific linear combination of the B_0 and W_0 bosons required to produce the weak Z_0 and electromagnetic γ given by eq. (1.2). Additionally, symmetry breaking mixes the charged W_1 and W_2 states into

the massive weak W_+ and W_- charged bosons given by eq. (1.3).

$$\begin{bmatrix} Z_0 \\ \gamma \end{bmatrix} = \begin{bmatrix} \cos \theta_W & -\sin \theta_W \\ \sin \theta_W & \cos \theta_W \end{bmatrix} \begin{bmatrix} W_0 \\ B_0 \end{bmatrix} \quad (1.2)$$

$$W_{\pm} = \frac{1}{\sqrt{2}} (W_1 \mp iW_2) \quad (1.3)$$

The charged weak bosons are responsible for flavor-changing interactions and neutrino-emitting processes and the Z_0 boson is involved in interactions which there is no flavor or charge change and acts merely as an exchange of energy/momentum as well as being involved in neutrino-scattering processes.

From Electroweak theory description and verified by experiment we know that the weak force is mediated by three bosons—the charged W bosons W^{\pm} and the neutral Z_0 boson whose masses match predictions— $M_W = 80.379 \pm 0.012$ and $M_Z = 91.1876 \pm 0.0012$ [22]. Direct observation of the Z_0 and W_{\pm} bosons [23, 24] was made in 1983 at CERN by the UA1 collaboration. Early observations of Electroweak predictions of neutral currents via neutrino interactions were made at CERN in 1973 utilizing the Gargamelle bubble chamber [25, 26]. Most importantly, it predicts that parity violation should be maximally violated within both charged and neutral currents.

Parity violation was observed in charged-current weak interactions early on and it was unknown whether or not neutral-current weak interactions could also be parity violating until, in 1978, the SLAC E122 detected and measured the parity-violating asymmetry in inelastic electron- ^2H scattering [27]. This measurement not only provided an experimental confirmation of the parity-violating nature of the Z_0 but also gave means to measuring the Weinberg angle $\sin^2 \theta_W$ —a measurement which agreed with predictions—which put WGS theory on much firmer grounds and demonstrated that weak interaction maximally violated parity.

1.6 The Standard Model

The electromagnetic force has been fairly well understood since the late 19th century. Maxwell's collection of equations accurately described observed electromagnetic phenomena in terms of classical mechanics. Twentieth century developments saw it formalized into the language of quantum field theory as Quantum Electrodynamics (QED) with the photon γ as its force carrier—where particles which are electromagnetically charged interact via the absorption or emission of photons. QED has undoubtedly been one of the most accurate and precisely verifiable theories in modern physics.

The just-described successful description of the weak interaction in terms of quantum field theory provided the same structure; particles which possess weak charge weakly interact through the absorption or emission of the weak bosons.

The development of electroweak theory was followed shortly thereafter by a successful description of the strong interaction which vastly simplified the ever-growing catalogue of new particles being detected. The force carrying particle of the strong interaction is the massless gluon (g) and it interacts via a “three-dimensional” charge generally referred to as color charge; this theory is commonly known as quantum chromodynamics (QCD). QCD like QED does not violate parity; for the purpose of this thesis which deals specifically with parity violation, QCD is only mentioned for a complete description of the Standard model and for emphasis that the interactions do not violate parity.

Combined, these three interaction descriptions form the basis for the Standard Model of particle physics which dictates that particle interactions must involve the transmission of force carrying bosons. Particle interactions can occur in any variety of ways so long as those interactions are not forbidden—they cannot violate a required symmetry.

Standard Model of Elementary Particles

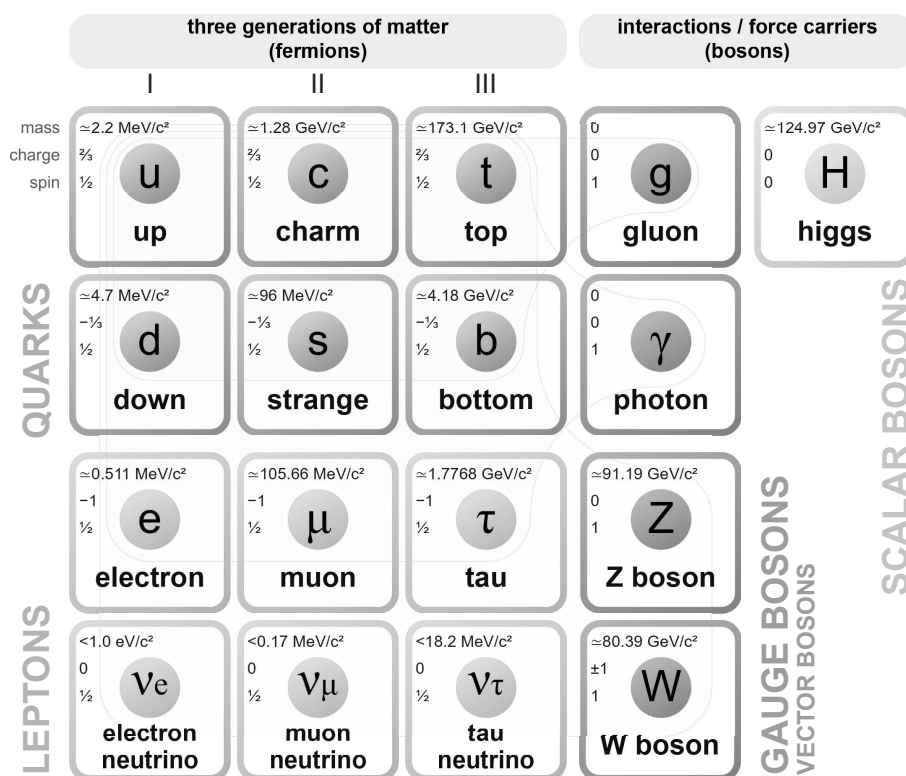


Figure 1.2: The Standard Model showing the three generations (I, II, III) of quarks and leptons, the gluons (there are actually 8 flavors), the photon, the Z_0 and W_{\pm} bosons and the Higgs. *Image from Wikimedia Commons [28]*

The Standard Model 1.2 provides the basis for the interactions and classification of all particles. The majority of predictions made by the Standard Model have been experimentally verified and continue to be with ever-increasing precision.

1.7 Measuring the Atomic Nucleus

The described forces of the standard model provide a foundation for the interactions which build and bind the nuclei of our universe together. The proton charge radius R_p is a basic property of the proton or any . Since the proton has an electromagnetic charge while the neutron does not the charge radius is somewhat easily accessed by measuring electron-proton scattering. Due to this ease, R_p has been extensively studied in experimental particle physics. The detailed understanding of nuclear charge radii and charge densities is an essential underpinning of our picture of the modern atomic nucleus.

Extensive documentation of the charge radii of nuclei is given in ref. [29].

Yet, because neutron has no electric charge the measurement of neutron densities and measuring the neutron radius R_n of atoms with traditional particle scattering strategies has been somewhat difficult. The neutron radius has long been suspected to be larger than that of the proton; early research on the topic comparing nuclear sizes to proton radius [30] suggested that not only should the neutron distribution exceed that of the proton distribution but appeared to increase with atomic number. Measurements of neutron densities which have been made generally come from scattering experiments involving hadrons; unfortunately, this method of probing the neutron densities leaves experiments with theoretical systematic uncertainties that arise from the model-dependent descriptions of the strong interaction [31]. Similarly, methods involving π^0 photoproduction to measure the total nucleus size—from which one could obtain a neutron skin measurement by subtracting out the charge radius from total nucleus size—can achieve reasonable statistical precision but are hindered by rather large theoretical uncertainties and model dependencies of π_0 -nucleus interactions. An extensive review of approached methods for measuring the neutron skin of nuclei is available in [32].

This lack of clean experimental information on the neutron radius of heavy atoms which is free of large theoretical systematic uncertainties has led to a somewhat incomplete modern picture of the atomic nucleus and has left large uncertainties in other associated quantities such as nuclear density which will be discussed in section 1.14.

1.7.1 Utilizing Parity Violation

Just as physicists have measured R_p by looking at the radius of the electromagnetic charge/force, similarly, the weak charge/force can be utilized to calculate R_n . In 1989, Donnelly, Dubach and Sick [33] made the suggestion that neutron densities could be effectively probed utilizing parity-violating electron scattering (PVES). Since the neutron has a significantly larger weak charge compared to that of the proton table 1.1, polarized electron beams can be used to probe the neutrons. The resulting asymmetry yields rather

clean model-independent information on the distribution since the asymmetry is the result of the weak force only and avoids complicated model-dependent uncertainties from the strong interaction approximations.

1.8 Particle Scattering

The dominant method utilized in the study of atomic and sub-atomic structures is particle scattering; particle scattering experiments have, since the beginning of experimental nuclear physics, provided us with a powerful tool to peer inside the atom. In elastic scattering the kinetic energy of the incident particle (and generally whole system) remains unchanged with only the directions of motion being altered. Elastic scattering is particularly useful as a tool in studying nuclear structures.

For any two particles in an elastic scattering interaction we can define four-momentum transfer squared q^2 as the momentum change $p_f - p_i$ between initial and final states.

$$q^2 = -Q^2 = 2E^2 - 2p_f p_i \quad (1.4)$$

In any scattering reaction number of events N which are measured is proportional to the flux F and the cross section σ

$$N = F\sigma. \quad (1.5)$$

From the Fermi golden rule the cross section is proportional to the matrix element squared

$$\frac{d\sigma}{d\Omega} \propto |M_{fi}|^2 \quad (1.6)$$

eqs. (1.5) and (1.6)

1.9 Elastic Scattering

The scattering of a relativistic particle off of a target neglecting recoil effects is called Mott Scattering. In general, this is treated assuming that the target particle is very small and point-like. The full Mott scattering cross section, which accounts for relativistic spin effects, of a sufficiently high energy electron such that $\beta = \frac{v}{c} \approx 1$ off of a point-like particle is given by

$$\frac{d\sigma}{d\Omega_{\text{Mott}}} = \underbrace{\frac{4\alpha^2 E^2}{|q|^4} \cos^2 \frac{\theta}{2}}_{\text{Spin-less Interaction}} - \underbrace{\frac{4\alpha^2 E^2}{|q|^4} \frac{|q|^2}{2M^2} \sin \frac{\theta}{2}}_{\text{Spin-spin Interaction Correction}}. \quad (1.7)$$

Spin effects can be neglected by choosing a spinless target. ^{208}Pb is a doubly-magic isotope, having closed shells for both protons and neutrons, and is thus spinless and an ideal candidate for such experimental study. Additionally, lead has the largest ground state to first excited state energy separation. The Mott cross section then, for a atomic nucleus with zero spin and total charge Ze , is given by

$$\frac{d\sigma}{d\Omega_{\text{Mott}}} = Z^2 \frac{4\alpha^2 E^2}{|q|^4} \cos^2 \frac{\theta}{2}. \quad (1.8)$$

1.10 Form Factors

The nucleus is not a single solid point charge but a distribution of charge with a finite size. Hence, the nucleus is better described in a proper quantum mechanical way as a probabilistic charge distribution $\rho(r)$ with total charge Z .

$$\rho(r) = (Ze)|\Psi(r)|^2 \quad (1.9)$$

such that

$$\int |\Psi(r)|^2 d^3r = 1. \quad (1.10)$$

When charge distributions are introduced to scattering calculations they manifest themselves as modifications to the point-like scattering cross sections eq. (1.12) These modifications are referred to as form factors and are specific to their descriptions.

$$\frac{d\sigma}{d\Omega} = \frac{d\sigma}{d\Omega_{point-like}} |F(Q^2)|^2. \quad (1.11)$$

The form factors which are functions of Q^2 are the Fourier transforms of the charge densities and take the form

$$F(Q^2) = \int e^{-iq \cdot r} \rho(r) d^3r. \quad (1.12)$$

At $Q^2 = 0$ the form factor integrated over r should be equal to the charges present. In regards to this thesis, the neutron form factor F_N and weak form factor F_W are interchangeable and describe the distribution of neutrons and weak charge within the nucleus; similarly, the proton form factor F_P and electric form factor F_{CH} are interchangeable. Information about the radius of a charge distribution can therefore be extracted from form factors which are themselves related to the scattering cross sections. The Mott scattering cross section can then be modified to account for the spatial distribution of target charges which are scattering electrons by combining eqs. (1.8) and (1.11)

$$\frac{d\sigma}{d\Omega} = \frac{d\sigma}{d\Omega_{Mott}} |F(Q^2)|^2. \quad (1.13)$$

Comparisons of various form factors against charge distributions are shown in fig. 1.3.

Since ^{208}Pb is a doubly-magic isotope its charge distribution—electromagnetic and weak—is assumed to be perfectly spherical; this then simplifies the extraction of the

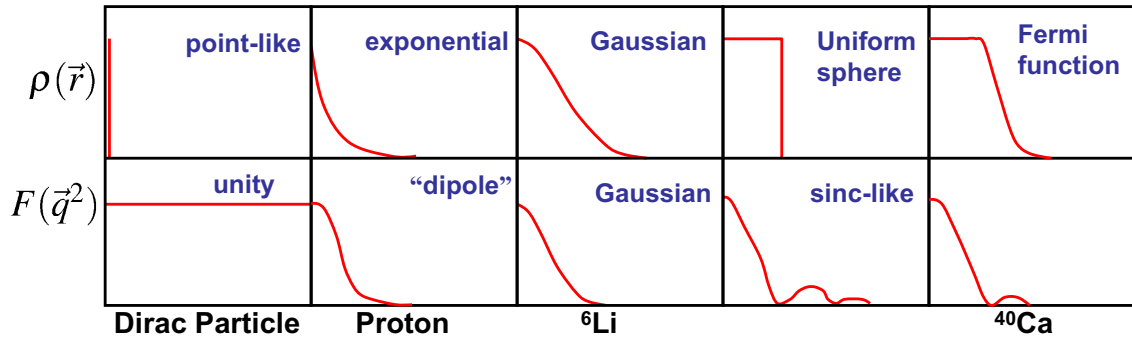


Figure 1.3: A comparison of charge distribution density functions and their corresponding form factors for a variety of charge distributions.

charge radius. Under such an assumption the weak form factor F_W takes the form

$$F_W(Q^2) = \int j_0(qr)\rho_W(r)d^3r. \quad (1.14)$$

where j_0 is the zeroth-order spherical Bessel function $j_0(x) = \text{sinc}(x)$ [34].

1.11 Helicity

Helicity is scalar quantity which comes from the dot product of the spin \vec{s} and momentum direction $\vec{p}/|\vec{p}|$ of a moving particle.

$$H = \vec{s} \cdot \frac{\vec{p}}{|\vec{p}|} \quad (1.15)$$

If the spin and momentum direction are aligned the helicity is a positive quantity and the particle is said to be right-handed while if the helicity is negative it is said to be left-handed. Helicity itself is not a fundamental property a massive particle. However, it is dependent on the frame of reference since a parity change inverts momentum while leaving spin unaltered.



Figure 1.4: Helicity/Particle-Handedness of particles with particular spin and direction of travel. A negative helicity (left-handedness) occurs when spin direction and momentum directions are anti-parallel and a positive helicity (right-handedness) occurs when spin direction and momentum direction are parallel.

1.12 Parity-violating Asymmetry

Since this formalism will be used several times, a general particle scattering asymmetry is calculated as follows where $\frac{d\sigma}{d\Omega}$ is the differential cross section being measured

$$A = \frac{\frac{d\sigma}{d\Omega}_a - \frac{d\sigma}{d\Omega}_b}{\frac{d\sigma}{d\Omega}_a + \frac{d\sigma}{d\Omega}_b} = \frac{\sigma_a - \sigma_b}{\sigma_a + \sigma_b} \quad (1.16)$$

where a and b are two qualitatively different states and we can omit the $d\Omega$ s as implied for convenience under the assumption that the solid angle of the differential cross section is the same for both states.

The PREX experiment will be looking for parity-violating scatters of helicity-controlled electrons off of lead nuclei. While the primary interaction is electromagnetic which is a parity-conserving interaction the infrequent weak Z_0 exchanges are not; these interactions are shown in fig. 1.5. Thus, measuring the asymmetry of the scatters between the two helicity states will yield information about the weak scatters.

Here, we'll deal with electron scattering on nuclei and while the predominant interaction in electron scattering is electromagnetic the weak force is, from time to time, involved; since the weak force violates parity we can statistically examine these events. For parity-violation where we're examining different scattering rates between left-handed and right-handed

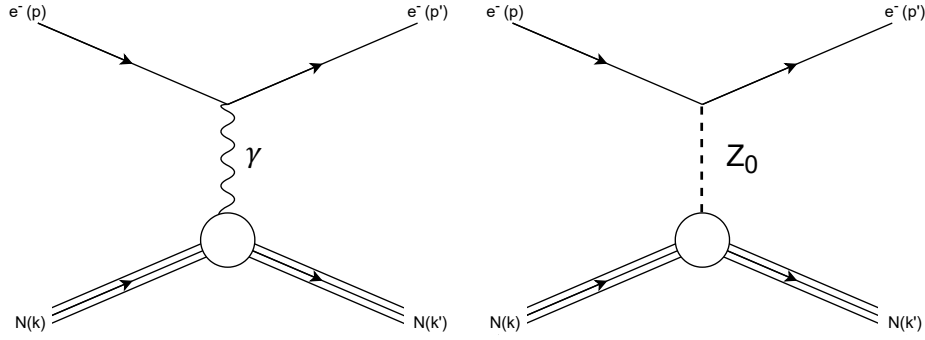


Figure 1.5: Feynman diagrams for electron-nucleon scattering for photon and Z_0 interaction.

scatters we can write eq. (1.16) as

$$A_{PV} = \frac{\sigma_R - \sigma_L}{\sigma_R + \sigma_L}. \quad (1.17)$$

The relationship between the parity-violating asymmetry A_{PV} of the measured cross-sections of the opposite helicity states σ_R and σ_L can be related through the following Born approximation:

$$A_{PV} = \frac{\sigma_R - \sigma_L}{\sigma_R + \sigma_L} \approx \frac{G_F Q^2 |Q_W|}{4\sqrt{2}\pi\alpha Z} \left[1 - 4\sin^2\theta_W - \frac{F_W(Q^2)}{F_{CH}(Q^2)} \right] \quad (1.18)$$

where G_F is the Fermi constant, Q^2 is the standard four-momentum transfer, α is the fine structure constant, F_W and F_{CH} are the weak and electromagnetic form factors, Q_W total weak charge of the nucleus, and Z is the total electromagnetic charge of the scattering target. The weak charge of any nucleus, with atomic number Z and neutron number N , is approximately

$$Q_W^{(N,Z)} = ZQ_W^p + NQ_W^n = Z(1 - 4\sin^2\theta_W) - N \quad (1.19)$$

In the limit of $Q^2 = 0$ $F(0)$ is equal to the number of respective charges present.

The fact that the weak force violates parity and interacts only with left-handed particles or their right-handed anti-particle counterparts while being blind to right-handed

Table 1.1: Electromagnetic and weak charge values for fermions. First-order values for the weak charges for protons and neutrons can be derived from summing over the constituent quarks.

Particle	Q_{EM}	Q_W
u, c, t	$-\frac{2}{3}$	$+1 - \frac{8}{3} \sin^2 \theta_W$
d, s, b	$+\frac{1}{3}$	$-1 + \frac{4}{3} \sin^2 \theta_W$
e, μ , τ	-1	$-1 + 4 \sin^2 \theta_W$
p	+1	$1 - 4 \sin^2 \theta_W$
n	0	-1

particles and their left-handed anti-particle counterparts allows us to measure quantities that are weak-related. Just as physicists have measured R_p by looking at the radius of the electromagnetic charge/force, similarly, the weak charge/force can be utilized to calculate R_n .

The electroweak cross-sectional dependence of the electron scattering can be found eq. (1.6) linearly adding the electromagnetic scattering matrix elements M_γ and the weak scattering matrix elements M_W giving

$$\sigma \propto |M_\gamma + M_W|^2 = |M_\gamma|^2 + 2M_\gamma M_W^* + |M_W|^2. \quad (1.20)$$

Since Z-boson weak coupling has a helicity preference (the parity violation) there is an interference term that produces a helicity-dependent asymmetry in the cross-sectional scattering. By measuring the cross-sectional rates σ in the alternating helicity states— σ_L being the left-handed state and σ_R being the right-handed state—a parity-violating scattering asymmetry can be calculated.

The source for the scattering asymmetry can be derived by incorporating and expanding eq. (1.17) with eq. (1.20) demonstrating that the parity-violating asymmetry is dominated by the interference term.

$$A_{PV} \approx \frac{2M_\gamma M_W}{M_\gamma^2} \quad (1.21)$$

An approximate size of this asymmetry for heavy neutron rich-nuclei like ^{208}Pb can be derived from eq. (1.18) with $Z = 82$, $N = 126$, approximating the value of $\sin^2 \theta_W$ as 0.25, using eq. (1.19) to get a $|Q_W| = 126$, and approximating F_W and F_{CH} at $Q^2 = 0$ leaving $F_W(0) = 126$ and $F_{CH}(0) = 82$ to give a parity-violating symmetry of

$$A_{PV} \approx \frac{G_F Q^2 |Q_W|}{4\sqrt{2}\pi\alpha Z} \frac{F_W(Q^2)}{F_{CH}(Q^2)} \approx 10^{-6}. \quad (1.22)$$

It's important to note that eq. (1.18) is a Born plane wave approximation. In reality the situation is more complicated than that due to Coulomb distortions [35, 36, 34] and present a significant correction to the parity-violating asymmetry. However, to first order the plane-wave approximation demonstrates the connection between the parity-violating asymmetry and the weak form factor. From eq. (1.18) we can see that the parity-violating asymmetry is a function of some constants and two form factors—of which F_{CH} has been well measured; this leaves A_{PV} as a function of F_W .

1.13 Extracting the Neutron Skin

Once parity-violating asymmetry has been measured it's possible to extract the Weak form factor from data and Coulomb distortion corrections are applied at this point [34] From the Weak form factor the weak charge density ρ_W and the weak radius R_W can be calculated. Finally, from the weak radius information about the neutron radius R_n and neutron skin R_{np} can be calculated.

$$R_{np} = \left(1 + \frac{ZQ_{Wp}}{NQ_{Wn}}\right) (R_W - R_{ch}) \quad (1.23)$$

An additional piece of information q_{Wp} —the proton weak charge which has a SM predicated value of 0.07 table 1.1 and is backed by measurement obtained by the Qweak experiment which was consistent with prediction [37]—is required for this final step.

1.14 Motivation for Measuring the Neutron Skin

While the primary motivation for the measurement of the neutron skin is to bring our understanding of the atomic nucleus into sharper focus there are important physical insights to be gained. The nuclear equation of state (EOS) attempts to describe the behavior of nuclear matter over a large scale from atomic nuclei to neutron stars; this size range spans an impressive eighteen orders of magnitude. There are many potential EOS models all of which make slightly different predictions. The predictions made by these nuclear equations of state are highly dependent on the nuclear density ρ —which is a sum of the proton density ρ_p and neutron density ρ_n .

The nuclear EOS is generally described as the energy of symmetric nuclear matter \mathcal{E}_{symm} with a leading-order correction dependent on the asymmetry of neutron and proton densities

$$\mathcal{E} \approx \mathcal{E}_{symm}(\rho) + \left(\frac{\rho_n - \rho_p}{\rho_n + \rho_p} \right)^2 \mathcal{S}(\rho) \quad (1.24)$$

where

$$\mathcal{S}(\rho) \approx J + L \frac{\rho - \rho_0}{3\rho_0} \quad (1.25)$$

with J being a binding energy correction, L being the slope of the symmetry energy \mathcal{S} , and ρ_0 [38] is the nuclear saturation density. It is L in eq. (1.25) which is the interesting quantity as L is directly related to the pressure of neutron matter. As a practical issue the neutron skin is directly related to the pressure of neutron matter—the higher the neutron pressure the farther neutrons will stick out and the larger the neutron skin will be.

Since heavy nuclei are far too complex for direct calculation of nucleon-nucleon interactions, methods of nuclear energy density functional (EDF) theory are applied to understand the behavior of nuclear matter. Variations on these energy density functionals produces different predictions for predictions of the neutron skin and, hence, the measured

value of heavy nuclei neutron skins can be used provide insights into nuclear saturation and constrain which EOS EDFs accurately describe heavy nuclei [38]. This is why the neutron skin which we define as

$$R_{np} = \sqrt{\langle R_n^2 \rangle} - \sqrt{\langle R_p^2 \rangle} \quad (1.26)$$

is a quantity of interest in atomic scale nuclear physics. Being able to apply experimental constraints on R_{np} would help favor or disfavor certain EOS EDF models for heavy nuclei and provide insights into the behavior of the nuclear symmetry energy at nuclear saturation. The R_{np} relationship to L across a variety of EOS EDF models is shown in fig. 1.6a and the relationship between R_{np} and A_{PV} is shown in fig. 1.6b.

Data obtained from PREX-II can provide us with a clearer picture of physical phenomena which occur in absolutely massive objects such as neutron stars [39, 36] where EOS parameters explain not only the formation of these massive stellar objects but also their core structure and mass [40], their radii [41], how they cool through the Urca process (a cyclical electron capture and beta decay cycle which results in cooling via neutrino radiation) [42], and their demise [43].

While PREX-II will provide insights into the the EOS at the point of nuclear saturation, measurements performed during CREX on ^{40}Ca will provide insights into the atomic nuclei mass region where ab initio methods can be used to directly calculate nucleon forces in light nuclei meet effective field theory and density field theory methods for calculating nucleon forces in heavy nuclei.

Chapter 2

Lab and Experimental Design

Thomas Jefferson National Accelerator Facility (JLab) provides the scientific community with the tools to perform electron scattering measurements utilizing the beam provided by their Continuous Electron Beam Accelerator Facility (CEBAF). CEBAF provides the Lab's four separate experimental halls—Halls A, B, C and D—with electron beam concurrently. This chapter will discuss the general Jefferson Lab components along with Hall-A and PREX-II/CREX specific components.

2.1 CEBAF

The facility consists of two linear accelerators, the North linac and South linac, and two re-circulating arcs, Arc 1 and Arc 2, which transport beam between the two linacs. Each linac is capable of adding approximately 1.1 GeV in momentum to the electrons. Experimental Halls A, B and C are able to be delivered up electrons with momentum to around 11 GeV receiving five passes through both linacs while Hall D can receive an additional 'half-pass' through the North linac allowing it energies up to approximately 12 GeV and up to approximately $200\mu\text{A}$ in combined currents to the halls. A basic mock-up of the accelerator design is shown in fig. 2.1.

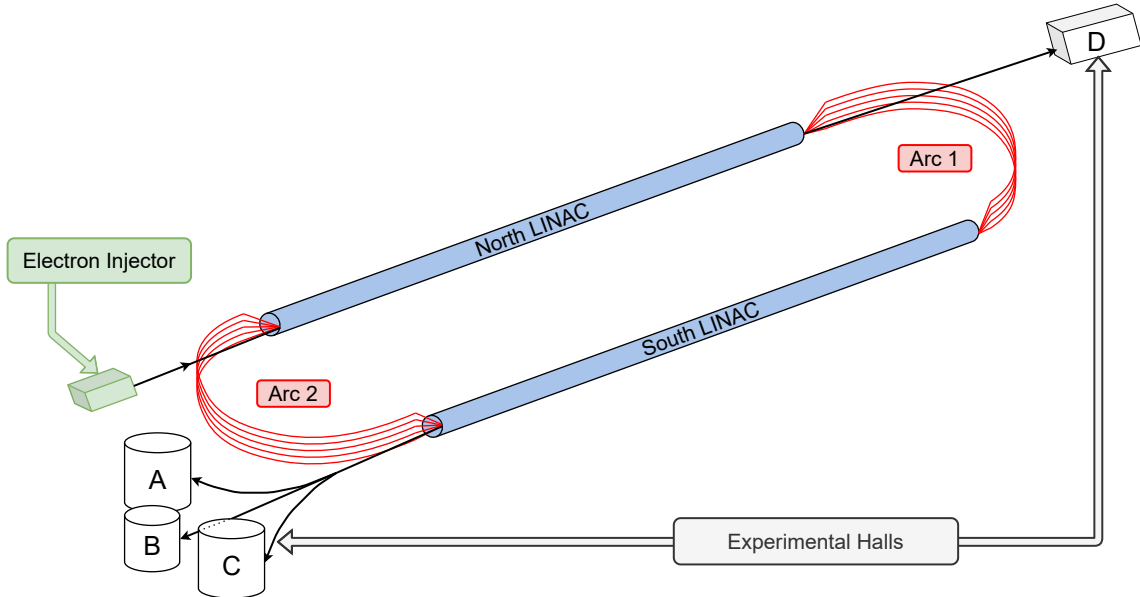


Figure 2.1: Mock-up of the Jefferson Lab Accelerator.

2.1.1 Linacs

Each linac possesses twenty five cryomodules each of which is capable of delivering between 20 to 100 MeV in momentum (depending on module construction) to the transported electrons. Each cryomodule consists of eight superconducting radio-frequency (RF) cavities. The RF cavities, so named for their operational frequency, are superconducting waveguides that are responsible for electron packet acceleration. While the linac system is designed to deliver up to 1.1GeV in energy per pass this value can be modified to specific needs by adjusting the electric fields within individual RF cavities.

2.1.2 Arcs

As the beam electrons are directed through the dipoles in each Arc to be recirculated in the linacs the electrons are subject to spin precession [45]. This effect also occurs as the electron beam is bent into Halls A and C by 37.5° and -37.5° respectively. The precession of an electron $\Delta\phi$ can be calculated as shown in eq. (2.1) [45] knowing the electron energy

E , as the electron enters the bends, and total bend angle $\Delta\theta$.

$$\Delta\phi = \frac{E}{440.65\text{MeV}} \times \Delta\theta \quad (2.1)$$

Since PREX-II and CREX both required only a single-pass through the linacs this calculation is fairly easy requiring only two precession considerations—a pass around Arc 1 and the bend into Hall A.

2.1.3 Polarized Electron Source

At the heart of JLab's operation is a high-voltage photogun which is the polarized electron source. The primary components of Jefferson Lab's polarized electron source is a super-lattice—multiple alternating layers—photocathode made of GaAs and GaAsP. This photocathode is used in conjunction with a laser system which produces circularly polarized light whose polarization is controlled by methods described in section 2.1.4. When the circularly polarized laser light comes into contact with the photoelectrode's

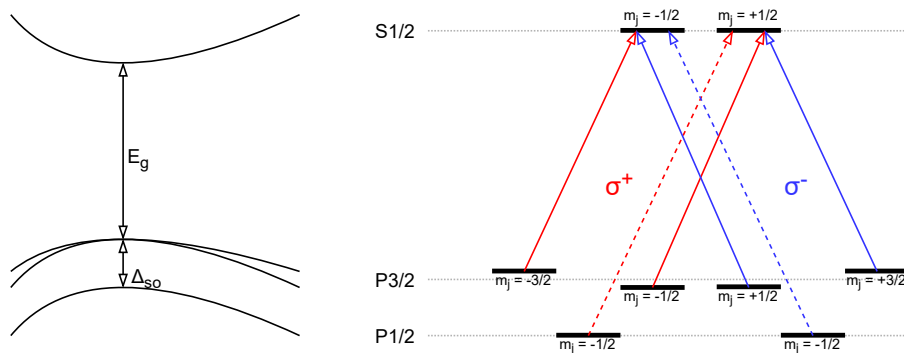


Figure 2.2: Mock up of polarized electron production within the photocathode. σ^+ and σ^- are left and right circularly polarized electrons which come into contact with the photocathode which have spin states ± 1 . The energy gap E_g is 1.52 eV while the spin-orbit splitting Δ_{so} is 0.34 eV. In this arrangement care must be taken such that the source laser energy exceeds the energy gap E_g but avoids excitement of the $p_{1/2}$ band. Figure adapted from [46].

valence band electrons they become excited polarized electrons are emitted with allowed transitions having $\Delta m = \pm 1$ being dependent on the spin of the photon; this is referred

to as optical pumping of the photocathode. A general mock-up of the photoelectric interactions is shown in fig. 2.2.

2.1.4 Helicity Control

Helicity of the electron beam provided by CEBAF is controlled by three methods each which will be briefly reviewed along with

Pockels Cell

Rapid helicity control of the laser is controlled through a dual RTP (rubidium titanate phosphate) crystal Pockels cell device for which each crystal can be independently controlled through the use of two high-voltage plates along with two ground plates. This design allows for These crystals act as a voltage-controlled wave plate—through the manipulation of a applied voltages which alter the electric field—manipulating the polarization state of the laser. For simplicity this device will be referred to as the Pockels cell throughout the remainder of this document.

Using the Pockels cell a the linearly-polarized source laser beam is turned into an alternating circularly-left polarized to circularly-right polarized beam. The now circularly left or circularly right polarized laser is placed incident upon the photocathode which then produces, via the photoelectric effect, spin-left or spin-right electrons which results in an alternating helicity pattern.

The Pockels cell is fed a pseudo-randomly generated voltage control in either quartet or octet patterns—in either $+ - - +$ or $- + + -$ for the quartets or $+ - - + - + + -$ or $- + + - + - - +$ for the octets; a diagram of this process can be seen in fig. 2.3. This produces bunches of electrons which are then fed into the injector, accelerated and delivered to the halls. The frequency of changes to the Pockels cell voltage is always chosen to be a multiple of 60Hz in order to cancel out powerline noise.

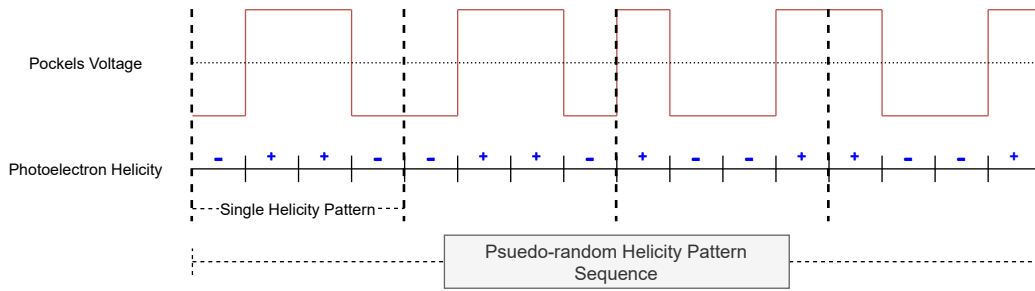


Figure 2.3: Rapid helicity control. Applied changes to the Pockels cell voltage, idealized here as a square wave, result in changes to photon polarization which results in changes to electron helicity.

Half-wave Plate

A second method of altering the helicity state of the electron beam is through the use of an insertable half-wave plate. The half-wave plates are standard optics table equipment and require no detailed explanation here. They are used to turn left circularly polarized light to right circularly polarized light by insertion into the laser path. The obvious benefit of using an half-wave plate to reverse the helicity of the laser is that it is a purely physical solution and requires no changes to the electronics.

Wien Filter

The Wien filters are dipole magnet devices which utilizes perpendicular magnetic and electric fields in the plane transverse to the motion of the electron such that the net force—as would be calculated from the Lorentz equation eq. (2.2)—equals zero and travels on an unaltered trajectory.

$$\begin{aligned}\vec{F} &= q(\vec{E} + \vec{v} \times \vec{B}) = 0 \\ q\vec{E} &= -q\vec{v} \times \vec{B}\end{aligned}\tag{2.2}$$

The Wien filter does, however, cause a spin-precession of the electrons as they pass through the magnetic field component. In this way, the filter can be used to fine tune the spin direction of the electrons as they are passed into the accelerator in order to maximize

overall polarization of the beam in the experimental halls. The total angle of electron precession in the Wien filter is referred to as the Wien angle. The Wien filter can be used to flip the helicity of the beam to tease out helicity-correlated beam asymmetries which drift slowly over time.

Unwanted Helicity-Correlated Beam Effects

While neither the half-wave plate or the Wien filter can achieve the rapid helicity flipping which can be achieved through the Pockels cell, these options can be used to cancel out electronic noise and other unwanted effects [47]. This electronic noise can be effectively cancelled out by performing less-frequent flips through the insertion of the half-wave plate; these half-wave plate flips reverse the sign of the helicity relative to that of the voltage signal and any associated phase shift which is introduced by the Pockels cell. A third flipping, which is used to cancel additional effects at the cathode level, is performed with the Wien filter; this process is extremely time consuming and eats up several hours of experimental time and is done infrequently.

PITA Effect

The Pockels cell can introduce or fail to correct for small amounts of linear polarization in the laser beam. The contributions of this linear polarization leaves the laser with a transmission asymmetry [48, 47] as the linearly polarized components have a preferred axis of transmission through optical components. We can define a transport asymmetry in the following manner letting T_x be the axis of maximum transmission and T_y be the axis of minimum transmission

$$\epsilon = \frac{T_x - T_y}{T_x + T_y}. \quad (2.3)$$

The phase shifts introduced from the Pockels cell for the + and - circular polarization states of the laser are

$$\delta_{\pm} = \pm \left(\frac{\pi}{2} + \alpha \right) - \Delta. \quad (2.4)$$

where α is a phase shift which is symmetric between the states resulting in same-signed linear polarization components between the + and - laser states and Δ is a phase shift that is asymmetric resulting in linear polarization components between the + and - laser states which is opposite in sign. The asymmetry in the intensity of the laser is given by

$$A_{PITA} = \frac{\Delta\epsilon}{\bar{T}} \sin 2\Theta \quad (2.5)$$

where \bar{T} is the averaged value of the maximum T_x and minimum T_y transmission and Θ is the angle with respect to the T_x axis. In practice, since both α and Δ are independent parameters this effect can be tuned away. Since the intensity asymmetry A_{PITA} of the laser manifests itself as a charge asymmetry, measurements of the charge asymmetry can be made against electronically induced changes to Δ in a measurement referred to as PITA Scan. The slope of this data reveals the sensitivity to Δ .

2.1.5 Beam Position Monitors

The electron beam position in the beam line is measured by various beam position monitors (BPMs); there are located at various places on the beam line across the entire lab. BPMs provide a range of useful functions from assisting beam transport to providing useful information during experiments. Transport of the beam is managed by constant feedback from beam position monitors (BPM) whose feedback is used to determine setting for quadrupoles which maintain beam focusing and dipoles which bend the trajectory.

The BPMs utilized in the experimental hall consist of four wire striplines which function as antennae oriented parallel to the beam line, each separated by 90° and rotated

by 45° with respect to the vertical and horizontal plane. A current independent method can be used in order to calculate a relative beam position to the antennae. As the beam passes by these antennae a current is induced. The relative position of the beam with respect to the stripline wires is ascertained by taking the respective asymmetry of the induced current readouts A_j from the stripline antennae measurements I_j where g_j is a gain-normalization factor and the underscript j identifies the stripline pair.

$$A_{x,st} = \frac{I_x^+ - g_x I_x^-}{I_x^+ + g_x I_x^-} \quad (2.6)$$

The spatial position of the beam in lab coordinates can then be calculated from this raw BPM data through the following calculation

$$\begin{bmatrix} X \\ Y \end{bmatrix} = \frac{D}{2} R(45^\circ) \begin{bmatrix} A_x \\ A_y \end{bmatrix} \quad (2.7)$$

where $R(45^\circ)$ is the 2D rotation matrix for $\theta = 45^\circ$ and D is the distance between striplines in the BPM.

2.1.6 Wire Scanners / Harps

Harps are used to measure both the beam's width and the beam's absolute position and are located at several positions along the beam line. The harp consists of three wires—each separated by 45° such that the first and third wires are perpendicular to each other—attached to a ladder and contained within the vacuum of the beam pipe. The ladder of the harp is remotely controlled and can be extended “swiped” through the beam; as the wires pass through the beam the charge collected on the wires is passed to a readout along with the total number of steps the motor controller has been extended. These signals are then used to determine the width and position of the beam.

Harps, located before and after the PREX-II target, were used during the PREX-II and CREX experiments to maintain assurance that spot size of the beam was within tolerance.

Prior to CREX an additional harp was installed upstream of the Møller polarimeter solenoid as a means of ensuring that the angle of the beam as it entered the target holding field was minimal.

2.1.7 Energy Measurements

An additional BPM, given the name BPM12X, is used to measure the deflection of the beam by a dipole located at the point of maximum curvature in the arc leading into the experimental hall. The angular deflection for a charged particle in a field is given by

$$\theta = \frac{e}{p} \int B \cdot dL \quad (2.8)$$

where p is the momentum, e is the charge, B is the field strength. Changes in the deflection of the beam are therefore inversely proportional to changes in the momentum (assuming of course the field stays constant). These readings are fed into the fast feedback system described in section 2.1.10.

2.1.8 Beam Current Monitors

There are three types of hardware used to monitor beam current intensity at the lab—beam current monitors (BCM), Faraday cups, and the Unser monitor [49]. The Unser monitor is a parametric current transformer which is calibrated against a known nominal current after which it can deliver an accurate signal but it very sensitive to magnetic fields and temperature shifts. However, this unit has the tendency to drift over relatively short periods of time and is not used for production measurements where it's important for beam current readings to be consistent over time so that counts can be properly normalized to current. The monitor is, however, useful for the calibration of the RF units. The RF units are cylindrical wave guides which are tuned to the beam frequency which allows for the resonance mode to be excited in such a way that the voltage signal produced is proportional to the beam current. The measurements taken from the

RF units are recorded into any currently running DAQ systems (which are collecting that information) on a helicity cycle-by-cycle basis. Integrated averages at the rate of a few per second are recorded into the EPICS system for archival purposes. These RF units do produce non-linear responses at low beam currents and should be occasionally checked to ensure that the response over production run currents is indeed linear.

2.1.9 Charge Feedback System

The BCMs, described in section 2.1.8 also provide the data that drives the parity systems charge feedback system which works to minimize the charge asymmetry during parity running [47]. The charge feedback system provides small adjustments to the Pockels Cell voltages based on predetermined experimentally measured relationships between the PITA voltage changes and the measured charge asymmetry, the aforementioned PITA scans, such that it is well understood how much to change the PITA voltage push towards a zero charge asymmetry. Information from the BCMs is used to calculate a voltage change to induce the required phase offset Δ which is defined in eq. (2.4) to minimize A_{PITA} and hence A_Q . A comprehensive understanding of BCM response and ensuring that the BCM response is linear in the desired current range is critical to this feedback system.

2.1.10 Fast Feedback System

The fast feedback system [50] is designed to correct and stabilize the beam energy. Small deviations which can effect beam position and spot size down the line and while magnet settings cannot be rapidly controlled the energy of the beam can be. Data from energy measurements, described in section 2.1.7, taken as the electron beam is bent through the arc leading into the experimental hall is sent to the feedback system. The feedback system uses this input to compute the necessary signals to send to sets of correctors which make effectively real-time changes required to suppress beam motion [51]. These correctors are select RF cavities, referred to as energy verniers, which are placed at

the exit of the accelerator in order to alter the energy picked up by the electrons while in the cavity before they are passed into to the experimental halls. Through this method, the beam position can be reasonably stabilized.

2.1.11 Mott Polarimeter

JLab's Mott Polarimeter [52] is housed at the injector prior to the acceleration of electrons into the accelerator.

The Mott scattering cross section eq. (1.8) has a spin-dependent term for transversely polarized electrons. In order to analyze the polarization of the beam the electrons must first be rotated by 90° . The polarimeter has four detectors—a pair for left and right scatters and a pair for up and down scatters. In general, the Mott scattering physical left-right asymmetry $A_{Mott}^{L/R}$ can be simply related to the beam polarization by:

$$A_{Mott}^{L/R} = \frac{N_R - N_L}{N_R + N_L}. \quad (2.9)$$

With a polarized source such as that at JLab where beam polarization can be controlled by the laser polarization and presents zero-risk of cross-sectional changes to this formulation can be extended [53]. False asymmetries induced by the instrumentation can be teased out easily by using an alternative formula where N'_R and N'_L and the left and right counts when beam polarization/helicity is reversed and taking the asymmetry of the geometric means $A_{Mott}^{G.M.}$ of the matching states:

$$A_{Mott}^{G.M.} = \frac{\sqrt{N_R N'_L} - \sqrt{N_L N'_R}}{\sqrt{N_R N'_L} + \sqrt{N_L N'_R}}. \quad (2.10)$$

The measured Mott scattering asymmetry is related to the beam polarization P_{beam} through the effective Sherman function S_{eff} , which is a theoretical quantity, by:

$$A_{Mott} = S_{eff} P_{beam}. \quad (2.11)$$

2.2 Hall A

2.2.1 Compton Polarimeter

Compton polarimetry is based off of elastic electron-photon scattering—also known as Compton scattering. The measurement, which is minimally invasive, can be run during the main experiment without loss of beam quality; this is a distinct advantage of Compton polarimetry over other methods. The Hall A Compton polarimeter optic cavity is set off

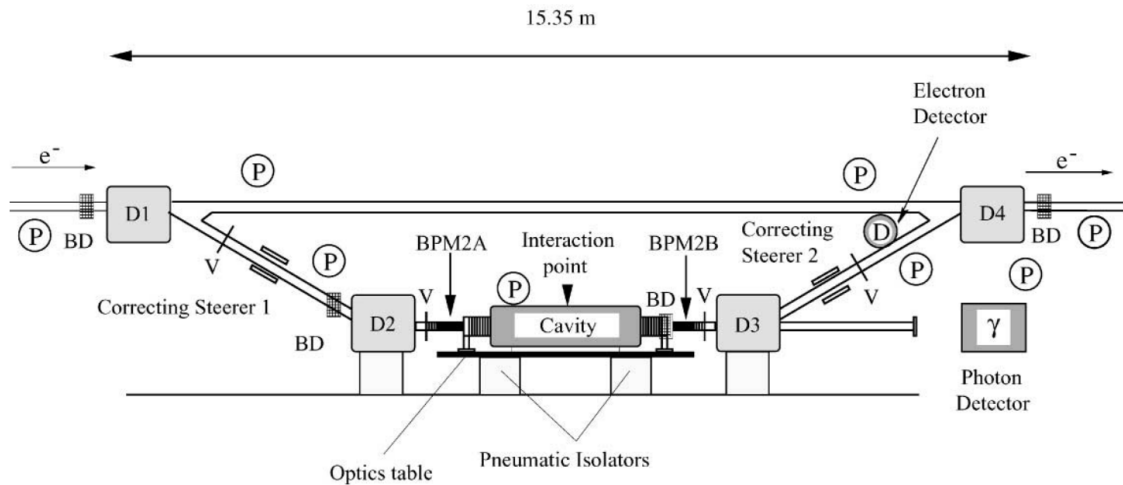


Figure 2.4: Diagram of Jefferson Lab Hall A Compton Polarimeter. Two dipoles D1 and D2 divert the electron beam from the main beam line to the laser table optics cavity. Dipoles D3 and D4 return the electron beam back to the main beam line. Compton back-scattered photons are detected at the photon detector while Compton scattered electrons are detected at the Electron detector.

of the main beam line by means of a chicane controlled by four dipoles which bend and align them beam in-to and out-of the chicane [54]. The purpose of placing the polarimeter off the beam line is to separate the beam from the Compton back-scattered photons which must be detected. The photon source of the Compton Polarimeter is a one-watt green laser. The electron beam is directed into a high-intensity Fabry-Perot optical cavity. The cavity acts as temporary "storage" for the laser beam as photons bounce back and forth between mirrors; this allows for a higher rate of electron-photon interaction as each photons have multiple chances to interact with the passing electrons. The polarized

electrons of the beam scatter from the circularly polarized photons stored in the cavity. Back-scattered photons picked are up by a photon detector and scattered electrons, which become momentum-sorted by the dipoles which return the electron beam from the chicane to the main line, can be analyzed for polarization measurements (although the electron detector was not used during the PREX-II and CREX experiments). Back-scattered photons which are picked up by a detector are analyzed for polarization measurements. In order to subtract out backgrounds the Compton polarimeter laser routinely alternates between on and off stages—with data collected while off being used to subtract out measured background.

$$A_{meas} = P_{beam} P_{\gamma} A_{\mathcal{L}} \quad (2.12)$$

The asymmetry which results from the Compton scattering cross-section's spin-dependent terms can be measured. This measured asymmetry A_{meas} , shown in eq. (2.12), is dependent on the polarization of the beam P_{beam} , the circular polarization of the laser P_{γ} , and the calculated longitudinal analyzing power $A_{\mathcal{L}}$; hence, by measuring the asymmetry, and having a well-constrained understanding of laser polarization and of the computed longitudinal analyzing power the beam polarization can be derived.

Electron Detector

Although unused for the PREX-II/CREX analysis an electron detector has been used to analyze the dipole-dispersed scattered Compton electrons. The detector, seen in the upper-right of fig. 2.4, is a set of four (4) radiation-hard diamond detectors all aligned in the same direction and are used to sort out qualifying electron tracks. The detector is situated in an orientation such that the strips that a dipole-dispersed electron track passes through can be used to determine the radius of curvature as it passed through the dipole (whose field is known) which can then be related to the energy of the electron. As such, a properly corrected strip-by-strip asymmetry calculation is more-or-less a measurement of the Compton scattering spectrum asymmetry. This data is fit to theoretical predictions

for a determination of the polarization.

2.2.2 Møller Polarimeter

The Møller polarimeter is the second polarimetry device in Hall A. Similar to the measurable Compton scattering asymmetry the Møller cross-section contains spin-dependent terms which manifest themselves as a large and measurable asymmetry between the helicity states of the beam. Because Møller polarimetry is destructive to the beam the main experiment must be put on a brief hold while measurements are made. This will be covered in much more detail in chapter 3.

2.2.3 Rasterization

At high currents the electron beam can locally dump large amounts of energy into targets causing them to overheat adding thermal noise which cannot be regressed out or fail in a much shorter than expected time. The PREX-II ^{208}Pb targets are designed for relatively low power absorption rate of less than 100W with a continuous experimental current of $70\mu\text{A}$. In order to slow down inevitable damage the beam is spread out over a larger area of the target; a rasterization system comprised of vertically and horizontally oriented dipoles upstream of the target are used to deflect the beam. A photo of ^{208}Pb targets taken post-experiment are shown in fig. 2.6 where thermal wear from the beam and target failure from long-term usage are shown. An oscilloscope in the Hall-A counting house monitors the current in the raster and is frequently referenced to ensure that the raster is running.

2.2.4 Hall A High Resolution Spectrometer (HRS)

The Hall-A HRS system is a pair of spectrometers aptly named LHRS (left) and RHRS (right). The spectrometers consist of a magnetic optics system used to control scattered electrons and a detector system. Each HRS consist of two quadrupoles, which

focus towards a sector dipole which bends at a 45° angle, a third quadrupole, scintillators which act as triggers and a pair VDCs [55] which allow for particle tracking. The HRS system itself was not designed for PVES experiments such as PREX and CREX [56]. The intent of the design of the HRS system was to provide a high momentum resolution over a very small cross section. It was this design feature that made the HRS system rather ideal for parity-violating experiments. The spectrometer is sufficiently capable of separating the small energy differences between the inelastically-scattered and elastically-scattered events. Seizing on this resolution capability PREX and CREX utilized the spectrometer without using the HRS's native detectors but rather using their own scintillating quartz detectors.

During PREX and CREX the VDCs were not used for experimental data taking. The VDCs were utilized during special low-current runs and provided tracking data for calibration to ensure that the elastic scattering peak was being captured properly or to check spot size using a special carbon hole target with the rastered beam.

2.2.5 Data Acquisition Systems

Data Acquisition Systems (DAQs) collect electronic data from the experiment and store it. There are a variety of DAQs in the Hall—Counting DAQ, Parity DAQ, Møller DAQ, Compton DAQ. Each of these collects information from its respective system.

2.2.6 Beam Modulation Coils / Energy Vernier / Dithering

The PREX-II and CREX experiments also made use of beam modulation coils which are used to modulate the beam. In total there are seven modulation coils are used to independently modulate the beams horizontal position x , vertical position y , the horizontal angle off of the longitudinal θ_x and the vertical angle off of the longitudinal θ_y . Beam and angle positions relative to the target are collected by the BPMs immediately upstream of the target. Modulation of the beam energy is handled by an energy vernier. This energy

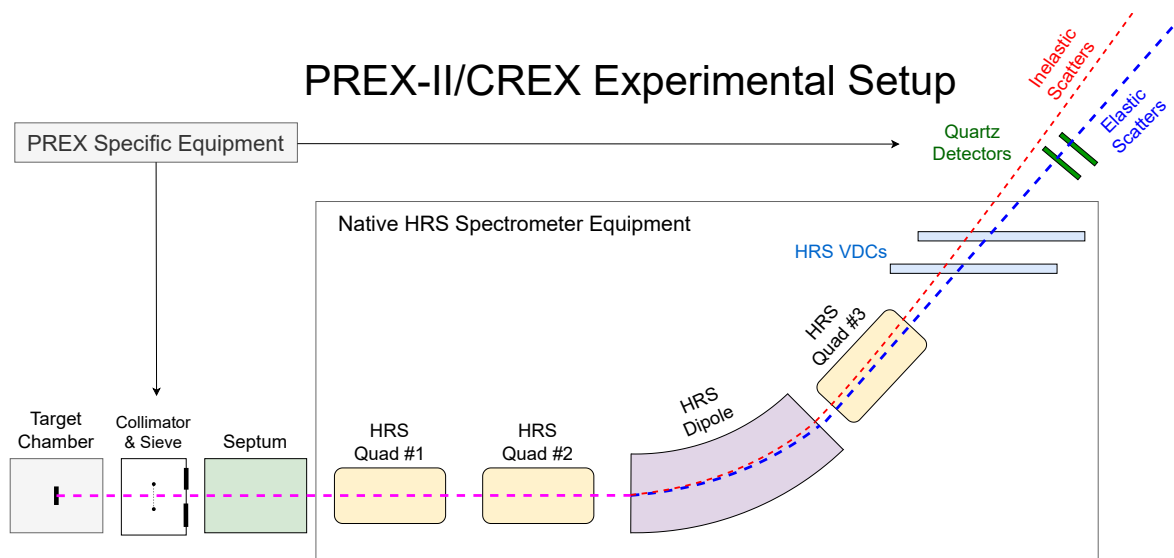


Figure 2.5: Basic Schematic of PREX/CREX Setup. (Not drawn to scale.)

modulation information is collected by BPM12X located in the arc that bends the beam into the experimental hall.

Modulation of the coils is controlled by software and occur during regular intervals when active. The coils and energy vernier are modulated in succession during this period. This modulation effectively functions as an exaggeration of normal beam parameter changes which under normal conditions can be small and difficult to pin down an exact sensitivity to. This process is referred to as dithering. Careful monitoring of this data is necessary in order to avoid unnecessary data losses and maximize the usefulness of parity data collected. Experimental data that occurred during beam modulation is cut from the general data in the analysis; thus, there's a balance to be struck as to how long and how frequent these modulation periods are. Data from this dithering can be used to directly apply corrections for position, angle and energy beam parameters, or it can be used to constrain a regression analysis on data taken during normal production run.

2.3 PREX/CREX Specific Experimental Equipment

This section will detail items which are specific to the PREX experiment and not native parts of the JLab facility.

2.3.1 PREX-II/CREX Targets

The PREX-II and CREX experiments utilized a dual target ladder system—one target ladder held production targets while the other target ladder held optics targets—for which the orientation can be seen in fig. 2.8. The Cu made production target ladder was positioned horizontally and perpendicular to the beam line and was cryogenically cooled down by a liquid helium line held at 15K and 12 atm. The optics ladder was positioned 45° off the horizontal and was water cooled. The ladders were controlled by a motion system which was remotely controlled by a GUI. The target ladder contained isotopically enriched lead targets (six of which were used during the PREX-II experiment), a carbon target (1% radiator), a carbon hole target used for alignment and a ^{40}Ca target. For CREX a greater than 99.9% isotopically pure ^{48}Ca target was added to the ladder in a reserved position. The optics ladder contained a water target for calibrating measurements of the scattering angles and a carbon target (0.2% radiator).

The ^{208}Pb targets were diamond-sandwiched in order to facilitate better heat dissipation and contact areas with the Cu ladder were covered in Ag paste. Diamond is an excellent heat conductor and, since it has an equal number of protons and neutrons, has zero isospin. Targets used during the original PREX experiment were diamond coated and evidence suggested that an adequately thick diamond coating could provide enough thermal protection extending the life of the target long enough to collect a sufficient amount of data from it. Lead foil thickness of the targets was approximately 0.5mm with the diamond coating being approximately 0.25mm. With sufficient rasterization of the beam the Pb targets were expected to withstand $70\mu\text{A}$ of beam current.

2.3.2 Collimation and Sieve

The PREX/CREX experiment setup includes collimation and a retractable sieve the location of which is shown in fig. 2.7 and general schematic of in fig. 2.9. The sieve is a thick collimation plate with a predetermined pattern of drilled holes. The holes in the



Figure 2.6: Post-experiment photo of PREX-II ^{208}Pb targets. Left-target shows signs of minor thermal wear in the shape of the raster. Right-target shows a target which reached thermal failure.

sieve allow for the distinct identification of points during the reconstruction of events; this allows for the optimization of the reconstruction matrix and allows for a determination of the uncertainty on the angular reconstruction.

2.3.3 Septum

The minimum design angle that the HRS system can accommodate is approximately 12° . Since PREX-II and CREX required capturing data on electrons scattered at a laboratory angle of approximately 5° a septum magnet pair was used to bend these heavily-forward 5° angle scatters to the minimum design angle of the spectrometer.

2.3.4 Quartz Detectors

Quartz detectors were the main detectors used for production run data collection; two quartz detectors were used per arm for a total of four detectors. Images of detectors can be seen in fig. 2.10. The detectors were made of radiation thin quartz—hardened

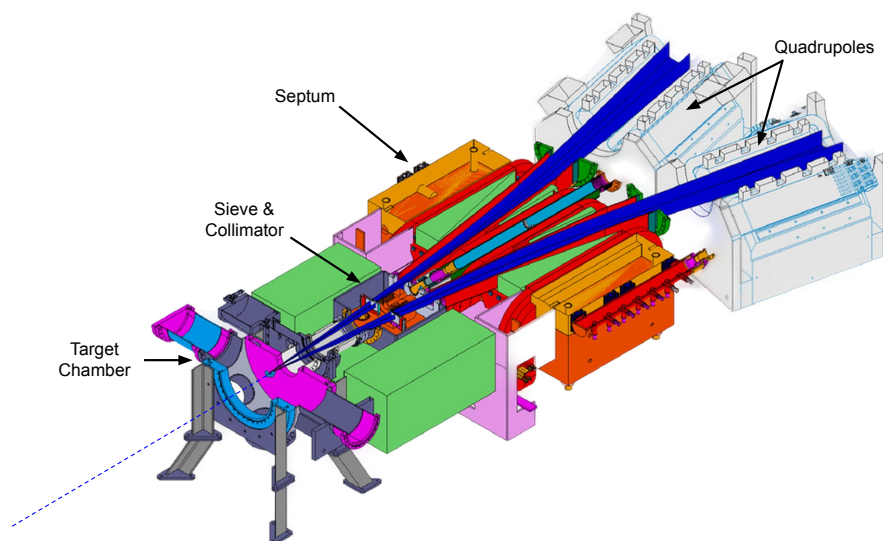


Figure 2.7: Schematic of PREX-II setup prior to electron scatters entering into the first HRS quadrupoles. The electron beam (blue dashed line) strikes the target; scattered beam electrons (denoted by dark blue bands) potentially pass through the sieve and are collimated prior to entering the septum which bends the electrons, selected for an $\approx 5^\circ$ scattering angle, outwards to accommodate the minimum separation angle of the HRS system $\approx 12^\circ$.

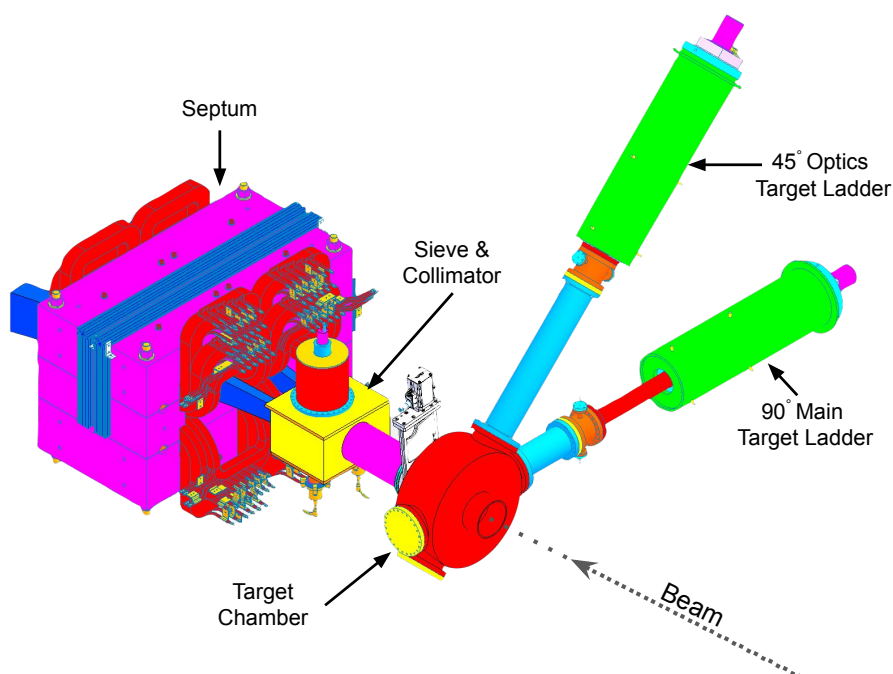


Figure 2.8: Basic Schematic of PREX/CREX experimental apparatus with visualization of the target arms containing the main target ladder and optics target ladder.

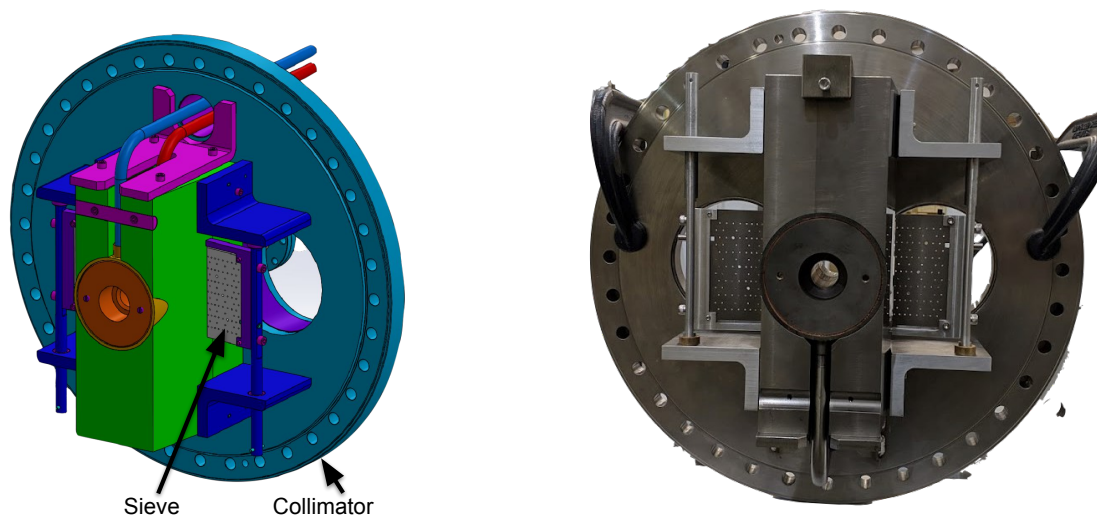


Figure 2.9: Left panel: Basic CAD schematic of the sieve/collimator component of the PREX-II/CREX experiment. Sieve plates can be rotated in and out of the scattered beam as necessary to aid in event reconstruction. Right-panel: Photo of sieve/collimator apparatus.

fused silica 5mm thick, 35mm wide and 160mm long—connected to a photomultiplier tube capable of handling multi-gigahertz flux rates. The quartz detectors were placed such that they were perpendicular to the scattered electron trajectories and positioned such that they would capture only the elastically scattered peak. Cherenkov light from electrons passing through the silica is internally reflected towards the PMT where the signals are integrated.

Data from the detectors is integrated over each helicity cycle. Detector non-linearities were benchmarked during the experiment and constrained to below 0.5%.

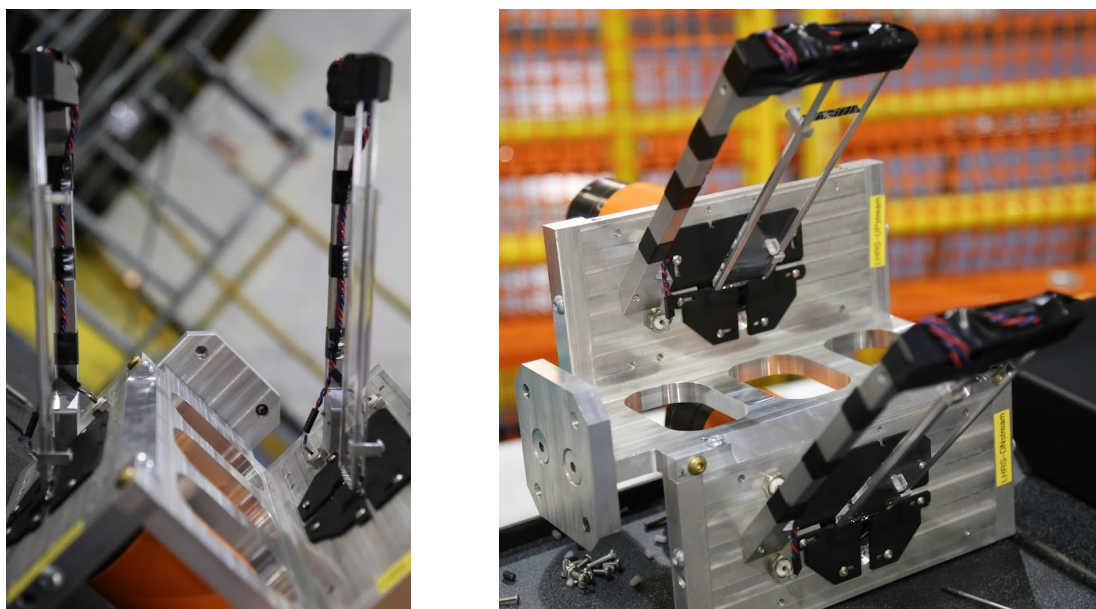


Figure 2.10: Images of PREX-II/CREX integrating detectors. Silicon light guides are attached to orange-colored PMTs. [Images courtesy of Dustin McNulty.]

Chapter 3

Møller Polarimetry

Polarimetry at particle accelerators generally comes in three forms: electron scattering off of heavy nuclei—Mott scattering; scattering off of a polarized target—Møller Scattering; or the scattering from optical photons of a well-defined frequency—Compton Scattering. All three of preceding techniques are utilized at Jefferson Lab; Compton polarimetry and Mott polarimetry were briefly overviewed in section 2.2.1 and section 2.1.11 respectively.

Møller scattering was first suggested as a polarimetry tool in 1957 [57] to measure the polarization direction of beta-decay emissions using the simultaneous observation of the two Møller electrons in order to separate out Møller scatters from other background events. The first successful demonstration of using Møller scattering as a polarimetry tool on a polarized electron source was performed in 1975 at SLAC [58]. Polarimetry measurements are fundamental to many of the precision experiments at Jefferson Lab which are utilizing polarized beam and are critical for experiments which use parity-violating scattering as a probe of the Weak Force. The focus of this chapter will be on the Møller polarimeter and Møller polarimetry as it was the author's primary contribution to the PREX-II and CREX experiments.

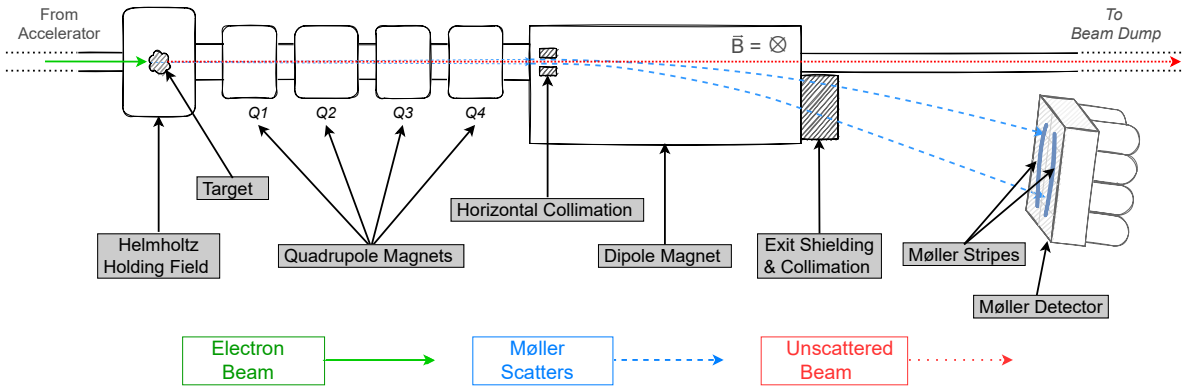


Figure 3.1: Mock up of the Jefferson Lab Hall A Møller polarimeter (not drawn to scale).

3.1 JLab Hall-A Møller Polarimeter

The Jefferson Lab Hall-A Møller Polarimeter [59] consists of a cryogenically cooled superconducting Helmholtz coil set in which the targets are held. Four quadrupole magnets are used to steer the scattered Møller electrons away from the beam electrons as they continue downstream; scattered Møller electrons must be successfully steered into dipole magnet which bends and sorts the Møller electrons by momentum as they head towards the detector. The scattered Møller electrons which are successfully steered through the spectrometer find themselves at the detector—a lead glass-fiber calorimeter. A mockup of the polarimeter can be seen in fig. 3.1.

3.1.1 Helmholtz Holding Field

The Hall A Møller polarimeter is what’s referred to as a “brute force” design which utilizes a strong magnetic field to bring a ferromagnetic target foil to magnetic saturation. In order to achieve the required field required to bring the target foil to saturation a superconducting cryogenically-cooled split-coil Helmholtz magnet is utilized; this setup provides a constant field along the beam line axis. This magnetizes the target foil in the direction of the beam line axis aligning the spin-unpaired electrons in the target foil in the direction of the electron beam. The holding field magnet is technically capable

of achieving a 5T field although lab operating standard limit the current to 80A which is around a 4.25T field strength which is sufficient to saturate the target foil to [60]. For the PREX-II and CREX experiments the target foil was held in a 4T field to ensure saturation. The Møller polarimeter target ladder sits in the center of the setup, has four target mounts containing 13 μm Cu, 10 μm Fe, 4 μm Fe and a 1 μm Fe foils. The 10 μm and 4 μm Fe foils, which were used in the PREX-II and CREX experiments, have a purity rating of 99.99%. The foil ladder arm is locked into place such that the plane of the foils are perpendicular to the beam.

3.1.2 Quadrupoles

The Møller polarimeter the quadrupoles are used to focus and steer the Møller electrons towards the dipole. For low-energy experiments such as PREX-II the quadrupole focusing is necessary to steer the Møller scattered electrons away from the beam line while for high-energy experiments the quadrupoles are critical in pulling the scattered Møller electrons away from the beam line center. The particular settings of the four quadrupole (and dipole) magnets is referred to as the magnet optics. Optimal optics steer a sufficient kinematic range of Møller electrons to the detector. Each quadrupole is capable of producing a 0.6T field at the pole tips although non-linear effects begin to occur as the magnets reach saturation.

3.1.3 Møller Dipole

The Møller dipole is used to bend the electrons below the beam line towards the detector. The apparatus as a whole consists of iron dipole magnets which sandwich a steel vacuum box. At the center of the box there is a magnetically shielded beam pipe which shuttles the remnants of the beam downstream with minimal bending. At the entrance to the dipole horizontal lead collimators which can be remotely adjusted and are used to control acceptance. The dipole vacuum box is sealed off by a 100 μm thick titanium window. Particle scatters and gamma emissions from electrons passing through

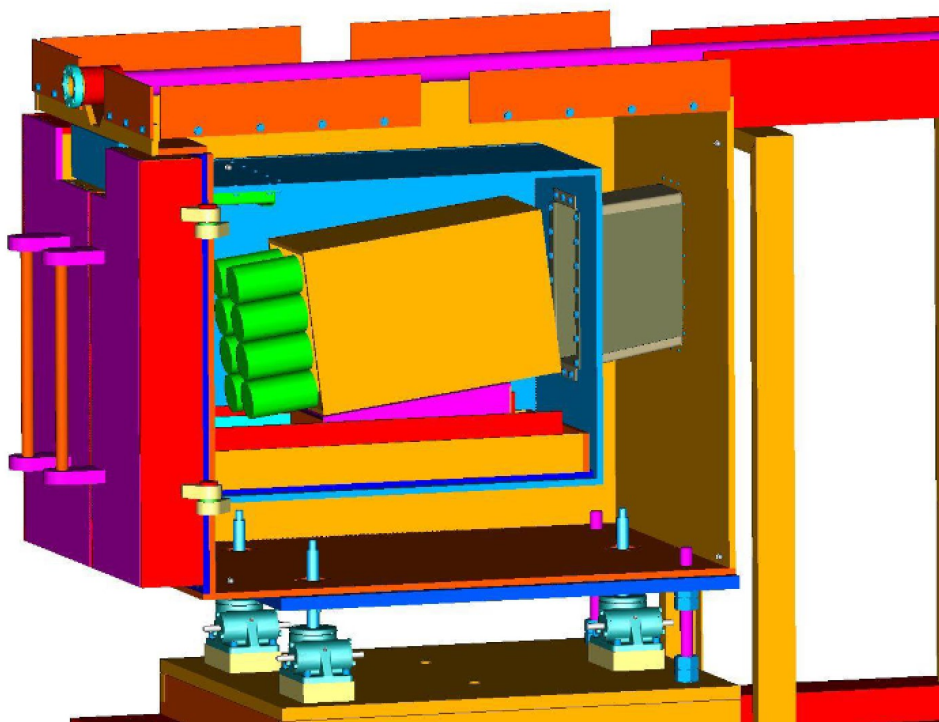


Figure 3.2: The Jefferson Lab Hall-A Møller polarimeter detector. The detector is contained in a shielded box (lead bricks filling box not shown) to protect it from backgrounds. Electrons successfully transported through the spectrometer enter through the box window, strike the lead-fiber bricks (yellow, actually composed of four blocks) and scintillation light is collected by eight PMTs (green).

this window are absorbed by a lead block of radiation shielding which also can act as collimation. Møller scattered electrons which are transported successfully through the dipole then travel in open air towards the Møller detector.

3.1.4 Møller Detector

The Møller detector shown in fig. 3.2, is a scintillating fiber and lead calorimeter—a detector in which scintillating fibers are laid into scored lead plates which are then assembled into a block. The fibers are then bundled and the light guide is connected to photomultiplier tubes PMTs. The left and right arms are each separated into upper and lower blocks; each block is equipped with two 2-inch PMTs leaving each detector arm separated into four channels. The left and right arms are ideally situated such that the vertical plane of the beam line passes between them. Particles enter the detector blocks,

shower in the lead, and cause scintillation in the fibers; the scintillation light is channeled down the fibers to the PMTs. Analog signals from the PMTs—the individual signals from all eight PMTs, the left-arm and right-arm sums, and the total sum—are then converted to digital signals via an analog-digital converter (ADC) and recorded in the Møller DAQ. An example of these signals received over the course of a PMT voltage calibration run can be seen in fig. 3.4.

The high-voltage settings fig. 3.3 of the PMTs are set up so that the Møller peak seen by each PMT corresponds to the same channel of at least 300 and are controlled via a GUI. For PREX-II the Møller peaks seen by each PMT were aligned to channel 360 and for CREX the Møller peaks seen by each PMT were aligned to channel 300 (example images shown for individual PMTs in fig. 3.4 and left-side right-side sums in fig. 3.5). The ADC signals were verified prior starting polarimetry measurements to ensure that the detector was functioning properly.

In addition to being passed to the ADC the left-arm and right-arm sums are passed to a signal discriminator which identifies the signal pulse peaks. Background events captured in the detector are suppressed through the use of a timing cut. Signals from the discriminator are then passed to a time-to-digital converted (TDC) where timing data is recorded. The discriminated signals are also passed to two different programmable logic boards (PLU) which identifies events as singles, coincidences or accidental coincidences. The PLUs also collect data from the BCM unit, helicity signal line and clock. Data is collected by two independent PLUs so that results from these two systems can be compared to ensure integrity of the data during analysis. Data from the PLUs is passed to and integrated by a scaler data acquisition unit.

3.2 Møller Scattering Physics

Møller Asymmetry

Møller scattering [61] is an extremely well studied elastic- interaction for which QED

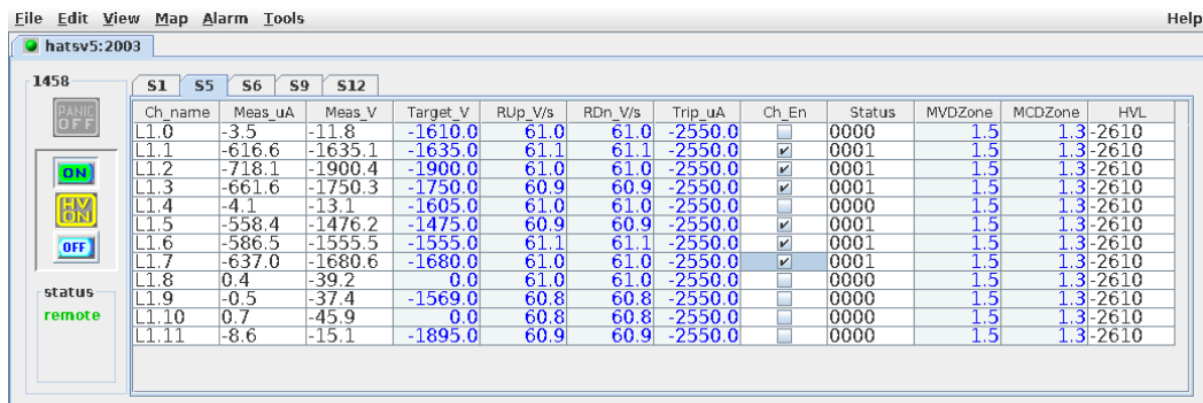


Figure 3.3: Møller polarimeter high-voltage control panel GUI with PMT selection settings for CREX optics which utilized the lower 6PMTs.

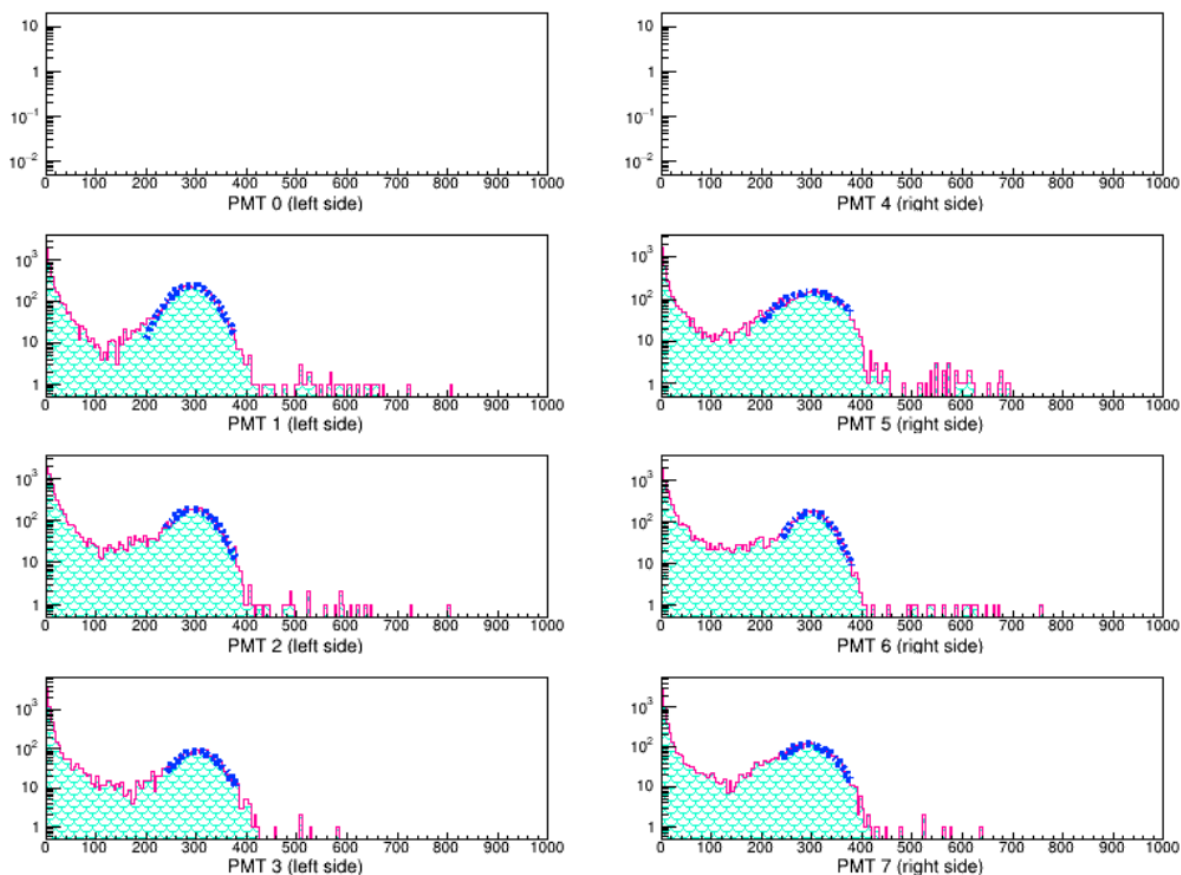


Figure 3.4: Møller polarimeter PMT signals from ADC data. High-voltage for the PMTs are individually set in order to align the Møller peaks to the same channel (here 300).

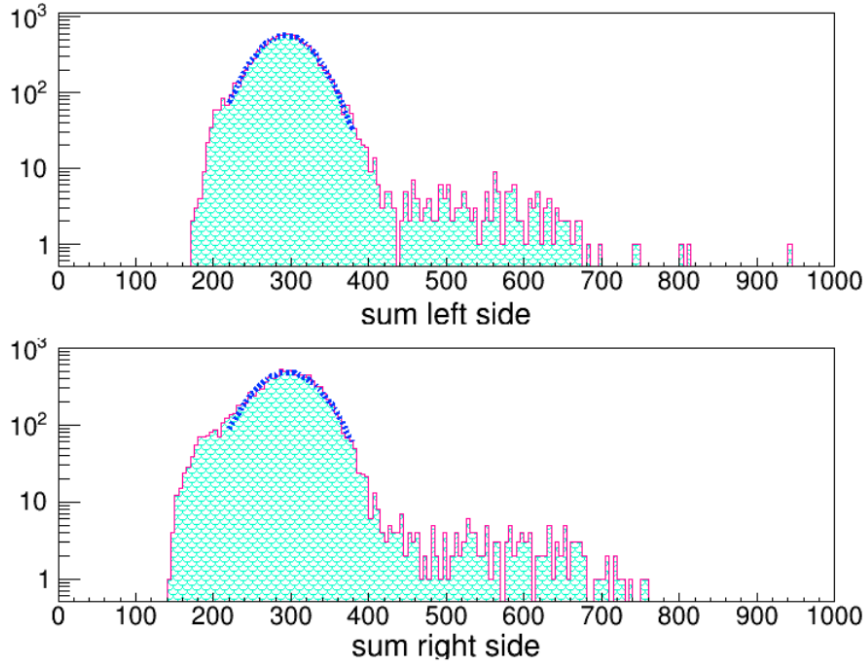


Figure 3.5: Left arm and right arm PMT signal sums. Threshold cuts set at channel 180.

predicts a precise spin-dependent scattering asymmetry. The Feynman diagrams for these types of scatters can be seen in figure fig. 3.6.

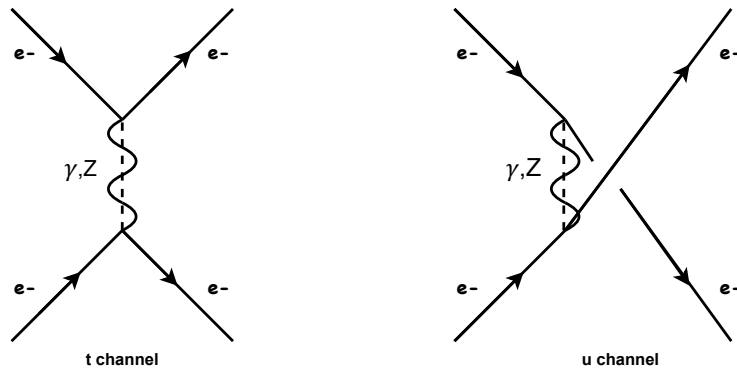


Figure 3.6: Møller scattering Feynman tree-level diagrams. Both t-channel and u-channel are required since we have two identical fermions scattering. Both γ and Z_0 interactions are shown for completeness although the weak Z_0 contribution is negligible compared to γ contribution.

The unpolarized Møller scattering cross section in the ultra-relativistic limit is:

$$\frac{d\sigma_0^M}{d\Omega} = \frac{\alpha^2 (3 + \cos^2 \theta^*)^2}{s \sin^4 \theta^*} \quad (3.1)$$

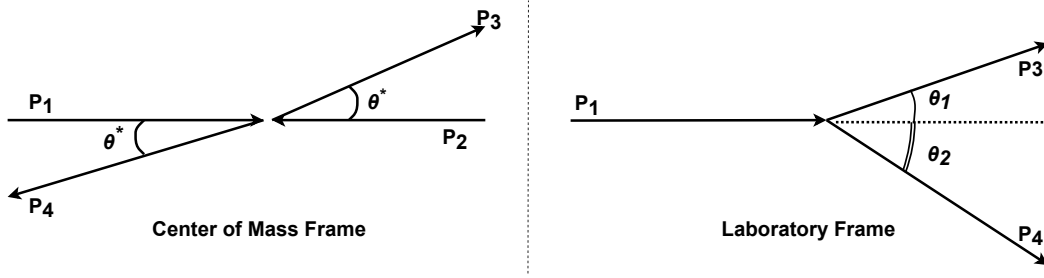


Figure 3.7: Møller scattering diagrams. Left-panel: center-of-mass representation; Right-panel: laboratory frame representation.

where θ^* is the center-of-mass scattering angle and the center-of-mass energy squared $s = (2E^*)^2$ given by where E^* is the center of mass energy of each electron leaving the Møller cross section proportional to $1/E^2$.

The polarized cross section for purely QED Møller scattering in the ultra-relativistic limit with polarization vectors P_{beam} and P_{targ} can be compactly written as

$$\frac{d\sigma^M}{d\Omega} = \frac{d\sigma_0^M}{d\Omega} \left(1 + \sum P_{beam,i} P_{targ,j} A_{ij} \right) \quad (3.2)$$

The non-zero A_{ij} QED terms are summarized below under the convention that that the direction of target polarization and the direction of the beam particle are both in the z-direction.

$$A_{zz} = \frac{\sin^2 \theta^* (7 + \cos^2 \theta^*)}{(3 + \cos^2 \theta^*)^2}$$

$$A_{xx} = -A_{yy} = \frac{\sin^4 \theta^*}{(3 + \cos^2 \theta^*)^2} \quad (3.3)$$

$$A_{zx} = A_{xz} = \frac{2 \sin^4 \theta^* \cos \theta^*}{(3 + \cos^2 \theta^*)^2}$$

Collectively, the values in eq. (3.3) are known as the Møller analyzing powers. eq. (3.2) can be written in terms of the longitudinal component A_{zz} and the remaining transverse combinations which we can call A_t with P_z^{beam} and P_t^{beam}

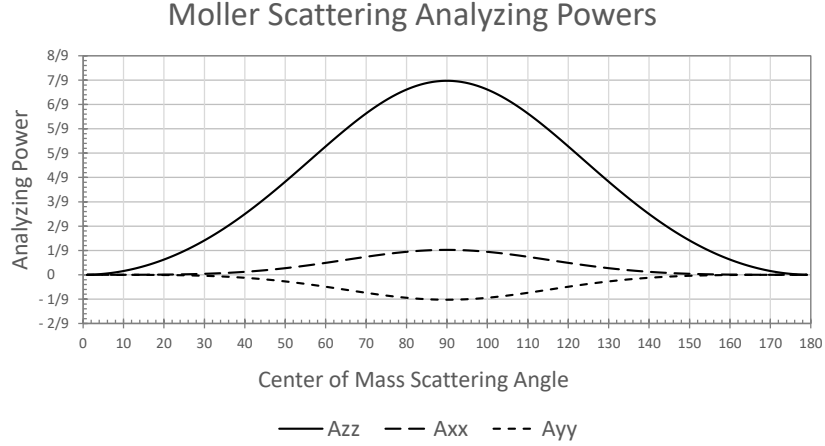


Figure 3.8: Møller analyzing powers A_{zz} , A_{xx} and A_{yy} plotted as a function of θ^* . The analyzing powers reach maximum value when the center-of-mass scattering angle is 90° . A_{zz} maxes out at $\frac{7}{9}$ while the A_{xx} and A_{yy} components max out at $\pm\frac{1}{9}$

Taking these terms and summing over them as prescribed in eq. (3.2) we can arrive at the following form presented by Swartz [62] where A_t represents all transverse polarization combinations while A_{zz} is strictly the parallel and anti-parallel configurations and P_z and P_t are the parallel/anti-parallel or transverse polarization vector components.

$$\frac{d\sigma^M}{d\Omega} = \frac{d\sigma_0^M}{d\Omega} (1 + P_{beam,z}P_{targ,z}A_{zz} + P_{beam,t}P_{targ,t}A_t \cos(2\phi - \phi_{beam} - \phi_{targ})) \quad (3.4)$$

The Hall A Møller polarimeter's brute force setup which magnetically saturates the target to ensure that P_{beam} and P_{targ} lie along the same axis along with the locked in place target ladder then simplifies the polarized cross-section to

$$\frac{d\sigma^M}{d\Omega} = \frac{d\sigma_0^M}{d\Omega} (1 + P_{beam,z}P_{targ,z}A_{zz}) \quad (3.5)$$

Any reference to analyzing power throughout the remainder of this thesis will strictly be referring to the longitudinal A_{zz} component. This analyzing power quantity is the basis for Møller polarimetry. The process of calculating the analyzing power will be detailed in section 3.5.

Møller Kinematics

The momentum of scattered Møller electrons is given by the following relationship,

$$p' = \frac{P_{beam}}{2}(1 \pm \cos \theta^*). \quad (3.6)$$

and is dependent only on the beam momentum and the center of mass scattering angle θ^* . Since Møller scattering is elastic and the masses are the same, in the center of mass frame the scattering angles are supplementary—they add up to 180° ; to avoid confusion, when center of mass scattering angle is referred to here it will strictly be the angle of the scattered beam electron. The lab scattering angle θ_L is given by

$$\tan^2 \theta_L = \frac{1}{P_b p'} \frac{2m_e}{E_0 + m} \frac{\sin^2 \theta^*}{(1 + \cos \theta^*)^2} \quad (3.7)$$

which through some quick substitutions and a small angle approximation can be simplified to

$$\begin{aligned} \theta_L^2 &= 2m_e \left(\frac{1}{p'} - \frac{1}{P_{beam}} \right) \\ \theta_L^2 &= \frac{2 m_e}{P_{beam}} \left(\frac{2}{(1 \pm \cos \theta^*)} - 1 \right) \end{aligned} \quad (3.8)$$

hence the lab angle of the scattered Møller electron is simply a function of beam momentum, which is held constant in laboratory conditions, and the center of mass scattering angle. The relationship between eq. (3.8), eq. (3.6) forms the spectroscopic basis for all Møller polarimetry.

3.2.1 The Levchuk Effect

One significant problem faced by Møller polarimetry is accounting for the momentum kicks the incident electron receives from the momenta of the Fermi-bound electrons of the target. This effect was identified and addressed by L.G. Levchuk [63] who, in pursuit of resolving large uncertainties in Møller polarimetry, had the insight to investigate what

effect the momentum of target electrons—which are not free but bound to their respective nuclei—would have on the Møller kinematics.

In a standard beam on stationary target the square of the center of mass energy is, in the high-energy limit,

$$s_0 = 2m_e E_b \quad (3.9)$$

The modified square of the center of mass energy s as proposed by Levchuk then becomes s_1 ,

$$s_1 = s_0 \left(1 - \frac{P_b \cdot \hat{n}}{m_e} \right) \quad (3.10)$$

where P_b is the momentum of the target-bound electron and \hat{n} is the beam-to-target-electron strike angle. In the laboratory frame, the Lorentz factor dependence for the lab momentum cancels out; this results in no change to the laboratory momentum [62]. The Levchuk modification to the square of the center-of-mass energy from the target-bound electron does, however, modify the laboratory angle. The standard Møller electron laboratory scattering angle given in eq. (3.8) becomes

$$\theta_L^2 = \underbrace{\frac{2 m_e}{P_B} \left(\frac{2}{(1 \pm \cos(\theta^*))} - 1 \right)}_{\text{Standard Møller Kinematics}} \underbrace{\left(1 - \frac{P_b \cdot \hat{n}}{m_e} \right)}_{\text{Levchuk Modification}} . \quad (3.11)$$

The Levchuk effect smears out Møller scatters tending to either increase or decrease both Møller electrons lab angle. This angle modification has the potential to be significant if the beam electron which was scattered off one of the innermost s-shell target electrons which have an average momentum of 90keV. Such a scatter would yield an approximately 17% angle correction; this alteration to the kinematics has the potential to present a significant correction to the analyzing power through lost Møller coincidence acceptance; care must be taken in developing optics settings that minimize the impact of this effect.

3.3 Møller Polarimetry

The cross-sectional helicity-dependent asymmetry for different beam-target spin orientations in Møller scattering eq. (3.5) can be exploited and opens up a method to measure the beam polarization. This QED Møller spin asymmetry has a rather large analyzing power which results in a rather large asymmetry ≈ 0.05 (assuming an approximate analyzing power of 0.75, an 8% target magnetization and 90% beam polarization). Unfortunately Møller polarimetry is destructive to the quality of the electron beam and therefore must be performed separate from the main experiment. The high scattering rates and large asymmetry do make Møller polarimetry an ideal tool for intermittent polarization measurements allowing precise measurements in a relatively short period of time.

Taking the standard difference over sum asymmetry as prescribed in eq. (1.16) and substituting in the polarized Møller cross-section given in eq. (3.5) we can arrive at an expected asymmetry in the ultra-relativistic limit

$$A_{meas} = P_{beam} P_{targ} \langle A_{zz} \rangle \quad (3.12)$$

where $\langle A_{zz} \rangle$ is the average analyzing power over the captured cross-section. This captured cross-section and its associated analysing power must be computationally calculated and the method of doing so is reviewed in section 3.5. After measuring the asymmetry it is possible to extract beam polarization by knowing the analyzing power.

3.4 Hall-A Møller Polarimetry Simulation

The Jefferson Lab Hall-A Møller polarimeter simulation—MOLPOL—is an application built on a GEANT4 framework. The MOLPOL geometry is constructed using standard GEANT4 geometries and is sized according to technical specifications and positioned according to Lab surveys; accurate positioning of physical elements is crucial to achieving

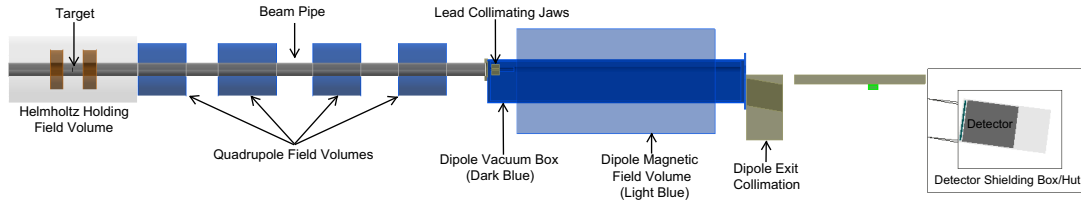


Figure 3.9: Rendering of Hall-A Møller Polarimeter in MOLPOL.

simulation results that accurately depict the captured cross section of the polarimeter. A visual depiction of the GEANT4 simulation geometry is shown in fig. 3.9.

3.4.1 Møller Generator

Since it would take a tremendous amount of time to let GEANT4 simulate the electron beam on target and produce a sufficient amount of Møller scatters MOLPOL, instead, utilizes a Møller pair generator. The Monte Carlo generator simulates pairs of Møller electrons within the target volume according to specified beam momentum and parameter spaces outputting Møller pairs.

In addition to the basic Møller kinematics, the generator also simulates the Levchuk effect and radiative corrections in the simulated interaction. Levchuk corrections, for the purposes of the work for PREX-II and CREX, were calculated using modified hydrogen wavefunctions to derive the cumulative distribution functions (CDFs) for polarized and unpolarized iron electrons [62] which were used in the Monte Carlo to randomize the selection of the target electrons bound momentum. The likelihood of the Monte Carlo'ed selection of a polarized or unpolarized event is determined from the input target polarization parameter.

Radiative corrections are calculated using a structure function approach for collinear radiation described in [64]. Events in the simulation are generated as a flat distribution in the center of mass frame and calculated weights are assigned for the Møller cross section and radiative corrections. After the generator has produced randomized Møller pairs GEANT4 handles the transportation of the electrons through the polarimeter.

3.4.2 Transport

Once the Møller electrons are generated GEANT4 takes over the work performing the simulation of the electrons through the detector. The primary non-drift transport components of the polarimeter simulation, whose physical descriptions were covered in section 3.1, are: a mapped solenoid field; four idealized quadrupole fields; and an idealized dipole field. Additionally, there are lead collimator jaws at the entrance to the dipole and lead collimation at the dipole exit.

Prior to the running of PREX-II, improvements were made to the GEANT4 simulation by including an solenoid field map which includes a near-complete extension of the fringe field; this produced noticeable differences in simulation results and was incorporated as a permanent feature. The use of field maps for the quadrupoles was investigated but was unable to replicate previous experimental data taken. Although, now, there is a fair amount of confidence that problems in replicating this data were a result of unknown beam orbit conditions. Given that knowledge a re-inspection on the use of those field maps against carefully controlled data that was taken during the CREX experiment may be in order.

Events which make it to the detector are recorded into a data file with the mean analyzing power being calculated in post-simulation analysis.

3.5 Calculating Analyzing Power

This section will briefly discuss the calculation of the analyzing power from simulation data. Due to the nature of the calculation the target polarization and the mean analyzing power are convoluted since only polarized electrons carry analyzing power. Let $A_{zz,i}$ be the analyzing power of a Møller coincidence electron, w_i be the associated weight of the simulated event which produced that electron and we will separate polarized vs.

unpolarized events keeping in mind that unpolarized events have zero analyzing power.

$$\langle A_{zz} \rangle' = \frac{\sum_i^{Pol} w_i A_{zz,i} + \sum_i^{Unpol} w_i A_{zz,i}}{\sum_i^{Pol} w_i + \sum_i^{Unpol} w_i} \quad (3.13)$$

The value $\langle A_{zz} \rangle$ can be extracted from $\langle A_{zz} \rangle'$ by dividing out by the simulated foil polarization used in the simulation.

From eq. (3.13) the previously discussed Levchuk effect section 3.2.1 becomes an issue when calculating the analyzing power. Ideally, the ratio of polarized to unpolarized coincidence events would be equal to the target polarization; in reality, this is not necessarily the case. The modified kinematics of the Levchuk-kicked electrons has the potential to knock them out of acceptance by terminating them on an unexpected aperture. This is primarily due to unpolarized K-shell (1S) electrons which can impart a momentum kick in the center of mass frame that results in a significant angle change in the lab frame by a few degrees. The large angle modifications caused by the Levchuk effect can cause coincidence losses and alter the actual ratio of polarized to unpolarized coincidence events; while these Møller scatters off of unpolarized electrons don't have any analyzing power these Levchuk losses do result in an overall change in acceptance causing a dilution of the denominator of eq. (3.13) which results in an overall higher analyzing power. A primary goal of developing a good optics solution for the PREX-II and CREX experiments was avoiding this effect.

3.6 Møller Polarimetry Optics

This section will review the Møller polarimetry optics solutions used for the PREX-II and CREX experiment as well as discuss the experimental choice to diagnostically tune the polarimeter to achieve an optimum analyzing power and the decision to use only a partial detector by turning off the high-voltage to select PMTs.

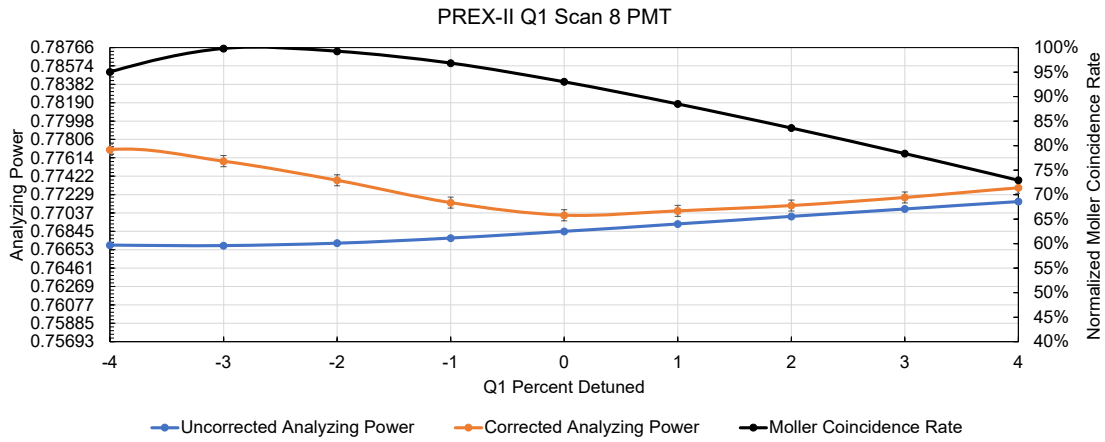


Figure 3.10: Disfavored 8PMT PREX-II Q1 asymmetry and rate scan. Vertical axis marks the detuning of the Q1 magnet in percent. Horizontal axis bars represent a 0.25% change off of the uncorrected analyzing power (blue line) at the point marked 0% detuning. It can be seen that corrected analyzing power (orange line) is not flat which is not optimal. The difference between the orange and blue lines is primarily due to the Levchuk effect.

3.6.1 PREX-II Optics

The original PREX-II Møller polarimeter optics plan utilized the entire 8 PMT detector configuration and the simulated asymmetry scan and rate scan of the first quadrupole setting can be seen in fig. 3.10 while activity on the detector face at the point of the asymmetry minimum can be seen in fig. 3.14. It was determined that we could aim for the region where the corrected asymmetry is at a minimum for polarimetry measurements. Multiple optics configurations were looked at in detail varying Q2 and Q4 magnet strengths and it was determined that an asymmetry minimum consistently occurred at an approximately 3% overtune from the quadrupole setting which coincided with the Møller coincidence rate maximum.

The diagnostic tuning process allowed us to avoid a substantial Levchuk correction but left the optics potentially sensitive to small changes in the quadrupole settings.

Shown in fig. 3.11 is scatter plot of Møller electron θ and ϕ acceptance under idealized conditions where the beam is a true point source, Levchuk effect and radiative corrections are turned off and transport interactions such as multiple scattering are disabled. Electrons

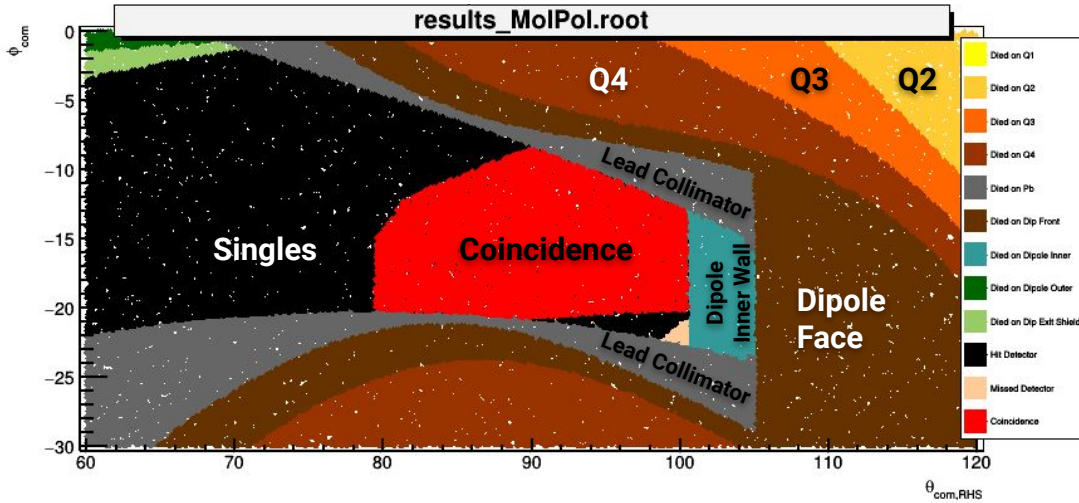


Figure 3.11: MolPol cemetery scatter plot sample image of PREX-II 8 PMT optics solution run with Geant4 performing transportation only without any scattering effects for the electron which traveled down the right arm of the polarimeter. Axes represent the θ_{COM} and ϕ_{COM} generated in the MolPol monte carlo. Scatter plot is colored by region in which Møller electron was last detected passing through a flux plane. Regions are marked in text on scatter plot for clarity.

which made it to the detector are marked in black if only one partner made it and red if the event resulted in a coincidence. Electrons which did not make it to the detector are marked by the region/surface in which they ended their transport. In fig. 3.12 the Levchuk effect in the MolPol generator has been turned on and it can be seen in that a significant number of electrons pass into the dipole and terminate on the outer wall (denoted by the small green markers). As per eq. (3.13) this serves to increase the average analyzing power. The goal is to avoid this problem and that's what the diagnostic tuning allowed us to do.

In fig. 3.13 over-tuning the Q1 magnet from the point of maximum rate by $\approx 3\%$ the polarimeter hits the minimum point of corrected asymmetry which is also the point where the Levchuk correction is most reduced. The remaining correction due to the Levchuk effect here is largely due to high-angle/lower-momentum electrons having been over-focused and hitting the dipole inner wall (the light blue markers).

The decision was made to diagnostically tube the polarimeter before each measurement through the following procedure.

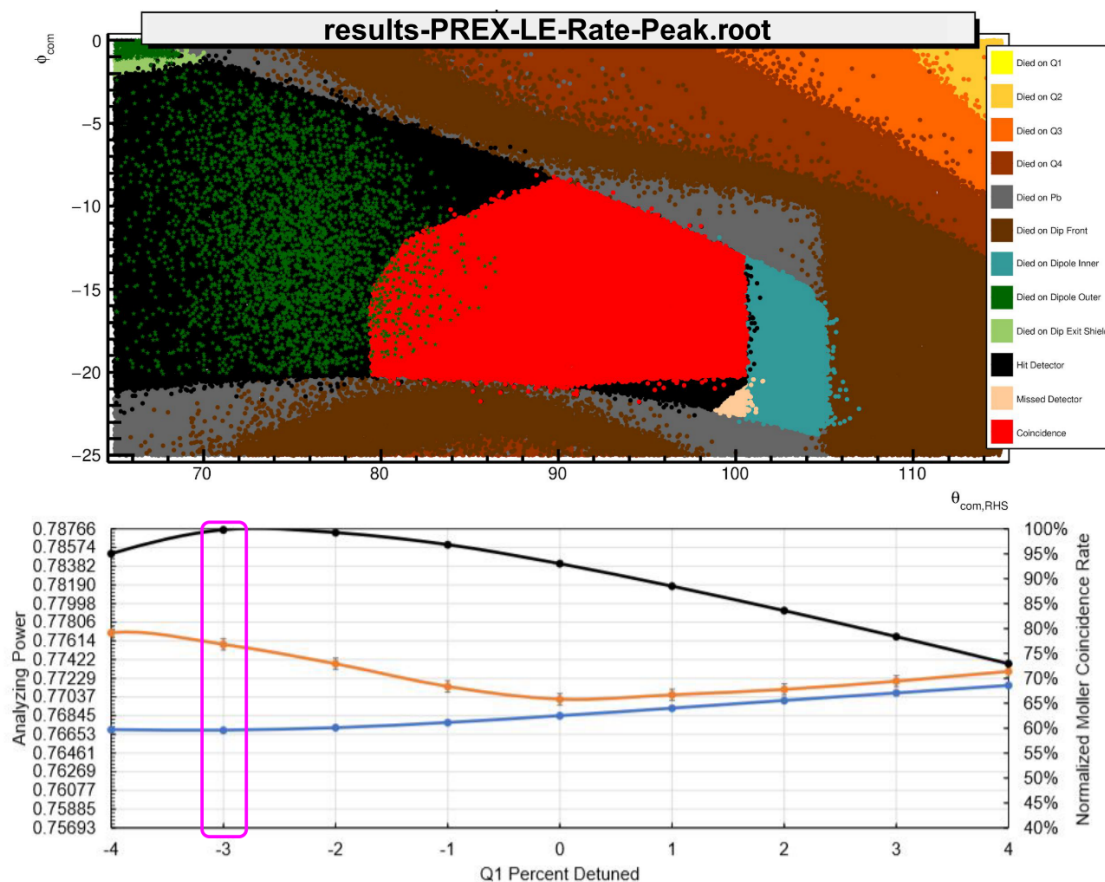


Figure 3.12: *Top panel:* MolPol cemetery scatter plot of PREX-II 8 PMT optics solution at rate maximum with the Levchuk effect turned in the Møller electron generator. Green scatter plot points are electrons which received a Levchuk angle modification large enough to cause them to collide with the outer wall of the dipole box. *Bottom panel:* Highlighted location on PREX-II 8 PMT optics asymmetry curve.

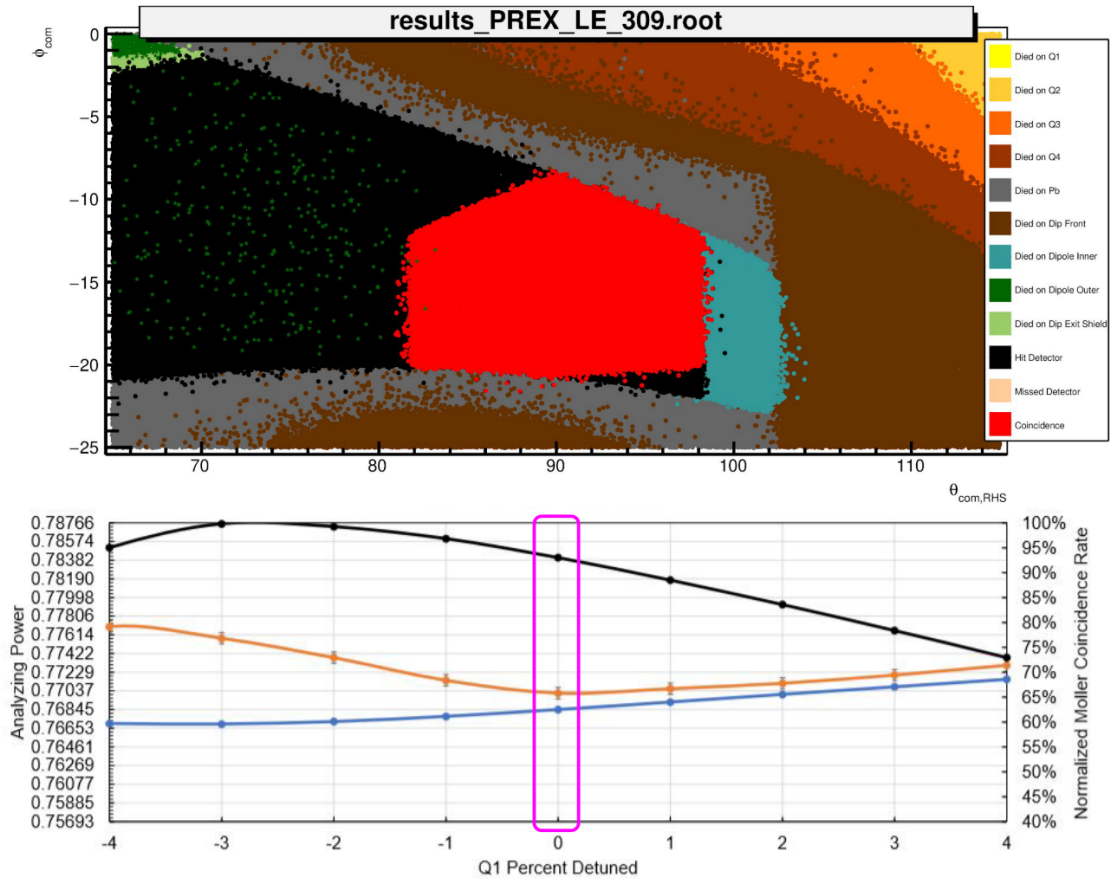


Figure 3.13: *Top panel:* MolPol cemetery scatter plot of PREX-II 8 PMT optics solution at a magnet setting $\approx 3\%$ over-tuned from rate maximum with the Levchuk effect turned in the Møller electron generator. Green scatter plot points are electrons which received a Levchuk angle modification large enough to cause them to collide with the outer wall of the dipole box. *Bottom panel:* Highlighted location on PREX-II 8 PMT optics asymmetry scan curve.

1. Cycle and set all magnets to nominal settings.
2. Perform dipole rate scan in incremental steps.
3. Cycle and set dipole to current which corresponds to maximum rate.
4. Perform Q1 rate scan in incremental steps.
5. Cycle and set Q1 to current which corresponds to maximum rate.
6. Polarimeter is now ready to take measurements.

This diagnostic tuning process was critical in discovering beam orbit inconsistencies during early measurements and gave some assurance to the reproducibility of settings and conditions. Small concerns emerged during the commissioning period.

- There was a large rate of singles hits due to inelastic scatters which resulted in higher than desired accidental rates.
- The region of effectively flat analyzing power was quite small and presented a challenge to achieving a high-precision measurement.

The process of trying to address these concerns led to the second critical insight/improvement on taking Møller measurements for the PREX-II and CREX experiments—utilizing a partial detector by turning off select PMTs. By utilizing the partial detector we can be sure that the angular distribution of Møllers which are successfully transported through the dipole will be larger than the maximum possible acceptance of the detector. When this is true, small changes to the angular distribution successfully transported through the dipole caused by changes in quadrupole optics become nearly irrelevant. A visual comparison of the physical size of the Møller coincidence acceptance between full and partial detectors utilizing the same quadrupole optics can be seen in a comparison of figs. 3.14 and 3.15.

This reduced PMT setup offered the following improvements.

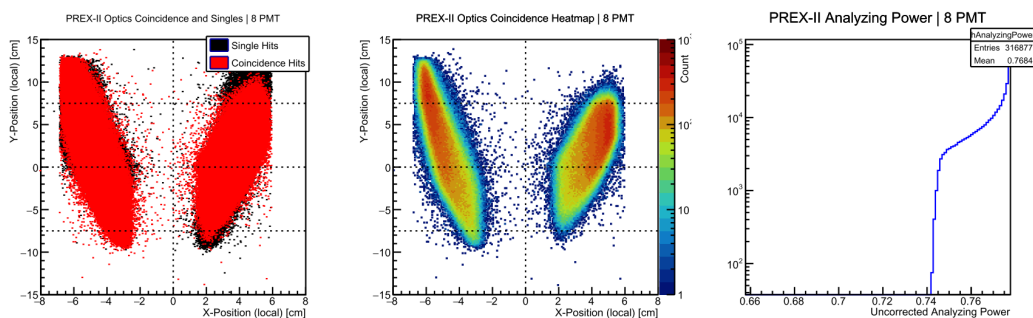


Figure 3.14: Disfavored PREX-II 8 PMT optics solution—Left panel: Coincidence and single hits overlay; Middle panel: Intensity of coincidence hits on detector; Right panel: Uncorrected analyzing power. The dashed lines on the left and center panels indicate individual PMT domains.

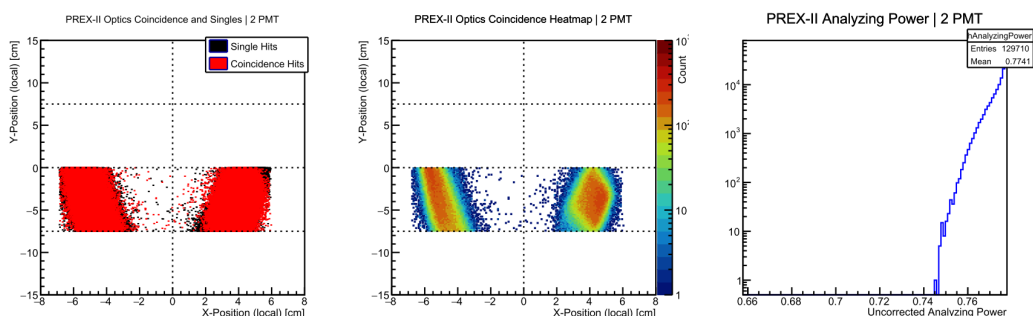


Figure 3.15: Favored PREX-II 2 PMT optics solution. *Left panel:* Coincidence and single hits overlay; *Center panel:* Intensity of coincidence hits on detector; *Right panel:* Uncorrected analyzing power. The dashed lines on the left and center panels indicate individual PMT domains.

- Provided larger margin of error in identifying the point of Møller coincidence rate maximum $\pm 2\%$.
- Greatly reduced sensitivity to Q2 and Q4 settings.
- Reduced detector hits from single Møllers with no matching partner.
- Reduced Mott background on the active PMTs since the increased dipole strength allowed for greater Mott/Møller separation.
- Constrained the analyzing power to a higher value closer to the maximum.
- Correction due to Levchuk effect can now be confidently eliminated by diagnostically tuning the Q1 magnet.

The marked improvements to reducing analyzing power sensitivity can be seen in fig. 3.16 giving an approximately $\pm 2\%$ region of analyzing power insensitivity. The center of this region occurs approximately 4% from the Møller rate peak. The dipole scan shown in fig. 3.17 has a well defined peak and a flat analyzing power to one side of the peak so care would have to be taken when choosing the rate maximum while tuning the magnet. Having the dipole magnet set stronger is more ideal than weaker; overall, there's an approximate $\pm 1.5\%$ region of analyzing power insensitivity.

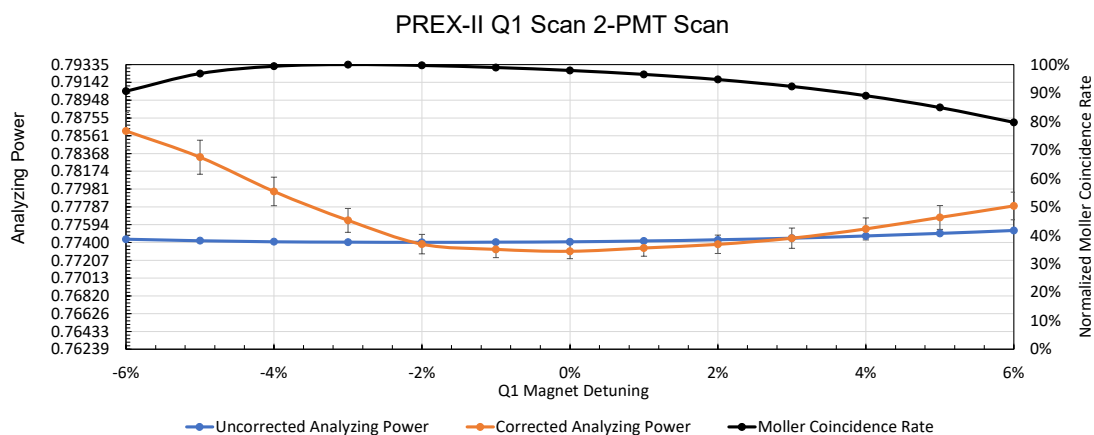


Figure 3.16: PREX-II Q1 asymmetry and rate scan utilizing only two of the photomultiplier tubes of the detector. Horizontal bars represent a 0.25% change off of the uncorrected analyzing power at 0% detuning. It can be seen that at our optimal tuning point the analyzing power is essentially flat and correction to the analyzing power is around -0.1%.

3.6.2 CREX Optics

The optics for CREX were approached through the same diagnostic tuning method along with again utilizing a partial detector by turning off select PMTs. Rates and analyzing powers for the quadrupole scan are shown for an 8 PMT and 6 PMT options in figs. 3.18 and 3.19. The 8 PMT option was avoided because the region of flat-ish analyzing power was narrow. The 6 PMT option offered a significant region of flat analyzing power $\pm 10\%$ leaving any concerns about the accuracy of the diagnostic tuning a non-issue. Reducing the number of PMTs used further would serve only to proportionally decrease the coincidence rate and increasing measurement time; thus, there was no incentive to use fewer PMTs. The nature of the acceptance cut imposed by the reduced PMTs can be seen in the center panel of fig. 3.20 where the detector defines the acceptance and this leaves a situation where excess Mollers miss the detector. The CREX dipole scan shown in fig. 3.21 offers a recognizable edge in the Møller coincident rate, a flat-ish rate peak and a region of approximately 4% of the magnet strength where we're insensitive to the dipole current setting. Identifying the rate peak as magnet current is decreased sufficient to tune the magnet; when choosing the peak err to the lower-current side.

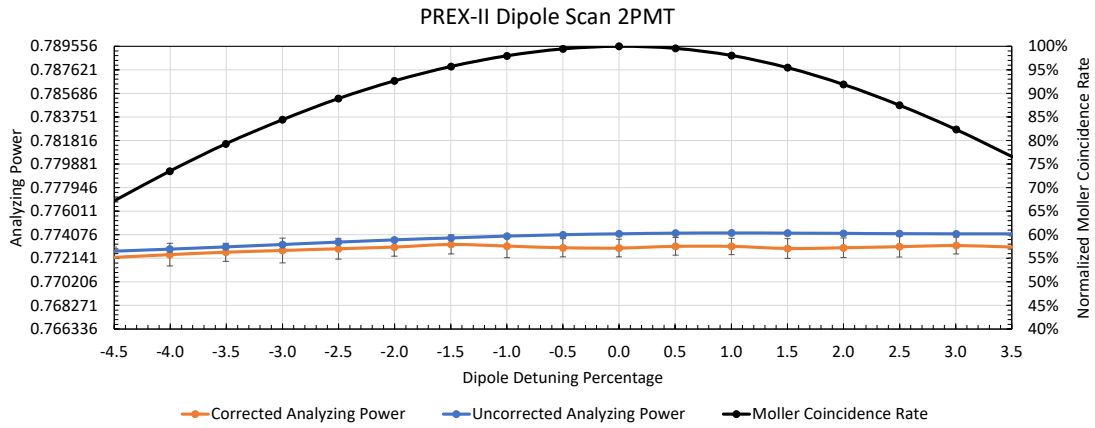


Figure 3.17: PREX-II dipole asymmetry and rate scan utilizing only two of the photomultiplier tubes. Horizontal bars represent a 0.25% change in analyzing power off of the uncorrected analyzing power at the 0% detuning position.

3.7 Optics Summary

A partial detector was used for both the PREX-II and CREX experiments. By allowing the detector to define the acceptance and ensuring that the acceptance was sufficiently smaller than the available Møller scatters which were successfully transported through the dipole we can minimize the impact of the Levchuk effect. A summary of the optics settings for the two experiments is given in table 3.1.

Table 3.1: Summary table of optics settings for the PREX-II and CREX experiments. Values given are for the pole tip field and are in units of Tesla. Both Q1 and Dipole settings are nominally recommended settings and are ultimately set by rate scan results.

Experiment	Q1	Q2	Q3	Q4	Dipole	Helmholtz
PREX-II	0.3	-0.06	0.0	0.06	0.157	4.0
CREX	0.28	0.05	0.0	0.10	0.337	4.0

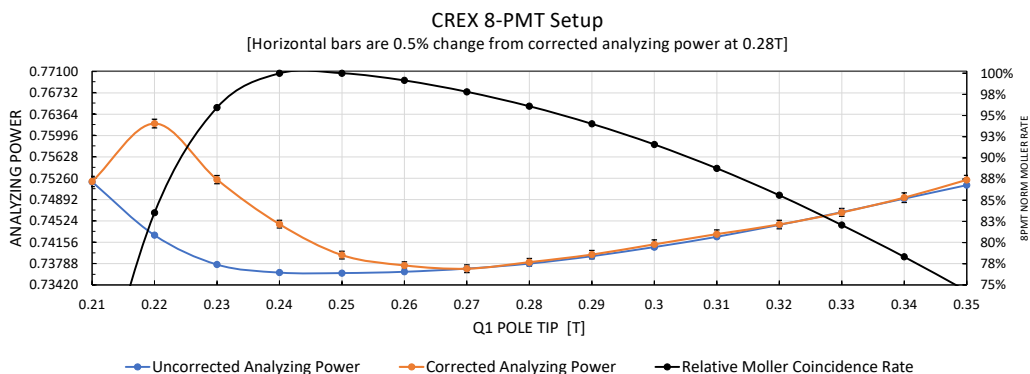


Figure 3.18: CREX optics utilizing all 8 PMTs of the Møller detector. Limited region of flat analyzing power made this a non-ideal solution.

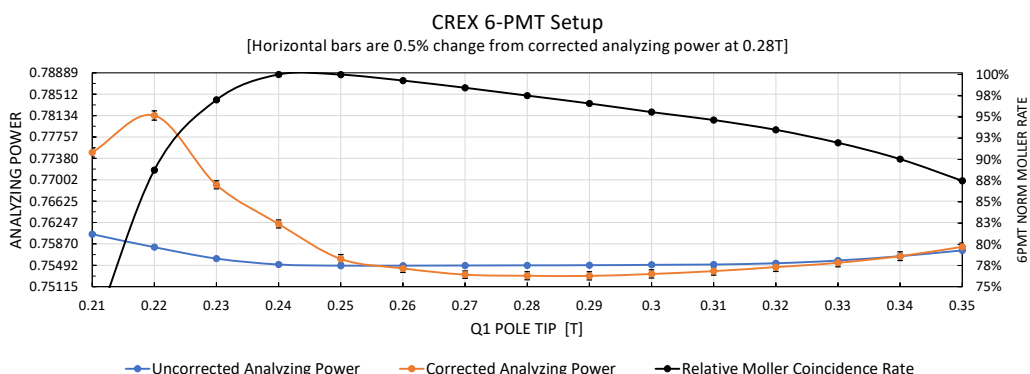


Figure 3.19: CREX optics utilizing only six PMTs if the Møller detector. Reduction of active detector area results in a large flat region of analyzing power with respect to quadrupole tuning making it an ideal optics solution.

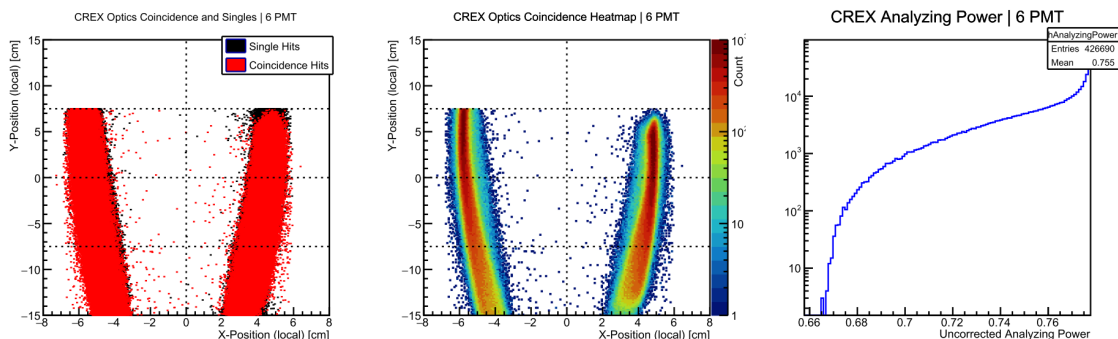


Figure 3.20: CREX 6PMT optics solution—Left panel: Coincidence and single hits overlay; Middle panel: Intensity of coincidence hits on detector; Right panel: Uncorrected analyzing power.

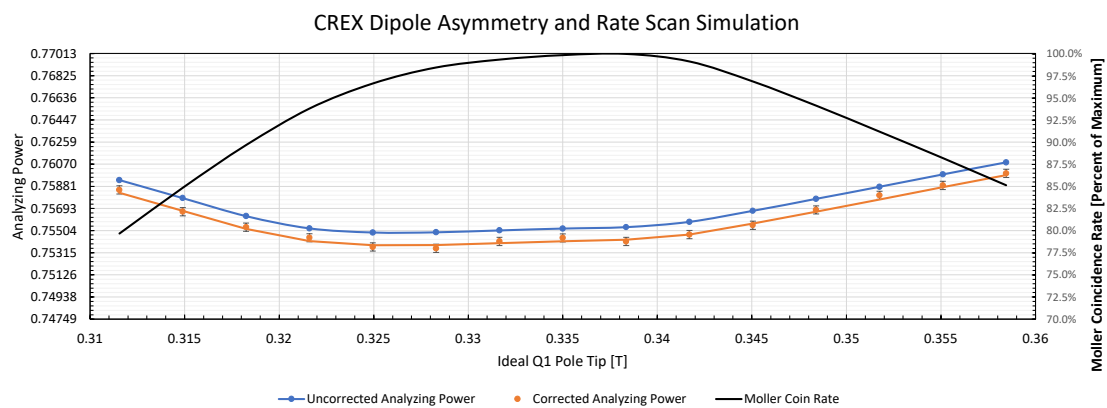


Figure 3.21: CREX dipole scan simulation results. Dipole has region of relatively flat rate that corresponds to region of flat analyzing power.

Chapter 4

Møller Polarimetry Results

This chapter will be a discussion of the Møller polarimetry data analysis since this was the author's primary assignment for analysis for the PREX-II and CREX experiments.

4.1 Møller Data Taking

PREX-II Data Taking

The PREX-II experiment ran from July through September of 2019. Møller polarimetry measurements were taken during that time on a regular weekly basis. Early Møller polarimetry shifts during July were unfortunately hindered by circumstances beyond the Hall control; any measurements made during July were minimal, had minimal setup check and were taken using the disfavored 8PMT optical setup for PREX-II. The first significant Møller polarimetry measurements begin on August 4, 2019 using the preferred 2PMT optics option and proceeded on a near-weekly basis until the close of the experiment.

CREX Data Taking

The data taking for the CREX experiment first briefly occurred on December 1, 2019 prior to the lab's holiday shutdown. When the experiment resumed in January 2020 regular polarimetry measurements were made with the Møller polarimeter. From mid-March 2020 through early-August 2020 was the COVID hiatus; measurements resumed for several

weeks in mid-August through September 2020. Since the Compton polarimeter was functioning well, the Møller polarimetry measurements were taken bi-weekly and will serve as a check on the Compton's measurements.

General Møller Data Taking Shift Procedure

Møller polarimetry shifts began with diagnostic tuning rate scan measurements for the dipole magnet and Q1. These setup run consisted of rate measurements so that we could identify rate peaks and drop-offs from which we could set the dipole and Q1 currents.

Møller polarimetry measurements taken in increments of 50K helicity cycles due to a memory limitation of older analysis software to which new analysis results would be compared. These which will be referred to as Møller runs, were made in both the HWP-IN and HWP-OUT states. Individual runs were limited to 50K helicity cycles; this is due to a memory limitation of older analysis software to which new analysis results would be compared. Runs were accumulated until the predetermined statistical uncertainty goal was reached for desired measurement; the sets of these individual Møller runs will be referred to as Møller Groups.

In addition to the polarization measurements there were also null/false asymmetry measurements made on the Cu foil. The purpose of these Cu foil measurements is to ensure that we aren't receiving false asymmetry signals from the Møller DAQ electronics.

4.2 Statistical Goals

The Møller polarimetry statistical error goals for individual measurements were 0.3% for PREX-II and 0.2% for CREX. One trade off for using the 2PMT configuration for PREX-II polarimetry measurements was that of lower rates for a more certain analyzing power; hence the lower statistical precision goal. The time required to reach these statistical goals [65] collecting coincidence data at rate r with a mean asymmetry $\langle A \rangle$ and

desired asymmetry error percentage $\epsilon = \delta A / \langle A \rangle$ is

$$t = \frac{1}{r \langle A \rangle \epsilon^2}. \quad (4.1)$$

Typical rates for PREX-II were approximately 11kHz and 25kHz for the 4 μm and 10 μm foils respectively and during CREX the typical rate was about 60kHz. With an approximate Møller coincidence asymmetry of 0.053 expected data collection times were 50 minutes per measurement during PREX-II when using the 4 μm foil and 25 minutes during CREX; these estimates compared well with times actually taken shown in figs. 4.1 and 4.2.

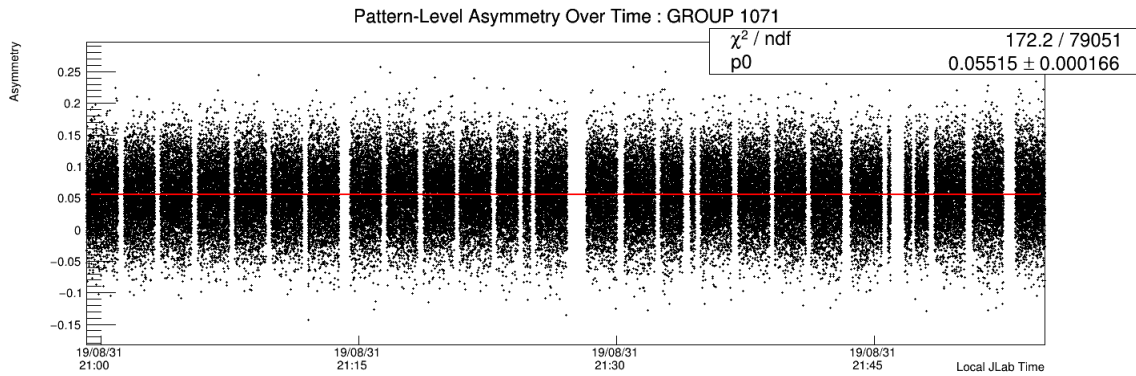


Figure 4.1: Asymmetry data of Group 1071 taken on 4 μm foil during the PREX-II experiment. Measurements including beam down time and small gaps in between individual runs (25 in total here at a helicity-flip frequency of 240 Hz) typically took on the order of 60 minutes.

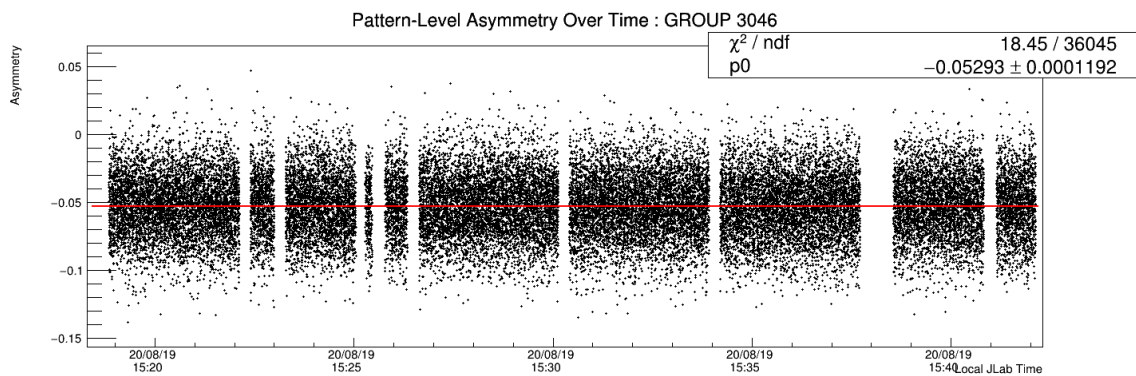


Figure 4.2: Asymmetry data of Group 3046 taken during the CREX experiment. Measurements including beam down time and small gaps in between individual runs (6 runs in total here at a helicity-flip frequency of 120 Hz) typically took on the order of 20 minutes.

4.3 MOLANA

MOLANA—Møller Analyzer—was the analysis software written by the author. This section will give a brief overview of the structure of the analysis chain which can be seen in fig. 4.3.

Software initialization

Software initialization and script execution is handled by a bash script. The author decided that for even casual Linux users this would perhaps be the easiest to understand. The initialization script takes input in the form of run number(s) to be analyzed and an alternate flag that indicates if the run to be analyzed was a bleed through run section 4.8.2. Analysis values such as dead time constant section 4.4.3, analyzing power section 3.5, charge pedestal section 4.4.2 and foil polarization are read from a small parameters data file as these don't require frequent input (although the values can be overridden when needed). The initialization script records the Møller settings file collected from JLab's EPICS system and into the database. Finally the initializer checks to see if the raw file has been previously decoded and then proceeds accordingly.

Møller Data Decoder

Raw data files from the Møller DAQ are converted to ROOT file formats. The decoded raw *data* file is then passed to **MOLANA Increments**.

MOLANA Increments

The scaler data in the converted raw data are sums over time; in order for this data to be useful data it is helpful to have all the scaler data converted into increments. The scaler data is also helicity-delayed against the ADC data. The analysis script calculates the scaler increments and corrects the data for the helicity delay. Values are stored in a new *increments* file and passed to **MOLANA Bleed** and **MOLANA Prompt**.

4.4 Møller Data Analysis

Throughout this section C will represent the recorded number of coincidence hits, A will represent accidentals, $R_{L/R}$ will be used to represent the left or right rates respectively, and Q will represent measured charge. Lower indices 1 and 0 will represent the sums of these quantities in alternating helicity states.

There are a handful of corrections that must be applied to this data in order to properly extract the Møller asymmetry. These includes a dead time correction, accidental correction, and charge normalization and charge pedestal subtraction; each of which will be briefly reviewed. The raw asymmetry of the data will be defined as:

$$A_{raw} = \frac{C_1 - C_0}{C_1 + C_0}. \quad (4.2)$$

and will be the basis for future cross-checking methods. Corrections to the raw asymmetry are applied as follows:

1. Coincidence rates must be accidental subtracted.
2. Coincidence and accidental rates must be charge normalized
3. Coincidence and accidental rates must be corrected for dead time losses.

4.4.1 Accidentals

Accidental coincidence hits (accidentals) are determined by utilizing a time delayed signal with either the left or the right side of the Møller detector. The time delayed coincidences are compared to the non-delayed coincidences and the difference of these two are the accidental coincidences. These accidental coincidences must be subtracted out of the coincidence hits.

$$A = \frac{(C_1 - A_1) - (C_0 - A_0)}{(C_1 - A_1) + (C_0 - A_0)}. \quad (4.3)$$

4.4.2 Charge Normalization and BCM Pedestal

There is a helicity correlated beam charge asymmetry which originates from differences in the circular polarization of the laser states mentioned in section 2.1.4. Coincidence and accidental counts recorded by the Møller DAQ must be charge normalized in order to make a proper asymmetry analysis. Additionally, the associated baseline measurement BCM electronics must be subtracted from the total charge recorded by the Møller DAQ.

$$\begin{aligned} C'_i &= \frac{C_i}{Q_i - P} \\ A'_i &= \frac{A_i}{Q_i - P}. \end{aligned} \tag{4.4}$$

This baseline is referred to as a pedestal and will be reference to as P and must be subtracted from the recorded charge for each recorded helicity cycle which we will reference as Q_i . This pedestal should also be measured prior to Møller polarimetry runs to determine its value. Substituting eq. (4.4) into eq. (4.3) gives the charge normalized asymmetry:

$$A = \frac{(C'_1 - A'_1) - (C'_0 - A'_0)}{(C'_1 - A'_1) + (C'_0 - A'_0)}. \tag{4.5}$$

Pedestal Measurements During PREX-II and CREX

Rather than take dedicated pedestal measurements during the Møller polarimetry measurements it was determined that the pedestal value could be calculated from data taken during beam trips—the Møller DAQ was running but for some reason the beam went momentarily off. This process was written into a secondary MOLANA analysis script that looked at Møller production runs to determine the value of the pedestal. A summary of the charge pedestal data for PREX-II can be seen in fig. 4.4 respectively. The data points in the PREX-II pedestal data which indicate a pedestal of 4 were taken while using the analog BCM while measurements made that show a pedestal of 2 were

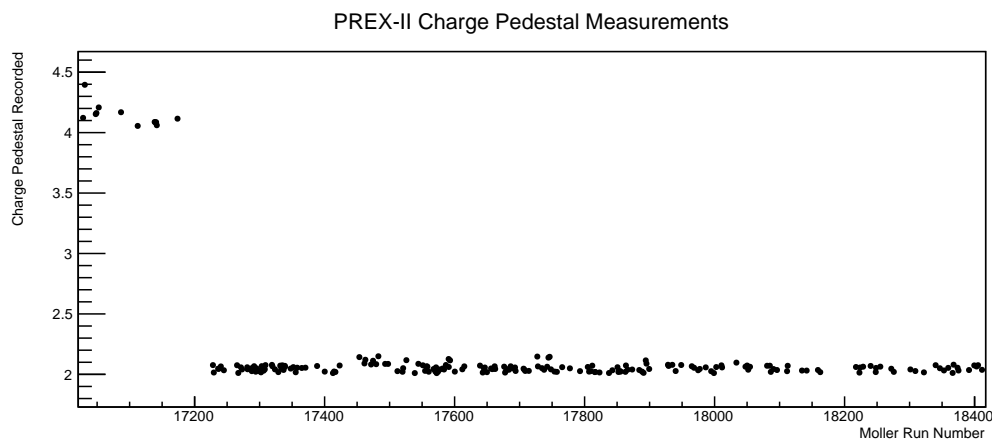


Figure 4.4: Pedestal data obtained during PREX-II Møller polarimetry measurements.

taken while using the digital BCM. The decision to use a charge pedestal value of 2 for

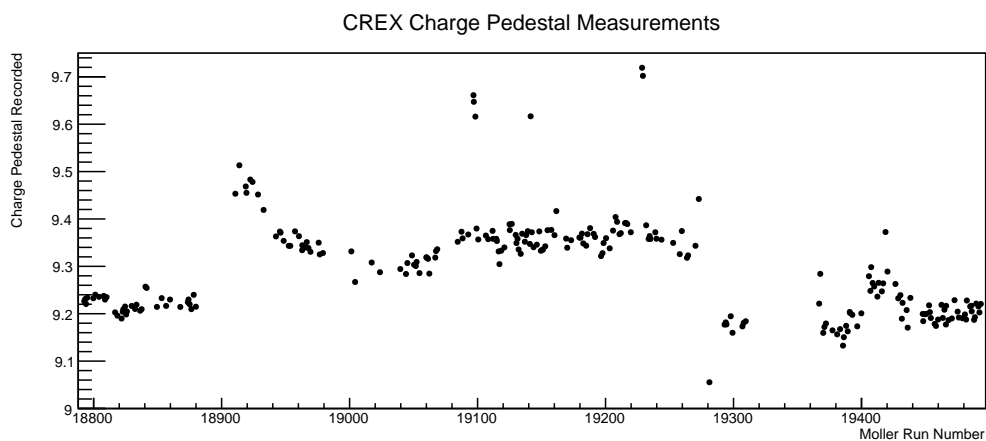


Figure 4.5: Pedestal data obtained during CREX Møller polarimetry measurements.

Møller measurements taken during PREX-II was made.

Pedestal measurements during CREX can be seen in fig. 4.5. Changes in the pedestal can be observed after returning from the 2019-2020 holiday shutdown at about run 18000 and after the COVID shutdown around run 19300. Pedestals of 9.25 and 9.35 were applied for Møller asymmetry calculations for CREX although in hindsight this small change which amounted to nothing more than a few hundredths of a percent change in calculation.

4.4.3 Dead Time

For any given rate of independent events E we can safely assume that the distribution of the time between those events is Poisson distributed. The expected probability that N events occur during the first time unit t is given by the probability mass function (PMF):

$$P[E = N] = \frac{\lambda^N e^{-\lambda}}{N!} \quad (4.6)$$

From this expression we can then calculate the probability that zero events occur in the first unit of time—denoted in the Poisson distribution formalism using λ as an abstract parameter for an event occurrence frequency $1/t_0$.

$$P[E = 0] = \frac{\lambda^0 e^{-\lambda}}{0!} = e^{-\lambda} \quad (4.7)$$

From eq. (4.7) we have the probability of there existing no recorded events during the first tick of electronic time. The amount of time in which the electronics have recorded no events and the computer is waiting for an event to occur is known as the *live time*. The probability that a stretch of live time continues decreases as each discrete unit of time—abstractly expressed by λ in this Poisson expression—passes. We can calculate the evolving probability of live time as discrete units of time continue to pass by extending eq. (4.7).

$$\begin{aligned} P[E = 0] * P[E = 0] * P[E = 0] \dots &= e^{-\lambda} * e^{-\lambda} * e^{-\lambda} \dots = e^{-\lambda t} \\ P[t > t_0] &= e^{-\lambda t} \end{aligned} \quad (4.8)$$

If eq. (4.8) is the probability of all passed time being free of electronic dead time then the probability of electronic dead time must necessarily be:

$$P[t_0 \leq t] = 1 - P[t > t_0] = 1 - e^{-\lambda t} \quad (4.9)$$

For a detector, dead time occurs as electronics become increasingly overwhelmed by particle detection rates. The detector has a limiting rate R^{limit} before it begins to miss data for which a time window available for a single particle detection τ can be defined as $\tau = 1/R^{limit}$. We can replace the value λt in eq. (4.9) with τR in where R is the rate which the detector hardware reports for particle detection. τ will be referred to as the *dead time constant* throughout the remainder of this document. We can now express the probability for dead time in relation to the detector rates by modifying eq. (4.9) to:

$$P[R \leq R^{limit}] = 1 - P[R > R^{limit}] = 1 - e^{-R\tau} \quad (4.10)$$

We can extend this to our integrated Møller detector rates where R^{meas} is the integrated rate of Møller detection, R^{phys} is the actual physical rate and R is the rate of particle detections and presuming the quantity $R\tau$ is small.

$$\begin{aligned} R^{meas} &= R^{phys} (1 - (1 - e^{-R\tau})) \\ &= R^{phys} e^{-R\tau} \\ &\approx R^{phys} (1 - R\tau) \end{aligned} \quad (4.11)$$

Determining the Dead Time Constant

The Jefferson Lab Hall A Møller Polarimeter is outfitted with an LED pulse generator. The pulser is turned on during a data collection mode similar to a standard asymmetry measurement. However, instead of looking for a coincidence between Møller electrons which hit the left side and right sides of the detector, this mode looks for a triple coincidence—left Møller, right Møller and LED flash. In this way, we can measure exactly how many LED flashes, which occur at a known rate, are lost as detector rates increase. A series of measurements while varying the beam current, which affects the scattering rates, will allow us to determine dead time losses. For the dead time analysis the original PAW scripts for the Hall-A Møller Polarimeter were used.

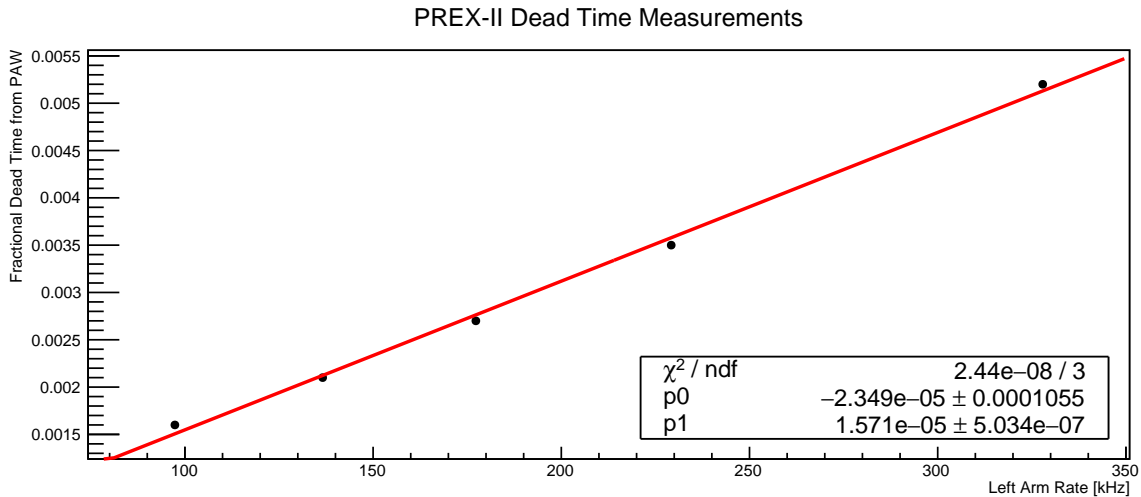
Table 4.1: Summary of dead time rate measurement runs taken during PREX-II.

Møller Run	Left Rate [kHz]	Dead Time [%]
17980	97.3	0.16
17981	136.6	0.21
17982	177.3	0.27
17984	229.2	0.35
17985	327.9	0.52

The output from the PAW analysis can be seen in table 4.1. We can extract the relationship between dead time losses and rates from the collected data through eq. (4.11) and obtain

$$\text{Losses} = \frac{R^{phys} - R^{meas}}{R^{phys}} = R\tau \quad (4.12)$$

The plot can be seen in fig. 4.6 where fractional dead time losses are on the vertical axis and left-sided Møller singles rates can be seen on the horizontal axis. The data has been fitted in ROOT and returns a slope of 1.57×10^{-5} ; this is our dead time constant τ .

**Figure 4.6:** Deadtime measurements during the PREX-II experiment used to determine the dead time constant of the detector package.

The Møller data must finally be corrected (both coincidence and accidentals) for the dead time by modifying eq. (4.5) as prescribed in eq. (4.12). The final pattern by pattern

computation of the asymmetry is as follows:

$$A_{comp} = \frac{(C'_1 - A'_1)e^{R_1\tau} - (C'_0 - A'_0)e^{R_0\tau}}{(C'_1 - A'_1)e^{R_1\tau} + (C'_0 - A'_0)e^{R_0\tau}}. \quad (4.13)$$

4.4.4 Data Cuts

This section will consist of a brief review of the various data cuts made to the data in order to maintain data quality. When data is flagged for a cut

Beam Trips

It is inevitable that during measurements beam trips will be experienced. Beam trips in the data stream were defined as moments where the BCM value recorded by the DAQ was less than predetermined threshold. Any time a beam trip was noticed in the data, the three helicity patterns preceding the trip were excluded from analysis and the three helicity after the return of the beam were excluded from data analysis. The data exclusions were made to alleviate possible concerns over data quality.

Mismatch between PLUs

Møller data is recorded by two different hardware units into the DAQ; the data recorded by each PLU therefore serves as a check on the integrity of the overall data. The data from each these units is compared during analysis. If the recorded integrated counts of coincidence or accidentals differ by more than 1 then the helicity cycle is discarded.

Incorrect Helicity Pattern

Occasionally the Møller DAQ may record the wrong state of a helicity cycle which results in a bad pattern and hence would result in a bad calculation. So this data must be removed. There are two steps to checking for proper patterns. At the beginning of every helicity pattern the DAQ records a pattern sync signal; this signal marks the beginning of the helicity pattern. The pattern sync channel data must consist of a single 1 (denoting

the signal) followed by several 0s (either three for quartets or seven for octets). A deviation from this pattern will exclude the pattern and its neighbors from calculation.

Second, there's the validation of the helicity pattern itself. Helicity quartet patterns come in $[0,1,1,0]$ or its flipped version $[1,0,0,1]$. Helicity octet patterns come in $[0,1,1,0,1,0,0,1]$ or its likewise flipped version. Each pattern is analyzed according to the following prescription.

- Let each helicity pattern of length N be represented by an cycle array $C = [C_1, \dots, C_N]$.
- For each helicity pattern C create an array of pair sums S such that $S_i = C_i + C_{i+1}$; the size of S will be $N - 1$.
- Modify S such that $S_i = S_i \bmod 2$.
 - For quartets S must explicitly be $[1, 0, 1]$.
 - For octets S must explicitly be $[1, 0, 1, 1, 1, 0, 1]$.

Any deviation from this prescription indicates that there has been either an error in recording the helicity cycle state or data was electronically lost.

4.5 Validating Møller Analysis Corrections

Since the Møller polarimetry analysis code used for PREX-II and CREX was newly written any corrections to the data were checked against their analytic expectations. This section will be a review of the three corrections to the Møller analysis: the dead time correction; the charge normalization; and the accidental subtractions. Analytic expressions for the size of the corrections will be derived in terms of measurable quantities. Each computational correction will be isolated and a percent correction will be taken against the raw asymmetry. A successful implementation in the code of the corrections should yield a one-to-one correlation between its computationally derived value and its analytically

expected value. In all of the following A_{raw} will refer to the uncorrected Møller coincidence asymmetry $\frac{C_1 - C_0}{C_1 + C_0}$ and the analytic expressions for the size of the correction will be given in the form of $\frac{A_{corr} - A_{raw}}{A_{raw}}$ to eliminate the need for sign-corrections.

4.5.1 Dead Time Correction Analytic Expectation

The MOLANA analysis code automatically calculated the dead time correction during prompt analysis. In order to ascertain whether the correction was being computationally applied correctly we need to calculate the analytic expectation. First, the following two relationship will be handy: It will also be handy to define the following relationships,

$$\begin{aligned} C_1 &= \bar{C}(1 + A_{raw}) \\ C_0 &= \bar{C}(1 - A_{raw}) \end{aligned} \tag{4.14}$$

We start off with the raw uncorrected Møller asymmetry that was defined in eq. (4.2) and we will correct for dead time losses as prescribed in eq. (4.11). The dead time corrected Møller asymmetry can be written as:

$$A_{corr}^{DT} = \frac{(1 + R\tau) C_1 - (1 + R\tau) C_2}{(1 + R\tau) C_1 + (1 + R\tau) C_2}. \tag{4.15}$$

It is evident that if the total detector rate R for each helicity state is equal then no deadtime-correction would be required as $A_{corr}^{DT} = A_{raw}$. However, because there exists a charge asymmetry between the two helicity states there exists base-rate differences between the two helicity states. Similar to eq. (4.14) the relationship between detector rates R_1 and R_0 can be expressed as a function of the helicity-averaged rate \bar{R} and rate asymmetry A_R .

$$\begin{aligned} R_1 &= \bar{R}(1 + A_R) \\ R_0 &= \bar{R}(1 - A_R) \end{aligned} \tag{4.16}$$

Expanding eq. (4.15) with the helicity correlated rate asymmetry yields the following

$$A_{corr}^{DT} = \frac{(1 + R_1\tau) C_1 - (1 + R_0\tau) C_0}{(1 + R_1\tau) C_1 + (1 + R_0\tau) C_0} \quad (4.17)$$

which we can simplify by expanding and collecting like terms and back-substituting A_{raw} into the result

$$A_{corr}^{DT} = A_{raw} \frac{[1 + ((\bar{R}\tau) + (\bar{R}\tau)A_R A_{raw}^{-1})]}{[1 + ((\bar{R}\tau) + (\bar{R}\tau)A_R A_{raw})]} \quad (4.18)$$

The $A_R A_{coin}$ term in the denominator can most likely be ignored in all cases as $A_R A_{raw}$ will be on the order of 10^{-3} and $R\tau$'s value is also of the order 10^{-3} (at a left-singles rate of 250kHz which is a high estimate). Cancellation of the the aforementioned term and some rearrangement yields that the size of the expected correction compared to the raw Møller asymmetry is:

$$\frac{A_{corr}^{DT} - A_{raw}}{A_{raw}} = \bar{R}\tau \frac{A_R}{A_{raw}}. \quad (4.19)$$

Since τ is a constant value and A_R should be of the same order as A_{raw} , controlling detector rates is paramount to minimizing the dead time corrections and hence associated systematic uncertainty.

Deadtime Calculated v. Analytic Expectation

For each Møller polarimetry run taken during PREX-II and CREX a raw/uncorrected asymmetry A_{raw} was stored in the database, a dead time only corrected asymmetry value was stored in the database A_{corr}^{DT} , and the average left and right arm detector rates \bar{L} and \bar{R} and the helicity-correlated asymmetries of those detector arm rates A_R and A_L were stored in the database. In a validation analysis data from each Møller polarimetry run stored in the database was used to calculate the quantities in eq. (4.19). Results of this comparison can be seen in fig. 4.7 for both the PREX-II and CREX experiments.

The calculations explicit to dead time corrections made in the newly written analysis code return the expected results. The first-order polynomial fit returns values which are consistent with a one-to-one comparison with slopes of 0.999 ± 0.002 for the PREX-II dead time corrections and 1.003 ± 0.005 for CREX.

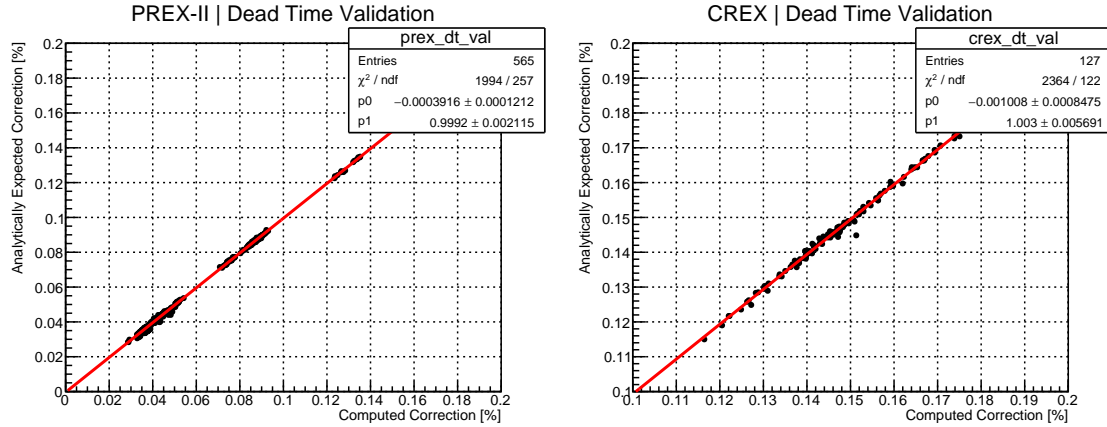


Figure 4.7: Comparison of computed dead time correction vs. analytic expectation for the dead time correction PREX-II and CREX. Each point represents the correction made to an individual Møller data run.

4.5.2 Charge Normalization and Pedestal Subtraction

The Møller data must also be corrected for charge asymmetry and pedestal correction. To achieve this the number of events during each helicity cycle is normalized to total charge measurement of that cycle and the charge pedestal must be subtracted from each cycle. The relationship between charge measurements Q_1 and Q_2 related to average charge measurement \bar{Q} and charge asymmetry A_Q is similar to that seen in eq. (4.16)

$$\begin{aligned} Q_0 &= \bar{Q}(1 + A_Q) \\ Q_1 &= \bar{Q}(1 - A_Q) \end{aligned} \tag{4.20}$$

And we will define the pedestal-corrected charge terms

$$\begin{aligned} Q'_0 &= \bar{Q}(1 \pm A_Q) - P \\ Q'_1 &= \bar{Q}(1 \pm A_Q) - P \end{aligned} \tag{4.21}$$

Again, starting with eq. (4.2) and then normalizing each state by the respective charge measurement we derive a term for the charge-corrected Møller asymmetry A_{Qcorr}

$$A_{corr}^Q = \frac{\frac{C_1}{Q_1} - \frac{C_0}{Q_0}}{\frac{C_1}{Q_1} - \frac{C_0}{Q_0}} \quad (4.22)$$

Proceeding with a substitution for the asymmetric charge states defined in eq. (4.20) and expanding, binomial approximation (requiring A_Q be small) and rearranging we arrive at a charge but not pedestal corrected:

$$A_{corr}^Q = A_{raw} \left(\frac{1 - A_Q A_{raw}^{-1}}{1 - A_Q A_{raw}} \right) \quad (4.23)$$

The charge asymmetry term A_Q can now be manipulated to account for the pedestal correction. To do so we derive a pedestal-corrected charge asymmetry A_Q^{Pcorr} from eq. (4.21)

$$A_Q^{Pcorr} = \frac{Q'_1 - Q'_2}{Q'_1 + Q'_2} \quad (4.24)$$

$$\approx A_Q \left(1 + \frac{P}{Q} \right).$$

Replacing A_Q in eq. (4.23) with A_Q^{Pcorr} we get the pedestal- and charge-corrected expression for the size of the correction in terms of our measured quantities A_Q , P , \bar{Q} and A_{raw}

$$A_{QPcorr} = A_{raw} \left(\frac{1 - A_Q \left(1 + \frac{P}{\bar{Q}} \right) A_{raw}^{-1}}{1 - A_Q \left(1 + \frac{P}{\bar{Q}} \right) A_{raw}} \right). \quad (4.25)$$

So long as the product $A_Q A_{raw}$ is sufficiently small the approximate charge- and pedestal-corrected asymmetry seen in eq. (4.25) can be manipulated into

$$\frac{A_{QPcorr} - A_{raw}}{A_{raw}} \approx -A_Q \left(1 + \frac{P}{\bar{Q}} \right) A_{raw}^{-1}. \quad (4.26)$$

Charge Corrections Validation

Charge and pedestal corrections for Møller data runs taken during PREX-II and CREX can be seen in fig. 4.8 plotted against the analytic expectations; the slope of the PREX-II data fit is -0.9969 ± 0.0003 and the slope of the CREX data is -0.9971 ± 0.002 . The analytically expected and computed corrections are consistent with expectations indicating the the implementation of the charge/pedestal correction in the new analysis code is correct.

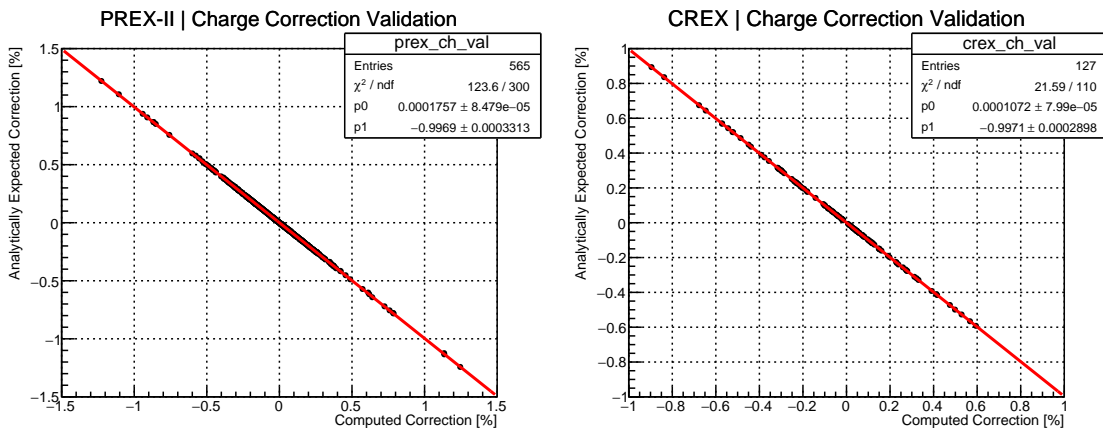


Figure 4.8: Comparison of computed correction vs. analytic expectation for PREX-II and CREX charge asymmetry and pedestal corrections. Each point represents a single Møller polarimetry data run. The fit shown is for a first order polynomial as we should see a one-to-one relationship between the quantities.

4.5.3 Accidental Correction

Møller data must also be corrected for accidentals. Let A_1 and A_0 be the recorded accidental rates in each helicity cycle, \bar{A} be the average accidental rate during the measurement and A_A be the asymmetry of the accidentals. Similar to before, the following relationships exist,

$$\begin{aligned}
 A_1 &= \bar{A}(1 + A_A) \\
 A_0 &= \bar{A}(1 - A_A).
 \end{aligned}
 \tag{4.27}$$

The process for accidental correction is rather simple; for each helicity cycle recorded accidental rates must be subtracted from the coincidence rates. To derive the analytic expectation for the size of this correction to the raw measured asymmetry we again will start with the Møller asymmetry eq. (4.2) and correct the measured coincidence rates.

$$A_{corr}^A = \frac{(C_1 - A_1) - (C_0 - A_0)}{(C_1 - A_1) + (C_0 - A_0)} \quad (4.28)$$

Using the relationships found in eqs. (4.14) and (4.27) the accidental corrected asymmetry can be further simplified to

$$A_{corr}^A = A_{raw} \left[\frac{1 - \frac{\bar{A}A_A}{CA_{raw}}}{\frac{1-\bar{A}}{C}} \right] \quad (4.29)$$

Let fractional average accidental rate to average coincidence rate be noted as $f_A = \frac{\bar{A}}{C}$ and assuming that f_A is sufficiently small the accidental corrected coincidence asymmetry can be approximated as

$$A_{corr}^A \approx A_{raw} [1 + f_A - f_A A_A A_{raw}^{-1} - f_A^2] \quad (4.30)$$

from which we can get an analytic expectation value for the size of the correction to the raw coincidence rates when we subtract out the accidentals.

$$\frac{A_{corr}^A - A_{raw}}{A_{raw}} \approx f_A [1 - A_A A_{raw}^{-1}] \quad (4.31)$$

From eq. (4.31) it can be seen that minimization of the accidentals rate is desirable in order to keep the size of the correction down and associated systematic uncertainty on that correction. The accidental asymmetry plays a lesser role in the size of the correction. Between PREX-II data taking and CREX the value of the accidental asymmetry changed, presumably due to changes in acceptance of Mott scatters.

Accidental Correction Validation

The results of the computed accidental correction versus the analytical calculation can be seen in fig. 4.9. The first-order polynomial fit results are consistent with a one-to-one relationship returning a slope of 0.9985 ± 0.0018 for the PREX-II data and a slope of 0.9958 ± 0.0052 for the CREX data indicating that the corrections were implemented correctly.

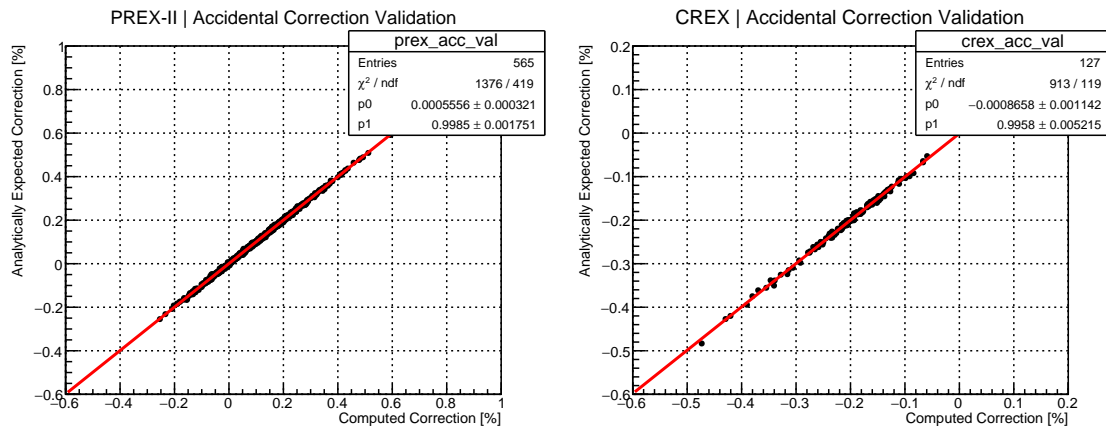


Figure 4.9: Comparison of computed correction vs. analytic expectation for PREX-II and CREX accidental corrections. Each point represents a single Møller polarimetry data run. The fit shown is for a first order polynomial as we should see a one-to-one relationship between the quantities. The analytically expected and computed corrections are consistent indicating the the implementation of the accidental correction in the new analysis code is correct.

4.6 Spin Dances

Special polarization measurements were taken at the beginning of the PREX-II and CREX experiments. As described in section 2.1.4, a Wien filter is used to induce a precession in the electron beam prior to the electrons being passed into the accelerator. While these devices can be used for a slow flip of the helicity states it is also used to calibrate the polarization of the electron beam in the experimental hall. Beam electrons precess as their trajectories are bent in the two recirculating arcs of the accelerator and the bend into the experimental halls; the Wien filter can be used to compensate for this precession to maximize the longitudinal polarization of beam.

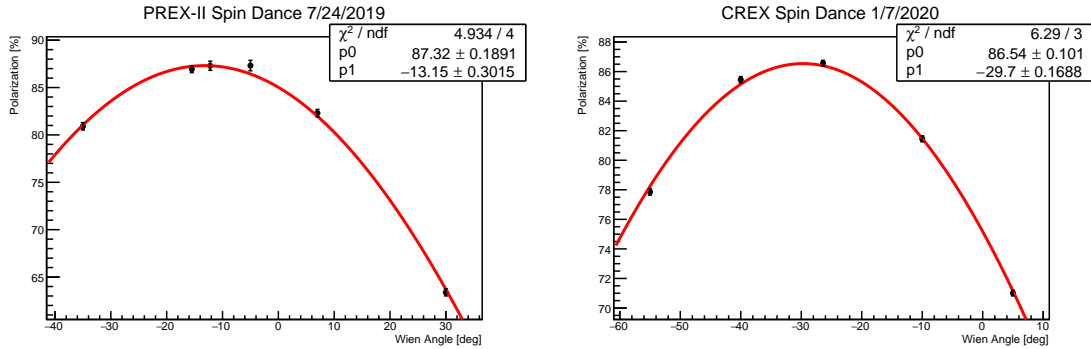


Figure 4.10: Graphical summary of PREX-II and CREX spin dance measurements taken. Polarization values with statistical errors (calculated from the analysis software written by the author) are fit to a cosine curve in ROOT $f(\theta) = x_1 \cos(\theta - x_2)$.

Polarization is measured while the accelerator deliberately alters the Wien angle setting; the polarization data is then fit to a curve in order to determine the Wien angle where maximum polarization occurs. The spin dance polarimetry measurements are used as calibration/systematics check on the Wien angle which was predicted/calculated as being optimal. Results of the spin dance measurements are shown in fig. 4.10 and horizontal Wien filter set points are shown in table 4.2.

Table 4.2: Wien settings for PREX-II and CREX prior to and after spin dance Møller polarimetry measurements.

Experiment	Predicted Wien Angle	Optimized Wien Angle
PREX-II	-15.5°	-13.0°
CREX	-26.4°	-29.64°

4.7 Møller Polarimetry Results

This section will be a review of the results of the Møller polarimetry measurements taken during PREX-II and CREX along with discussion. Final beam polarizations that were used for PREX-II results will be shown and results from polarization measurements during CREX will be shown against Compton polarimeter measurements.

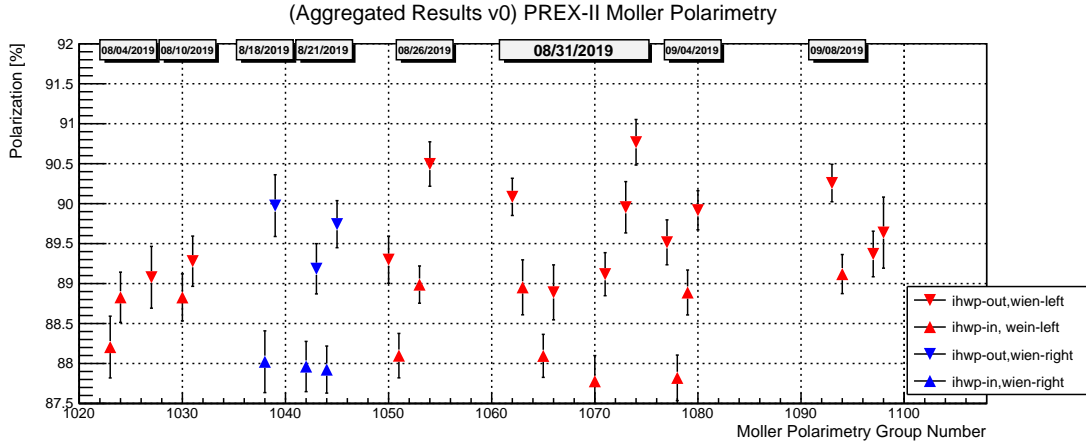


Figure 4.11: All taken PREX-II Møller polarimetry measurements organized by Møller polarimetry Group number.

4.7.1 PREX-II

A summary of all polarization measurements taken during PREX-II can be seen in fig. 4.11. The measurements are separated by HWP-In and HWP-Out states along with Flip-Left and Flip-Right Wein filter states. During analysis of polarization runs, systematics checks and subsequent foil checking it was determined that there existed two issues that needed to be addressed during analysis. First, was the presence of a large difference between the HWP-In and HWP-Out helicity states. Second, inconsistencies in data taken on the $4\mu\text{m}$ foil when the beam position was changed. Both of these issues will be addressed in separate sections to follow.

Half-wave Plate State Difference

The half-wave plate polarization difference was first identified on 8/18/19 when HWP-IN and HWP-OUT polarization measurements—Møller group 1038 and 1039 measurements—yielded an approximately 5σ difference suggesting an inconsistency in polarization between the two half-wave plate states. The difference in measurements can be seen in the data for both the $4\mu\text{m}$ and $10\mu\text{m}$ iron foils polarization measurements which are summarized in figs. 4.14 and 4.15 respectively. Data from the Compton polarimeter was analyzed as a check against the Møller polarimetry measurements and analysis to rule out

any potential failures in the Møller analysis. Data taken by the Compton polarimeter is shown in fig. 4.12 and suggests the existence of the polarization difference between half-wave plate states but with a $\approx 2.5\sigma$ difference was not definitive. The accelerator was asked to take polarimetry measurements with high statistical precision with the Mott polarimeter as prior measurements made by the Mott polarimeter suggested a potential difference but were statistically ambiguous. The high-statistics data subsequently taken by the Mott polarimeter is shown in fig. 4.13 demonstrated the existence of the polarization difference to a high degree of statistical precision and was independently analyzed twice [66, 67]. Confirmation by the Compton and Mott polarimeters ruled out the possibility of the HWP measurement differences being a Møller-specific issue.

It was determined that this issue was due to an unaccounted-for birefringence in the vacuum window of the Hall-A laser. Because of this HWP state difference polarizations for the HWP-In and HWP-Out states were calculated and provided to the experiment separately.

4 μ m Fe Foil Irregularity

The second issue was related to an apparent physical imperfection in the 4 μ m foil; this issue was discovered when running systematic tests on the 4 μ m foil while jogging it off-center by ± 2 mm. Results from those systematics checks demonstrated that polarization measurements taken off-center on the 4 μ m foil were 1% higher than those taken at the center. The 10 μ m foil was used in polarization measurements and also systematically tested for deviations by jogging the foil ± 2 mm off center. The results of these measurements and systematic studies can be seen in fig. 4.16, with a tabled summary given in section A.5. After the discovery of the 4 μ m foil discrepancy all subsequent Møller polarimetry measurements were taken on both the 4 μ m and the 10 μ m foils. A summary of these results which demonstrates the consistent difference between measurements on the two foils (when at center) can be seen in figs. 4.17 and 4.18 in both HWP states.

In order to deal with these differences the decision was made to take the 10 μ m-to-4 μ m

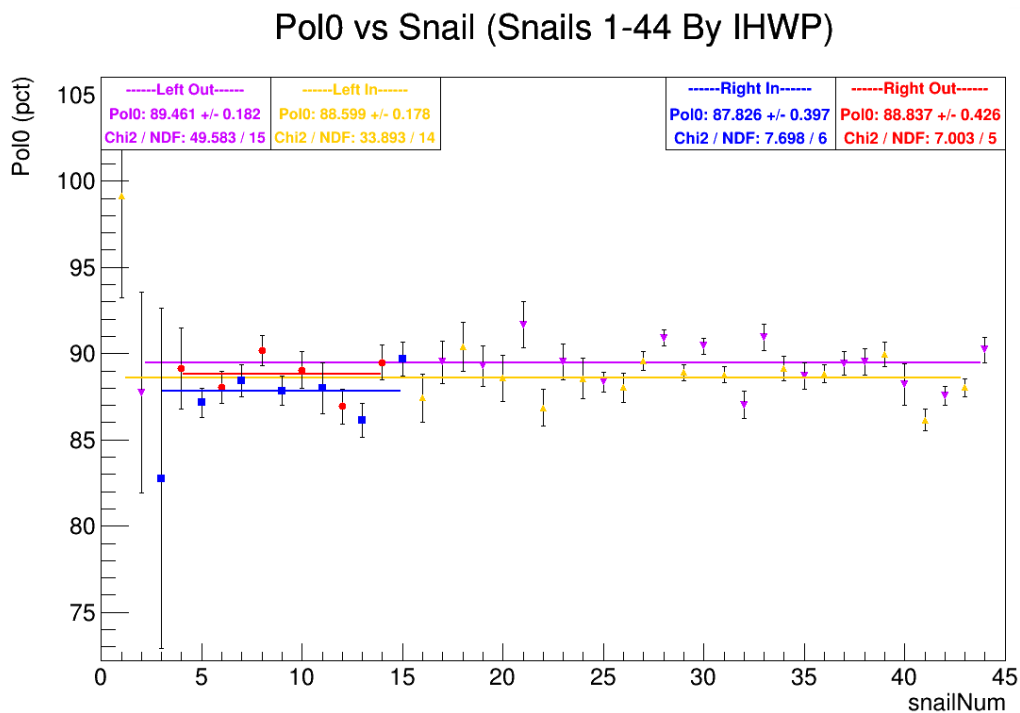


Figure 4.12: Compton polarimetry measurements separated by iHWP state and Wien flip state. For the purpose of comparing polarimetry measurements the Compton polarimeter results suggested that the HWP-IN/HWP-OUT difference seen by the Møller polarimeter was real with a statistical significance of $\approx 2.5\sigma$. [Compton data plot courtesy of Allison Zec.]

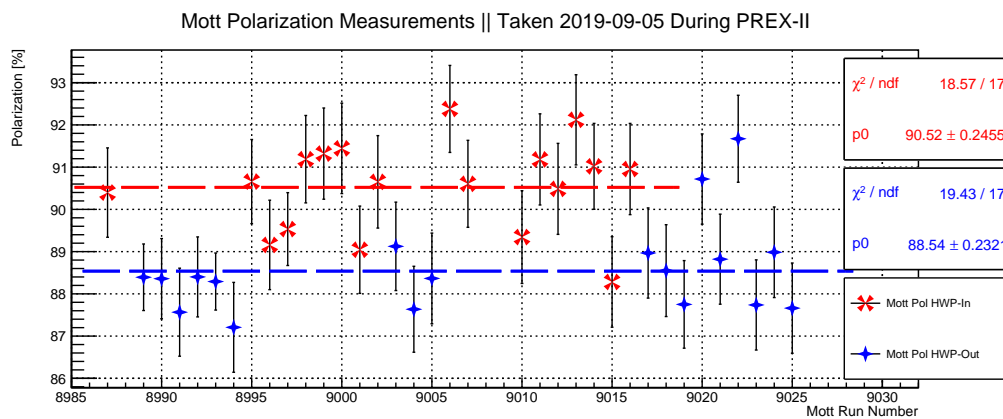


Figure 4.13: Mott polarimeter measurements taken on 9/5/2019 verified with reasonable precision that the HWP-IN/HWP-OUT difference first noticed by Møller polarimetry was real and not statistical in nature.

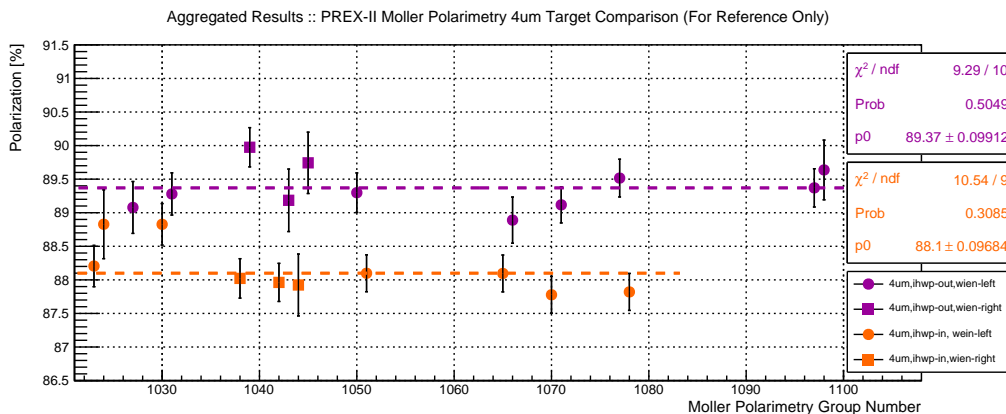


Figure 4.14: PREX-II Møller sign-corrected polarimetry measurements taken on the 4 μm iron foil separated by half-wave plate state and wien filter state. The error-weighted data was fit with a zeroth-order polynomial to arrive at average polarizations for each half-wave plate state across both Wien filter configurations.

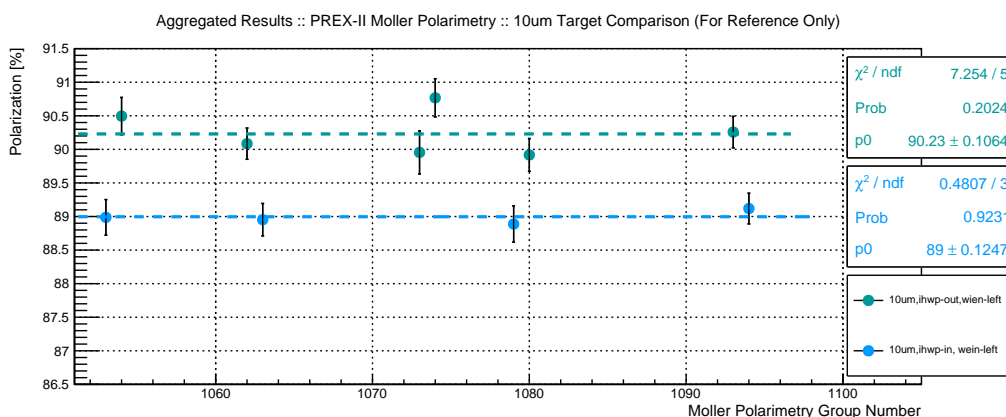


Figure 4.15: PREX-II Møller sign-corrected polarimetry measurements taken on the 10 μm iron foil separated by half-wave plate state. The error-weighted data was fit with a zeroth-order polynomial to arrive at average polarizations for each wave state.

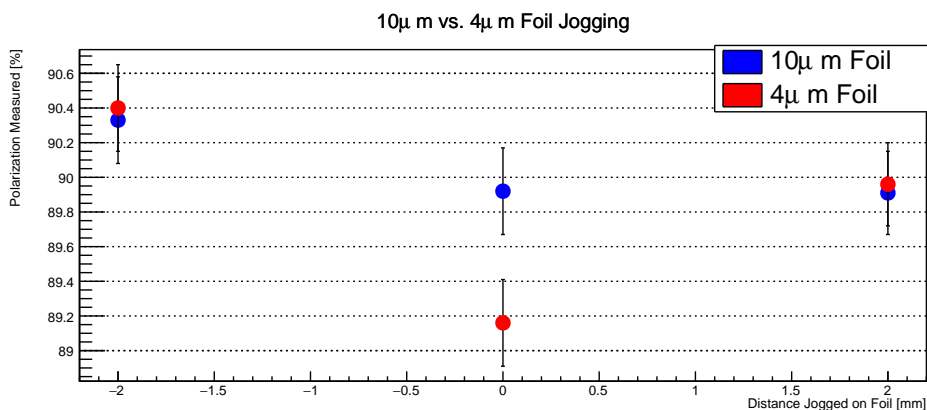


Figure 4.16: Polarization measurements made during foil jogging systematics studies on 4 μm and 10 μm foils demonstrating possible inconsistency with measurements taken on the 4 μm foil. Polarization values for the above plot are located in section A.5.

ratios on data from shifts which polarization data was available for both foils. The ratios were error-weighted and the errors were propagated into the ratios. These ratios were then fit with a zeroth-order polynomial in order to determine a mean conversion factor (see fig. 4.21). The conversion factor would be applied to measurements taken on the $4\mu\text{m}$ foil in order to scale them to the $10\mu\text{m}$ measurements. The scale factor calculated and used was 1.0110 ± 0.0015 .

At the conclusion of the PREX-II experiment the target ladder was removed from the Møller polarimeter and the foils were examined. The $4\mu\text{m}$ foil showed clear signs of wrinkling, presumably from the 4T field that was used to magnetically saturate it, while the $10\mu\text{m}$ foil appeared to be in excellent shape. Photographs taken of the two foils are shown in figs. 4.19 and 4.20.

Final Polarization Values

Following the calculation of the scaling factor polarization values were derived from the following set of data and separated into HWP-OUT and HWP-IN measurements:

- All $10\mu\text{m}$ foil measurements were used and any $4\mu\text{m}$ measurements taken on the same day were treated as systematic studies for the purpose of calculating the scaling factor.
- Any $4\mu\text{m}$ foil measurements which were taken on a day without a corresponding $10\mu\text{m}$ measurement were scaled using the scaling factor and used in the final calculation; the error of the scaling factor fit was added in quadrature to the statistical error of the original Group analysis result on the $4\mu\text{m}$ foil.

The error-weighted data were fitted to a zeroth-order polynomials in order to get an average polarization for each half-wave plate state over the course of the PREX-II experiment. A graphical summary with fit data can be seen in fig. 4.22. Final reported polarizations supplied to the experiment were $89.1\%\pm 0.1\%$ for the HWP-IN data and $90.3\%\pm 0.1\%$ for the HWP-OUT data.

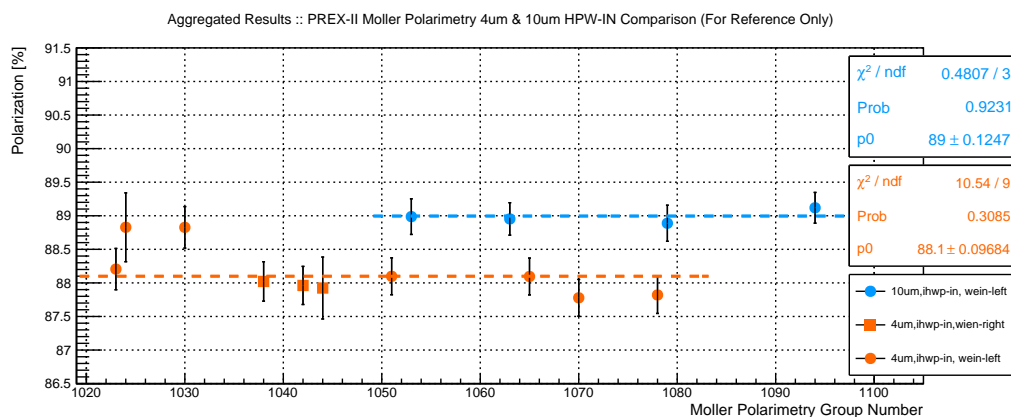


Figure 4.17: PREX-II sign-corrected polarimetry data taken on the 4 μ m and 10 μ m foils in the HWP-IN state. The error-weighted data were fit with a zeroth-order polynomial to capture a mean polarization. A difference of $\approx 1\%$ is demonstrated.

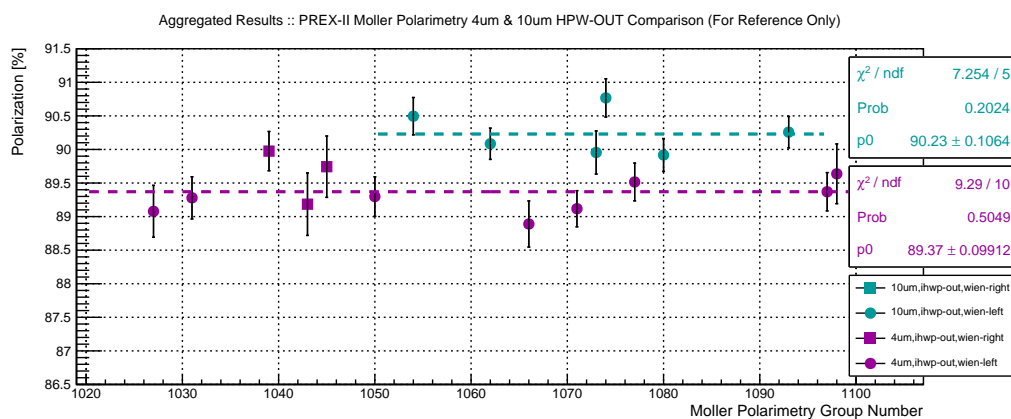


Figure 4.18: PREX-II sign-corrected polarimetry data taken on the 4 μ m and 10 μ m foils in the HWP-OUT state. The error-weighted data were fit with a zeroth-order polynomial to capture a mean polarization. A difference of $\approx 1\%$ is demonstrated.



Figure 4.19: Photo of 4 μ m foil taken after the PREX-II experiment had concluded. Foil wrinkling is clearly visible.



Figure 4.20: Photo of 10 μ m foil taken after the PREX-II experiment had concluded. Foil appears to be in excellent shape.

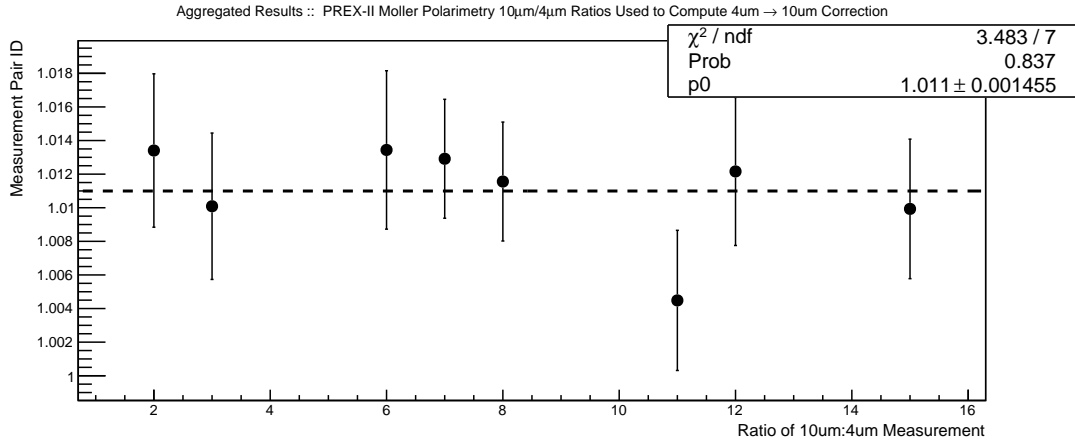


Figure 4.21: 10 μm -to-4 μm foil polarization ratios from data which was taken consecutively. Ratios were error weighted and the errors propagated. The error-weighted ratio data was then fit to a zeroth-order polynomial to get a conversion ratio for days which there was no 10 μm foil measurements.

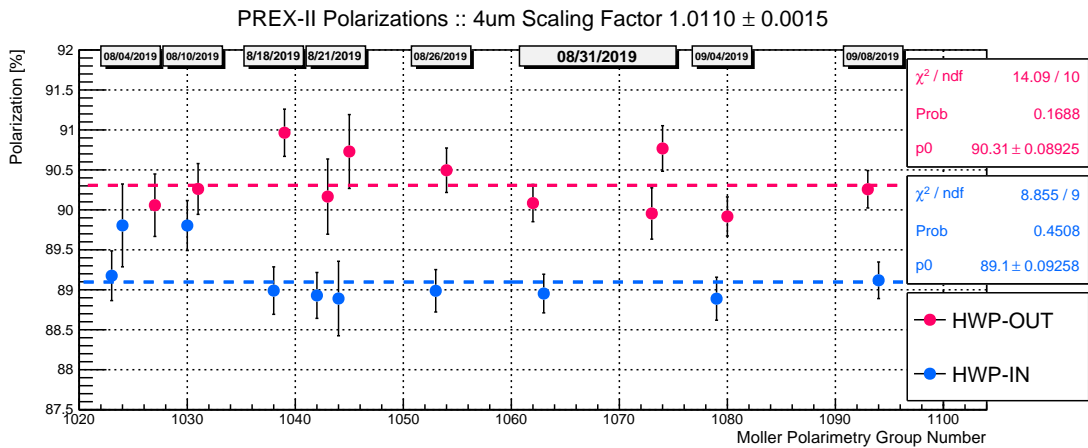


Figure 4.22: Final PREX-II Møller polarimetry results.

4.7.2 CREX

Møller polarimetry measurements were taken along with Compton polarimetry for the near-entirety of the CREX experiment. A tabled summary of Møller polarization measurements taken during CREX and analysis results can be found in table A.9. Møller polarimetry results are plotted alongside Compton polarimetry results over time in figs. 4.23 and 4.24; results are separated into two plots to avoid large time break due to COVID shutdown.

For CREX polarimetry, the Compton results will be used for the majority of the data

with the Møller polarimetry measurements serving as a cross-check and general comparison. For any CREX data taken prior to the time when the Compton started taking data the Møller polarimetry values will be used. Error-weighted mean polarization values for each half-wave plate state from the two Møller polarimeter measurements prior to the Compton start up— $P_{\text{Møller}}^{\text{IN}} = 86.83\% \pm 0.14\%$ and $P_{\text{Møller}}^{\text{OUT}} = 86.93\% \pm 0.14\%$ —and the error-weighted mean polarization values of the early Compton measurements— $P_{\text{Compton}}^{\text{IN}} = 86.62\% \pm 0.18\%$ and $P_{\text{Compton}}^{\text{OUT}} = 86.93\% \pm 0.19\%$ —are statistically consistent.

Overall Møller-to-Compton Comparison

In order to compare polarimetry results each Møller measurement would be compared against Compton measurements which occurred in a ± 2 day time window. This matching process yielded ten Møller measurements for which Compton measurements could be compared. Compton data was provided in a spreadsheet and this was used as the environment for the data analysis. For each of the 10 Møller measurements associated Compton 'snails' (the equivalent of a Møller Group) were identified and the weighted arithmetic mean was extracted along with a standard error. A plot of these measurements is shown in fig. 4.25 separated by Wien filter state and half-wave plate state. Weighted arithmetic means were then taken on the data: for all ten Møller and ten Compton data points available; for the pre-shutdown data points; and for the post-shutdown data points. The measurement means are also shown on fig. 4.23 as constant lines across the data with 1σ error bars. A summary of the weighted means and associated errors along with the difference of the means is given in table 4.3 for all three sets. In each of the three sets the mean Møller polarization and mean Compton polarizations the error bars on the averages kiss indicating that the measurements are consistent.

A second brief ratio analysis of the ten Compton/Møller data pairs is shown in fig. 4.26. Polarization ratios in the form of Compton-over-Møller. Individual measurement error was propagated by adding relative errors of the paired data points in quadrature. A weighted arithmetic mean was then taken from the 10 Compton/Møller ratios. The mean value of

Table 4.3: Calculated weighted arithmetic means of matched Møller and Compton measurements. Errors are absolute percent. Difference of the means is Compton minus Møller.

Data set:	All			Pre-Shutdown			Post-Shutdown		
Møller Mean Pol	87.08%	\pm	0.06%	86.72%	\pm	0.08%	87.43%	\pm	0.08%
Compton Mean Pol	86.99%	\pm	0.03%	86.67%	\pm	0.05%	87.52%	\pm	0.05%
Difference of Means	-0.09%	\pm	0.07%	-0.05%	\pm	0.09%	0.10%	\pm	0.10%

the Compton/Møller ratios is 0.9995 ± 0.0009 and is consistent with a value of 1 indicating that the Møller and Compton measurements are consistent within statistical error alone.

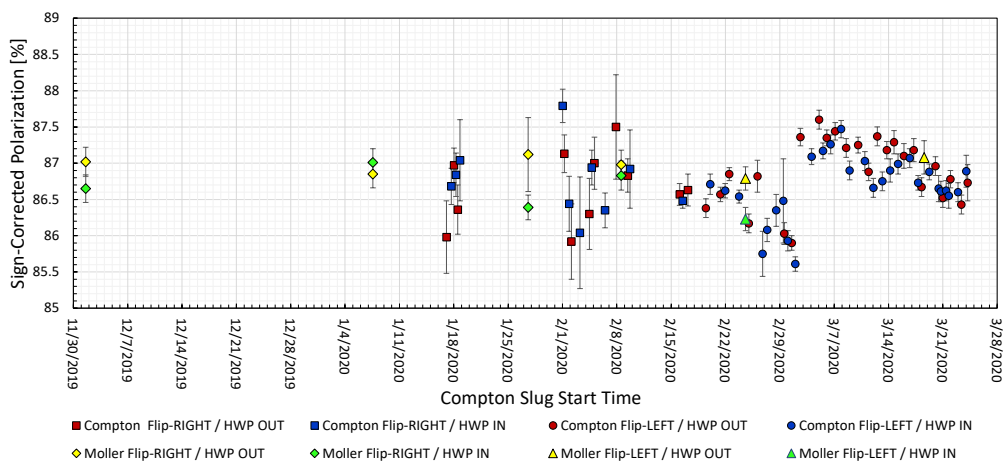


Figure 4.23: Overlay of measurements made by the Compton Polarimeter and Møller polarimeter during the period before the COVID shutdown.

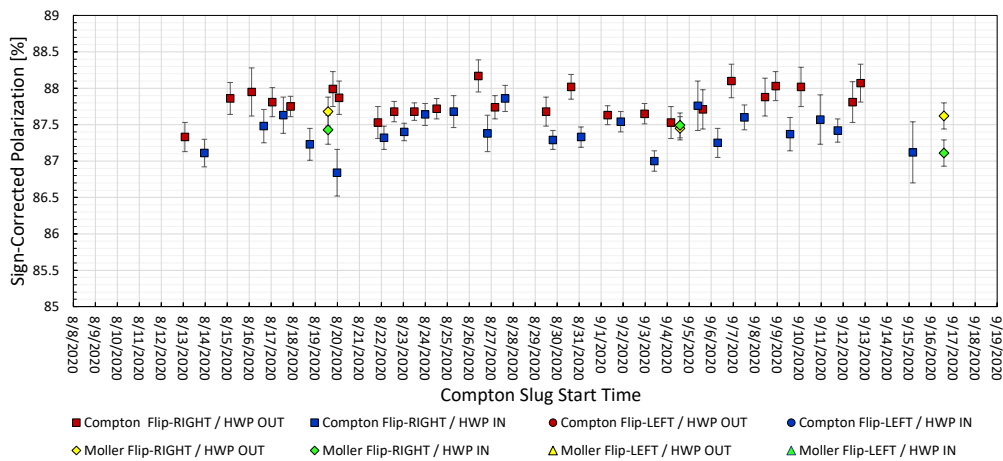


Figure 4.24: Overlay of measurements made by the Compton Polarimeter and Møller polarimeter during the period after the COVID shutdown. First Møller polarimetry measurements

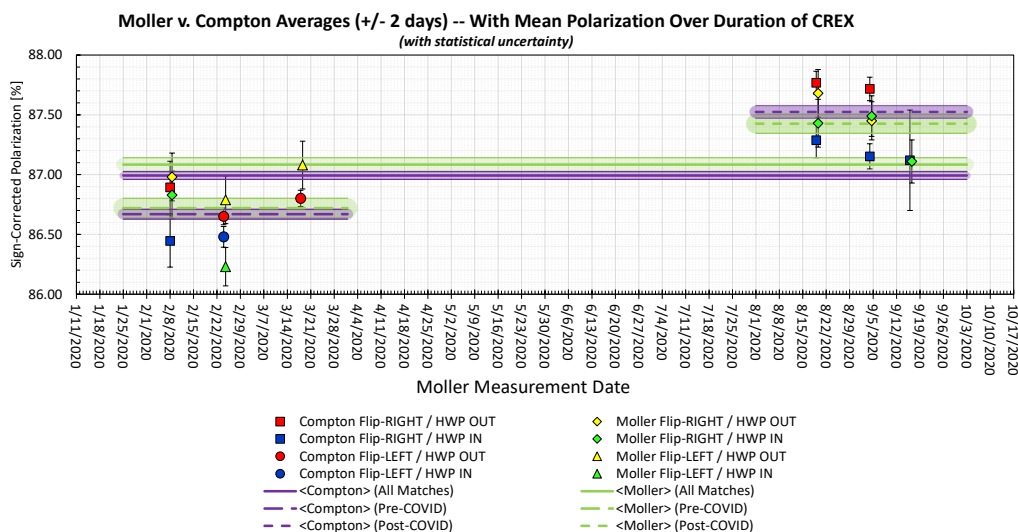


Figure 4.25: Comparison of Møller polarimetry measurements against error-weighted averages of any Compton polarimetry 'snails' which concluded in a ± 2 day period around the Møller measurements; there are a total of 10 Møller measurements which had associated Compton measurements. This comparison data was then averaged across half-wave plate states over the course of the whole experiment, over pre-COVID measurements only and post-COVID measurements only. Averages are plotted as constant lines are bounded by 1σ error bars which are lightly shaded.

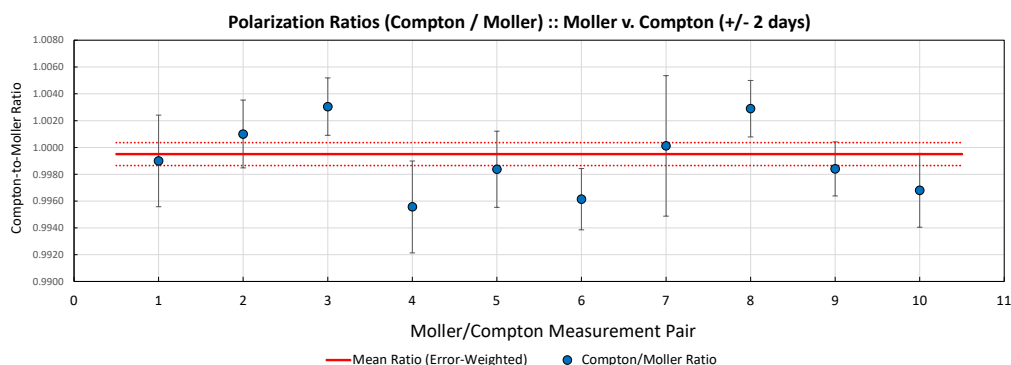


Figure 4.26: Ratios of Møller polarimetry measurements and error-weighted averages of any Compton polarimetry 'snails' which concluded in a ± 2 day period around the Møller measurements; there are a total of 10 Møller measurements which had associated Compton measurements. Compton-to-Møller ratios were taken from the available 10 pairs of data points. The mean Compton-to-Møller ratio was 0.9995 ± 0.0008 .

4.8 Møller Polarimetry Systematics

This section will deal with various systematic uncertainties in the calculation of the analyzing power and general systematic uncertainties of our final polarization result in two separate subsections.

4.8.1 Analyzing Power Systematics

The key component of Møller polarimetry is having a precise understanding of the spectrometer’s acceptance and calculating the analyzing power. There are various sensitivities and uncertainties that can have an effect the calculation of this value. The following will be a review of these systematics for both the PREX-II optics and CREX optics.

Quad 1 Sensitivity

As discussed in section 3.6 our primary tuning magnet is the first quadrupole magnet of the Møller spectrometer. Our diagnostic tuning method required us to find the rate maximum and then “overtune” the magnet from this rate maximum point by a prescribed amount; for PREX-II this prescribed amount is $\approx 3\%$ and for CREX it is 20%.

PREX-II Q1 Sensitivity

A review of Q1 scan data taken over the course of the PREX-II experiment compared against chosen Q1 magnet operating currents selected for asymmetry measurements was consistent with identifying rate maximum within the required accuracy of $\pm 2\%$. Additional asymmetry scan data taken on 8/10/2019—summarized in fig. 4.29 and table A.6—supports this conclusion. A select summary of simulated Q1 magnet detuning, analyzing powers and change in analyzing powers is given in table 4.4 and is a partial summary of data shown in fig. 3.16. Changes in the analyzing power at $\pm 2\%$ from the optimal magnet tune a maximum of +0.11%. A final systematic uncertainty of 0.12% for

the Q1 diagnostic tuning was assigned for PREX-II analyzing power systematics.

Table 4.4: Select summary of simulation data for PREX Q1 optics simulated asymmetry scan. Targeted diagnostic tuning point was 3% over the identified rate maximum—the $\delta A_{zz}/A_{zz}$ are relative to that tuning point.

Detuning From Optimal	Normalized Coincidence Rate	Corrected Analyzing Power	$\delta A_{zz}/A_{zz}$
-5.0%	96.0%	0.78328	1.32%
-4.0%	99.4%	0.77955	0.84%
-3.0%	100.0%	0.77641	0.44%
-2.0%	99.7%	0.77389	0.11%
-1.0%	99.0%	0.77325	0.03%
0.0%	97.9%	0.77304	0.00%
1.0%	96.5%	0.77340	0.05%
2.0%	94.7%	0.77380	0.10%
3.0%	92.3%	0.77446	0.18%

CREX Q1 Sensitivity

For the CREX optics tune there existed a much larger region of insensitivity which can be seen in fig. 3.19 compared to the PREX-II optics. A select summary of the analyzing powers from simulated scans is given in table 4.5. With full confidence that polarimetry data was taken in the effectively flat region of analyzing power of fig. 3.19 and backed up by asymmetry scan data shown in fig. 4.30 a very conservative estimate of being $\pm 10\%$ in our tuning was made. This estimate results in a maximum 0.1% systematic uncertainty on the analyzing power from the Q1 tuning being assigned.

Quad 2/4 Sensitivity

Sensitivity due to minor mischaracterizations of the Q2 and Q4 magnets was determined through a series of simulations. Since my diagnostic tuning method for Møller measurements was used, each simulation was run as follows: magnet settings for Q2 and Q4 were altered; new Q1 value chosen to coincide with coincidence rate maximum); and then high-statistics simulations were run at the 4% overtune from maximum rate for PREX-II and 20% overtune from maximum rate for CREX. Magnets Q2 and Q4 were

Table 4.5: Select summary of simulation data for CREX Q1 optics simulated asymmetry scan. Values that are $\pm 10\%$ detuned off of the targeted set point at 20.8% were interpolated from the simulation data and are shown in blue; these values are the basis for the systematic assignment.

Detuning From Rate Maximum	Q1 Pole Tip [T]	Normalized Coincidence Rate	Corrected Analyzing Power	$\delta A_{zz}/A_{zz}$
0%	0.24	100%	0.760989	0.89%
4.2%	0.25	99.3%	0.756944	0.36%
8.3%	0.26	98.4%	0.754804	0.079%
10.8%	—	—	0.754580	0.049%
12.5%	0.27	97.4%	0.754426	0.029%
16.7%	0.28	96.3%	0.754265	0.0073%
20.8%	0.29	95.2%	0.754210	0.0%
25.0%	0.30	94.0%	0.754244	0.0045%
29.1%	0.31	92.8%	0.754723	0.068%
30.8%	—	—	0.754911	0.093%
33.3%	0.32	91.3%	0.755203	0.13%

varied by $\pm 2.5\%$ resulting in nine separate simulations.

Table 4.6: Summary of PREX-II Q2/Q4 sensitivity simulation results. Maximum change in analyzing power highlighted in blue.

Q2 Uncertainty	Q4 Uncertainty	$\delta A_{zz}/A_{zz}$
-2.5%	-2.5%	-0.004%
-2.5%	0.0%	0.028%
-2.5%	2.5%	0.061%
0.0%	-2.5%	-0.013%
0.0%	0.0%	0.004%
0.0%	2.5%	0.054%
2.5%	-2.5%	0.052%
2.5%	0.0%	0.066%
2.5%	2.5%	0.069%

The original decision on using 2.5% as the uncertainty on the Q2 and Q4 quadrupole characterizations was based on the inability to replicate past measurements in simulation. After the discovery of the beam orbit issue (to be discussed) and easily reproducible results during CREX it was agreed upon that the Lab's standard acceptance of a $\pm 1\%$ uncertainty in the magnet characterization was most certainly sufficient. Given simulation results shown in table 4.6 that show a maximum change in analyzing power of around 0.07% and

considering that we over-compensated for magnet uncertainty a 0.05% systematic was applied for Q2/Q4 analyzing power sensitivity.

Dipole Sensitivity

The systematic particular to deviations in the dipole settings were determined by how well it is believed that the rate maximum was successfully identified when performing the dipole calibration scans prior to data taking. For PREX-II, the dipole was the somewhat more difficult/concerning magnet to tune with no particular very well defined features to look for but rather just a smooth-ish maximum which wasn't strongly peaked fig. 3.17 but did fit reasonably well to a curve; the potential problem was choosing a point that was too weak and in the region of analyzing power sensitivity.

A graphical summary of the dipole rate scans with simple second-order polynomial fits done in Excel can be seen in fig. 4.27. A more formal fitting fig. 4.28 was performed while assigning systematics in an attempt to constrain how far the choice of maximum may have been off-peak. With the exception of the measurements taken on 8/4/2020 (Group

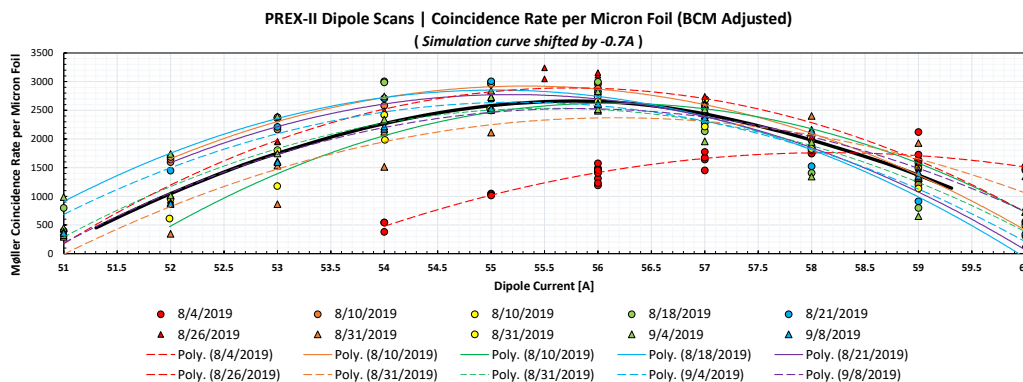


Figure 4.27: PREX-II dipole rate scan summary. Each point was an individual run. Run was fit with second-order polynomials immediately after data was being taken to provide guidance on locating rate maximum. Black band is predicted simulation curve shifted by 0.7A to line up average dipole scan peaks.

1021) the dipole currents for coincidence rate maximums were set at values between 55A and 56A. Dipole set points for each day are listed in table 4.7 as ‘Set’. At no point was a running point chosen that was more than 0.35 amps off of the formal ROOT fit values

which are shown in table 4.7 under the fit^{max} column; the less formal Excel fits fig. 4.27 were used to eye up the data because they're quick to look at when time is of the essence.

Table 4.7: PREX-II dipole scan second-order polynomial fit $f(x) = Ax^2 + Bx + C$ parameters and errors as performed in ROOT along with fit maximum $\text{fit}^{\text{max}} = -\frac{B}{2A}$ and $\text{fit}_{\text{error}}^{\text{max}}$ equal to the errors added in quadrature. Dipole Scan 1035 was a scan performed while altering the B.dl of the MBC1H01 (horizontal) corrector magnet to see if we could induce significant rate changes (45% loss) observed on 8/4/2019. Dipole scan 1069 was an end-of-shift check using the $4\mu\text{m}$ foil to check against dipole scan 1060 performed with the $10\mu\text{m}$ foil earlier in the day.

Date	Group	A	δA	B	δB	C	fit^{max}	$\text{fit}_{\text{error}}^{\text{max}}$	Set
8-4-2019	1021	-0.0246	0.000199	2.866	0.0225	-82.76	58.15	0.656	58.0
8-10-2019	1028	-0.0428	0.000339	4.733	0.0377	-129.87	55.29	0.621	55.75
8-10-2019	1035	-0.0381	0.000370	4.274	0.0410	-119.05	56.08	0.765	—
8-18-2019	1036	-0.0411	0.000457	4.523	0.0510	-123.24	54.90	0.869	55.25
8-21-2019	1040	-0.0433	0.000453	4.784	0.0505	-131.01	55.15	0.820	55.5
8-26-2019	1048	-0.0384	0.000256	4.293	0.0284	-118.92	55.77	0.524	55.75
8-31-2019	1060	-0.0799	0.000572	8.925	0.0635	-247.21	55.78	0.563	56.0
8-31-2019	1069	-0.0424	0.000413	4.719	0.0458	-130.28	55.57	0.764	—
9-4-2019	1075	-0.0375	0.000275	4.179	0.0304	-115.54	55.67	0.575	55.75
9-8-2019	1091	-0.0818	0.000705	9.137	0.0780	-253.23	55.81	0.676	55.75

After considering the dipole scan data taken over the course of PREX-II, looking at the fit data and some healthy discussion it was determined that we likely found the maximum dipole rate with a precision of about 0.5 amps. For the PREX-II optics tune, it was optimal to err slightly to the higher side of the mean since the analyzing power was stable in that direction. The average error on the fitted means is ≈ 0.65 amps which is $\approx 1\%$ off the mean rate peak. A conservative estimate of $\pm 1.5\%$ was taken as the uncertainty in the magnet current compared to rate peak. This uncertainty in the dipole calibration was then compared to simulation results which are partially summarized in table 4.8 to arrive at a conservative estimate for the uncertainty in analyzing power.

A generous 0.05% systematic which exceeds the analyzing power change for such a detuning was applied. Additional possible concerns about how beam orbit may have impacted dipole tuning are covered by the much more generous 'Beam Orbit' systematic to be discussed.

The CREX dipole sensitivity was effectively non-existent with a safe 4% under-tuning

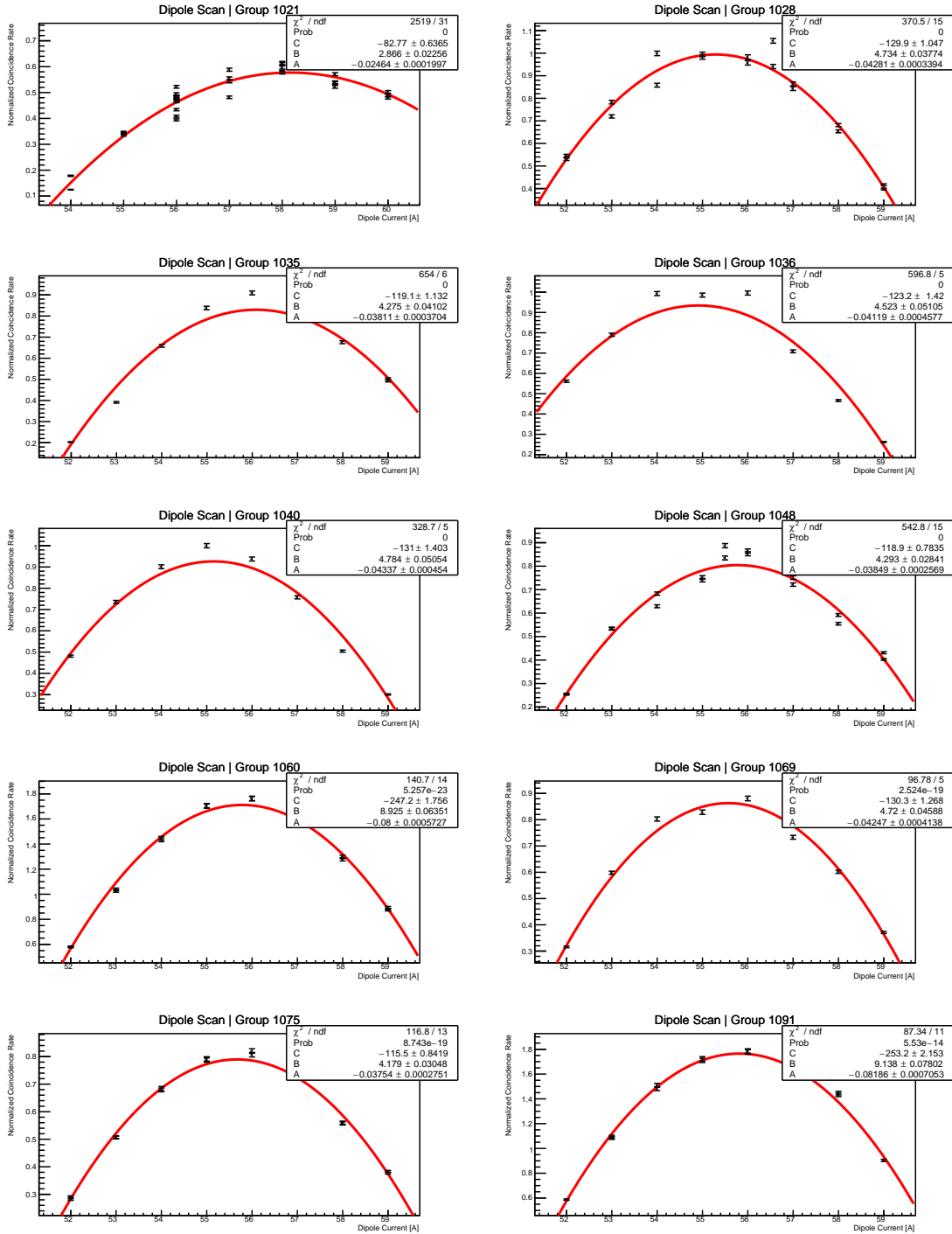


Figure 4.28: Fits of PREX-II dipole rate scans. A summary of this fit data can be seen in table 4.7. Møller coincidence rates are normalized to the recorded BCM recorded charge rate adjusted for pedestal. This data was utilized to place a limit on how well the rate peak was identified for the purpose of setting a systematic.

Table 4.8: Select summary of simulation data for PREX-II dipole optics scan. A -1.5% mistuning has a potential 0.05% asymmetry uncertainty impact.

Detuning Percentage	Normalized Coincidence Rate	Analyzing Power	$\delta A_{zz}/A_{zz}$
-1.5%	95.1%	0.773820	-0.044%
-1.0%	98.0%	0.773963	-0.025%
-0.5%	99.4%	0.774077	-0.011%
—	100%	0.774159	—
0.5%	99.5%	0.774207	0.006%
1.0%	98.0%	0.774224	0.008%
1.5%	95.5%	0.774215	0.007%

region off of the Møller rate peak and did not require the same level of scrutiny as the PREX-II systematic did.

Detuning Percentage	Normalized Coincidence Rate	Uncorrected Analyzing Power	$\delta A_{zz}/A_{zz}$
-8%	79.7%	0.759345	0.531%
-7%	84.9%	0.757785	0.324%
-6%	89.7%	0.756272	0.124%
-5%	93.8%	0.755227	-0.089%
-4%	96.7%	0.754875	-0.061%
-3%	98.5%	0.754894	-0.059%
-2%	99.4%	0.755054	-0.037%
-1%	99.9%	0.755211	-0.017%
—	100.0%	0.755337	0.000%
1%	99.1%	0.755787	0.060%
2%	96.9%	0.756720	0.183%
3%	94.1%	0.757744	0.319%
4%	91.2%	0.758775	0.455%
5%	88.2%	0.759829	0.595%
6%	85.1%	0.760857	0.731%

Table 4.9: Select summary of simulation data for CREX dipole optics scan.

Levchuk / Radiative Model Uncertainty

Levchuk effect and radiative model uncertainty was determined from two sets of experimental polarimetry data taken—one during PREX-II running and one during CREX running. These data sets were taken at various points of quadrupole detuning and

then compared against simulated expectations.

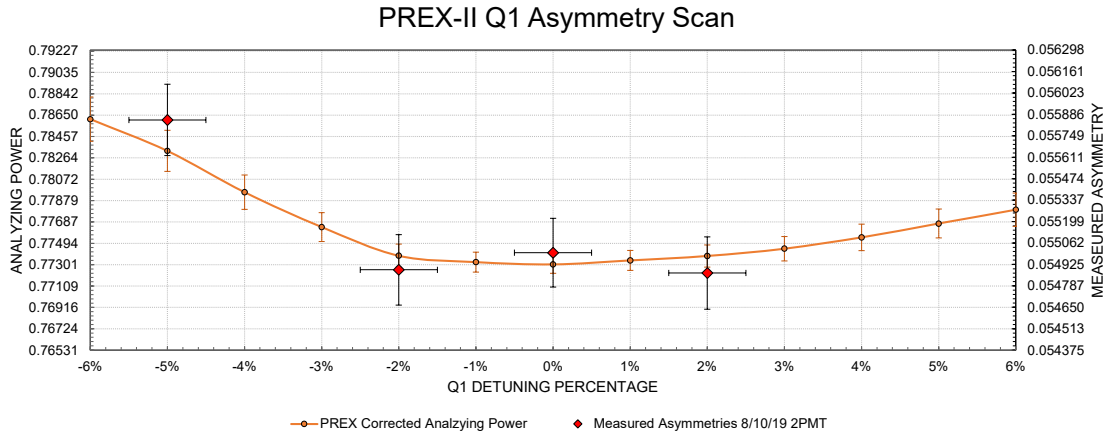


Figure 4.29: Asymmetry data taken during PREX-II experiment on 8/10/2019. Measured asymmetries shown on right-hand vertical axis and correspond to analyzing powers on left-hand vertical; scaling factor calculated as prescribed in eq. (3.12). Vertical error bars equal to statistical error on asymmetry scan measurements and statistical error on standard daily polarization measurement used for converting the measured asymmetry to analyzing power added in quadrature.

Data obtained during the PREX-II experiment can be seen in fig. 4.29 and is summarized in table A.7. The horizontal chart bars in fig. 4.29 represent a 0.25% change in analyzing power off the expected central tune value of 0.77301, corresponding asymmetry values are labeled on the secondary axis using a beam polarization of 89.8% and measured asymmetries are plotted with error bars. Horizontal error bars reflect uncertainty in magnet characterization map and the vertical error bars are statistical uncertainty on the measurements. From the PREX-II asymmetry data it appears that our computational corrections are reasonable.

Data obtained during the CREX experiment can be seen in fig. 4.30 and summarized in table A.7. Error bars, here, represent a 0.5% change in analyzing power off the central tune value of 0.75421, corresponding asymmetry values are again labeled on the secondary axis using the beam polarization of 86.62% and measured asymmetries are plotted with error bars. Horizontal error bars again reflect a 1% uncertainty in magnet characterization and the vertical error bars are again the statistical uncertainty on the measurements. It is clear from the CREX asymmetry data that our modeling of the Levchuk effect, while generally fine at our optimal optics tune, could use improvement.

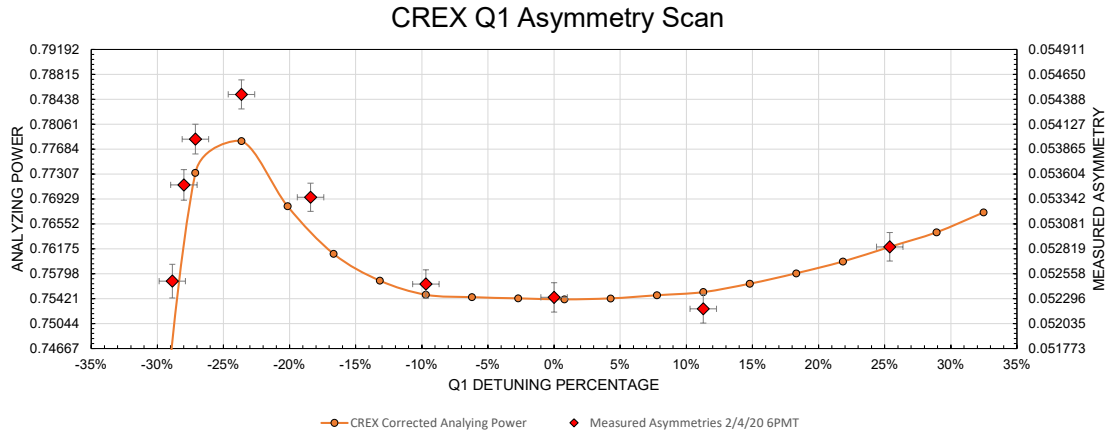


Figure 4.30: Detailed asymmetry data taken during CREX experiment on 2/8/2020. Measured asymmetries shown on right-hand vertical axis and correspond to analyzing powers on left-hand vertical; scaling factor calculated as prescribed in eq. (3.12). Error bars equal to statistical error on asymmetry scan measurements and statistical error on standard daily polarization measurement used for converting the measured asymmetry to analyzing power added in quadrature..

Looking the -8% off-tune point in the CREX asymmetry data in tables A.6 and A.7 it can be seen that the measured asymmetry is $\approx 4\%$ from the central optics tune asymmetry/analyzing power while the model predicted that there should be an $\approx 3\%$ deviation. From this the decision was made to apply a 30% systematic on our understanding of the Levchuk (and radiative corrections) models used in simulation. For both PREX-II and CREX, the predicted size correction from the Levchuk Effect and radiative corrections models on the central tune asymmetry was -0.2% ; this results in a systematic uncertainty in the analyzing power due to Levchuk and radiative corrections of 0.06% .

Beam Orbit Studies

Beam orbit going into the polarimeter was a problem during PREX-II. The problem after measurements taken on 8-4-2019 when coincidence rate scans were less than 50% of expected rate. A summary of Q1 rate scans performed in August 2019 is shown in fig. 4.31. In order to rectify the issue and additional wire scanner would be installed; however, that was unable to occur until after the PREX-II experiment had concluded. Significant efforts were made in the setup for polarimetry measurements taken during PREX-II to ensure that we were running as close to optimum setup as possible.

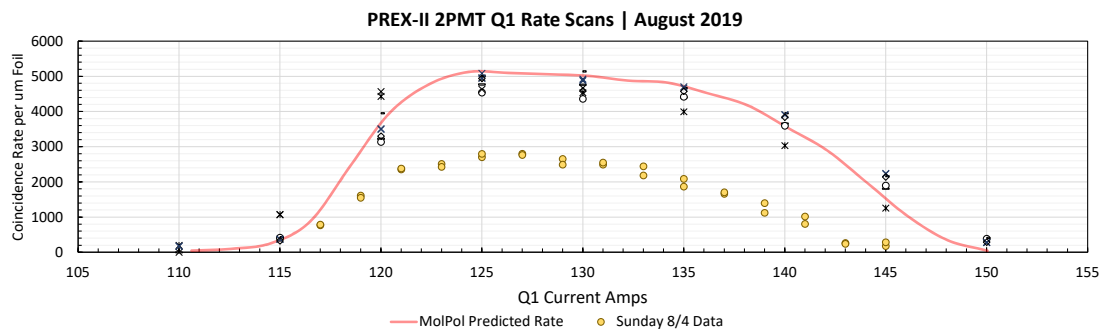


Figure 4.31: Summary of rate scans performed in August 2019 during the PREX-II experiment. Simulation predicted rate is shown against magnet current. Measurements taken on 8-4-2019 are highlighted in gold circles while all other measurements are simply marked.

Simulated studies were performed looking at the effects the beam entering the polarimeter holding field on an angle at one to two millirads were performed as were simulations of the beam striking the target significantly off-center ($\pm 1\text{mm}$). The systematic assigned for this beam orbit uncertainty was agreed upon to be the largest percent changes in analyzing power for both position and angle deviations added in quadrature. This yielded a value of 0.25%. A conservative 0.3% systematic was assigned to beam orbit concerns.

Lead Block Bleedover

The Møller polarimetry measurements for the PREX-II and CREX experiments only utilized a portion of the Møller calorimeter in order to constrain our acceptance. This presented a concern over how much of an impact signal sharing between neighboring lead blocks could potentially have on our calculation of the analyzing power.

First, ADC data from a data run taken during the March 2019 Commissioning period was inspected to discern whether or not this was a major concern; plots of the ADC data are shown in fig. 4.32. The amount of bleed over between blocks was deemed not problematic after data inspection of several runs and a toy study was performed as a follow-up to gauge the resultant systematic uncertainty.

A mock-up of the of method used in this toy model study is depicted in fig. 4.33. The simulations were designed such that all events which struck the lead blocks connected

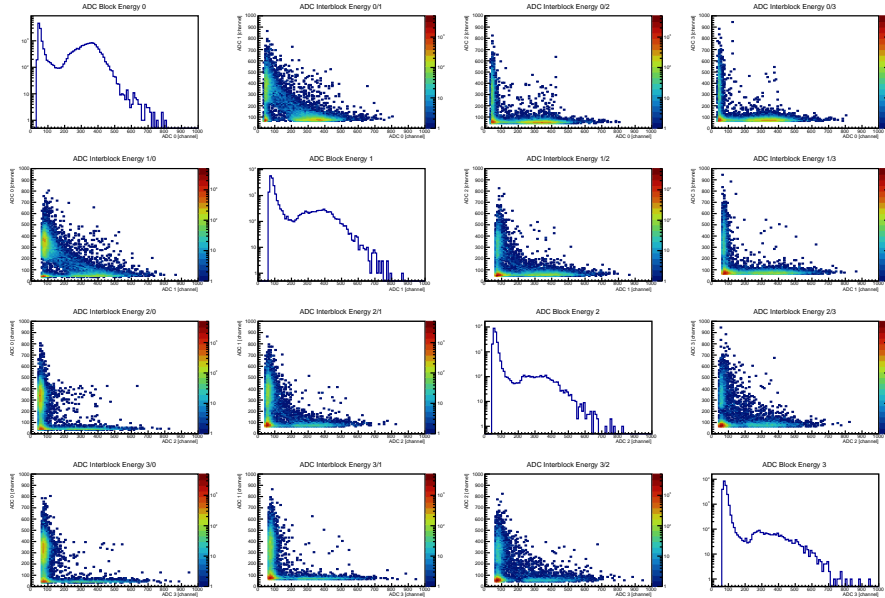


Figure 4.32: Plots of ADC data for the left arm of the Møller calorimeter (Blocks 0-3) from a commissioning run for PREX-II utilizing the 8PMT configuration. Off-axis scatter plots of PMTs 0/1, 1/2, and 2/3 are of interest and show small amounts inter-block energy bleedover. In this optical setup the 0/1 block boundary would be expected to have the largest amount. On-axis plots are histograms of signal distributions recorded by the ADC for each PMT.

to active PMTs were counted in addition to some fraction of hits which occurred up to one Molière radius (20mm) away. A simple linear probability was assumed such that at the edge of the active lead block the probability of acceptance was 100% and at 20mm away from the active edge of the lead block probability of acceptance decreases to 0%. Simulations were run on several seeds and analysis was performed as prescribed; results showed that in the 2-PMT optics setup for PREX-II having two inactive PMT neighbors there was a nominal -0.08% change in analyzing power. A similar percent change considering only one active edge when utilizing 6 PMTs was found for the CREX optical setup and yielded a -0.04% change in analyzing power.

Phi Acceptance

A systematic on the ϕ acceptance was calculated. Two physical components of the spectrometer have an effect on the ϕ acceptance—the Pb collimator jaws at the entrance to the dipole and the solenoid which twists the acceptance and causes changes to the

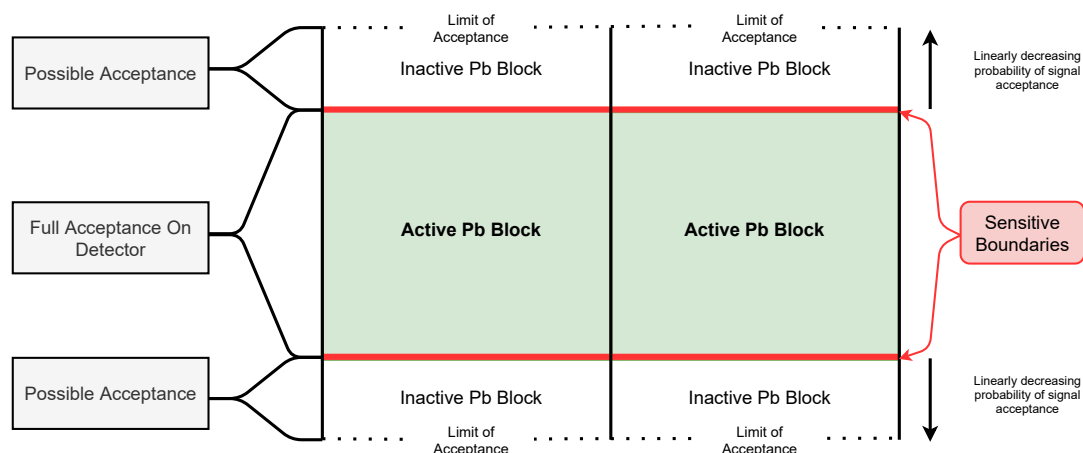


Figure 4.33: Visual depiction of shower-bleedover systematic simulation study for the 2PMT PREX-II optics setup (CREX optics included only one sensitive edge). Region of "possible acceptance" limited to one Molière radius.

coincidence ϕ distribution. Nominal changes in the cross-sectional acceptance were noted. systematic uncertainties of 0.03% and 0.01% were applied for the PREX-II and CREX respectively.

4.8.2 General Systematics

This section will review the assignment of general and analysis systematics for both PREX-II and CREX.

Foil Polarization

Foil polarization uncertainties are the largest systematic source of error for the Møller polarimeter. This comes from a few separate contributions. The first contributor is how well we know that the target foil was aligned perpendicular to the beam—this would include wrinkling in the foils as well as small angle deviations in the target ladder. For PREX-II and CREX the alignment and saturation uncertainties were given a conservative 0.50% systematic uncertainty. Next is the uncertainty in the target foil polarization value used at an estimated 2940K which contributes a 0.28% systematic uncertainty. Additionally, there's an uncertainty due to target heating with a 0.6 μ A beam current which would induce a change of approximately 12 K in the foil temperature; this contributes

a 0.02% uncertainty in the target foil polarization. Finally, for PREX-II only, was the application of a systematic uncertainty for the 4 μm -to-10 μm scaling which was assigned a total systematic contribution of 0.26%. In total, the target foil polarization systematic uncertainty for PREX-II was 0.63% and for CREX was 0.57%.

4 μm -to-10 μm Scaling

Additionally for PREX-II, included under the foil polarization uncertainty due to the 4 μm -to-10 μm scaling. This included the relative error of the 10 μm /4 μm data shown in fig. 4.21 which is approximately 0.15% along with some conservative estimates for unknown systematics.

Deadtime

The distribution of dead time corrections are shown in fig. 4.34. In the PREX-II data three distinct distributions in the run are representative of different operating currents over the course of the experiment and given eq. (4.19) these differences were to be expected. The mean dead time correction for PREX-II was 0.052% and for CREX the average dead time correction was 0.15%. The CREX dead time correction was higher and is consistent with expectations given that data collection rates were better. A 100% systematic uncertainty was applied for dead time corrections for both the PREX-II and CREX polarization results.

Bleed through

Bleed through is an issue where beam electrons intended to reach one hall end up in another hall. Special bleed through measurements are made to determine how much bleed through the experimental hall is receiving. These runs are performed when the other Halls are actively taking production data. CEBAF closes the slit aperture to eliminate electrons which may originate from the Hall A laser ensuring that any current coming into the experimental hall was intended to go elsewhere. Data from these bleed through

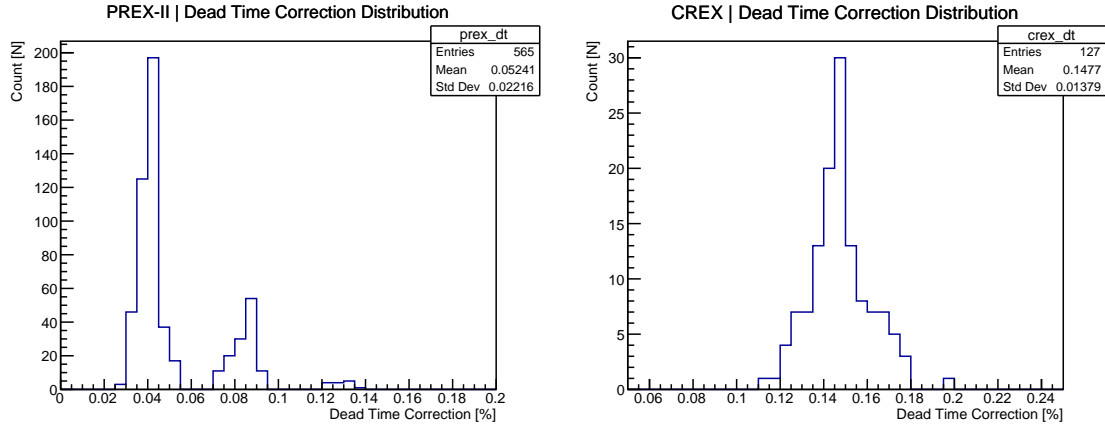


Figure 4.34: Møller polarimetry dead time correction percentages per data run for the PREX-II and CREX experiments.

runs is examined for coincidence hits counted by the Møller detector; these rates are then compared to the average Møller coincidence rate for that day.

There was no high-current experiments running in Hall C during the PREX-II experiment and Hall B and Hall D are low current. There was no meaningful bleed through during the PREX-II experiment’s Møller polarimetry measurements. During CREX, however, Hall C was running high-current experiments and bleed through was experienced. A summary of these measurements is shown in table 4.10.

An average of 0.09% bleed through was seen on average during CREX with days while Hall C was receiving beam being clearly evident. Since Hall-C’s polarization was opposite that of Hall-A’s during CREX this value was doubled to 0.18% which was assigned as the systematic uncertainty due to bleed through.

dP/P (Spin Precession)

When the electrons are bent as they pass through the accelerators recirculating arcs or bent as they are going into the experimental halls they experience spin precession. This precession is dependent on the beam energy as shown in eq. (2.1). Variation in the beam momentum dP/P results in an uncertainty in the precession of the beam electrons. The calculation of the uncertainty due to this variation is straight forward.

Table 4.10: Summary of bleed through measurements recorded during Møller polarimetry measurements during the CREX experiment.

Date	Percentage
12-01-2019	0.022%
01-07-2020	0.005%
01-27-2020	0.20%
02-08-2020	0.13%
02-24-2020	0.13%
03-18-2020	0.0%
08-19-2020	0.12%
09-04-2020	0.12%
09-16-2020	0.02%
Average	$\approx 0.09\%$

Assuming a maximum dP/P loss of $4(10^{-4})$ and energies of 0.98 GeV for PREX and 2.178 GeV for CREX and assuming a single half-pass is equal to one-half of the total energy we have the following:

$$\Delta\Phi_{PREX} = \frac{\left(\frac{1}{2}\right) 980 \times 4(10^{-4})}{440.65} \pi + \frac{980 \times 4(10^{-4})}{440.65} \left(\frac{37.5}{180} \pi\right) = 0.000196$$

$$\Delta\Phi_{CREX} = \frac{\left(\frac{1}{2}\right) 2178 \times 4(10^{-4})}{440.65} \pi + \frac{2178 \times 4(10^{-4})}{440.65} \left(\frac{37.5}{180} \pi\right) = 0.000431$$

In addition to these $\Delta\Phi$ we will also make the assumption our starting Φ was up to 5° off longitudinal (small deviations in the Wein angle that may be off maximum are difficult to determine but increase sensitivity to precession). We compute the uncertainty in polarization by taking the change in the longitudinal component between Φ and $\Phi + \Delta\Phi$. For PREX-II this leaves us with a 0.02% systematic and for CREX a 0.039% systematic for precession.

Accidentals

Accidental corrections as defined by eq. (4.31) made on the PREX-II and CREX data are shown respectively in fig. 4.35. Data was fit with a Gaussian and a systematic equal to

20% of the of Gaussian mean was assigned for each experiment. For PREX-II this works out to be a systematic uncertainty of 0.023% and for CREX a systematic uncertainty of 0.038%.

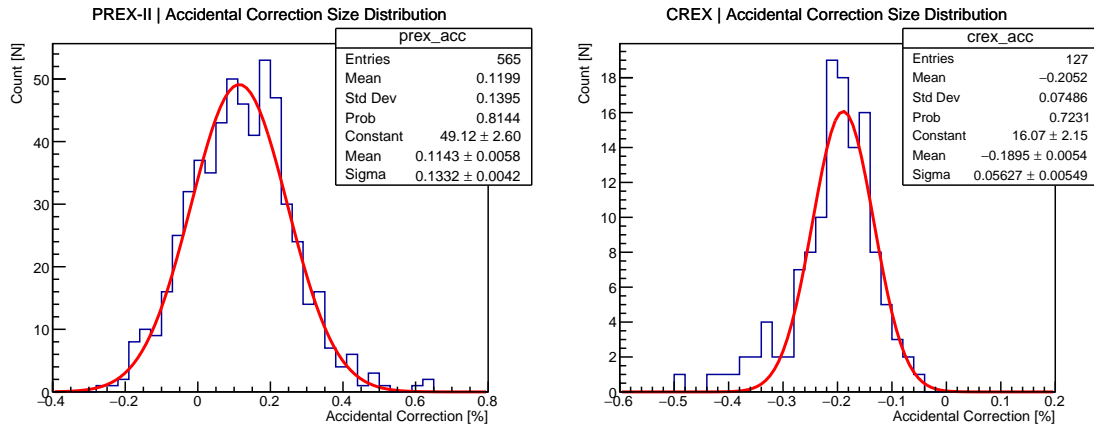


Figure 4.35: Møller polarimetry charge normalization correction percentages per data run for the PREX-II and CREX experiments.

Charge Normalization

The inherent charge asymmetry of the beam results in an additional systematic for the analysis as was reviewed in section 4.4.2. Charge normalization corrections to the data can be seen in fig. 4.36. During PREX-II, the Møller DAQ charge asymmetry was consistent with the Parity DAQ charge asymmetry taken during explicit PITA adjustments [68]. Since the changes in the charge asymmetry were consistent during these PITA adjustments no systematic was applied for the charge correction for PREX-II polarimetry data. Since there was no available PITA adjusted data taken during CREX Møller polarimetry measurements, simultaneous data was taken on the Møller DAQ and the Parity DAQ at high current before the close of the experiment and the difference in the measured charge asymmetry was 32%. The mean charge normalization correction for CREX Møller polarimetry data runs, shown in fig. 4.36 and taken to be the larger of the arithmetic and Gaussian means, was 2.9%; from this a systematic of 0.1% was assigned.

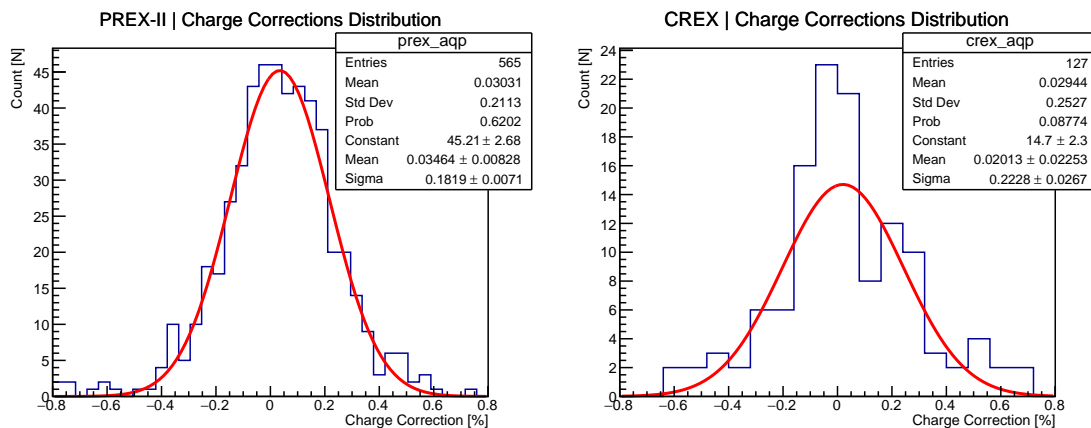


Figure 4.36: Møller polarimetry charge normalization correction percentages per data run for the PREX-II and CREX experiments.

Slit Dependence

Møller polarimetry is often run at sub-1 μ A currents which are too low for CEBAF to be capable of directly producing from the laser. In order to work around this there are two primary methods used to lessen the beam current delivered to the hall: A physical aperture referred to as the “slit” which is located downstream of the photogun; and a variable neutral-density filter used to reduce laser intensity before the laser reaches the photogun. A third method utilizing a “beat-frequency” beam mode can deliver low current to the hall by delivering only a fraction of the original beam [69] while still having the full laser current on the photocathode.

A 2007 Hall C systematic study investigating slit usage during Møller polarimetry measurements compared polarimetry data taken using the beat-frequency method of reducing current and the slit control method. Data from this study, shown in fig. 4.37 was used to extrapolate a systematic uncertainty for the slit conditions during the Hall A Møller polarimetry measurements taken for PREX-II and CREX. The Hall C study demonstrated consistent polarization with a difference of $0.24\% \pm 0.27\%$. Whereas the Hall C slit attenuation during this study was an average of 96% the slit attenuation during the Møller polarimetry measurements for PREX-II and CREX was an average of 60%. This 0.51% uncertainty at a 4% transmission can be used to extrapolate an uncertainty at a 40%

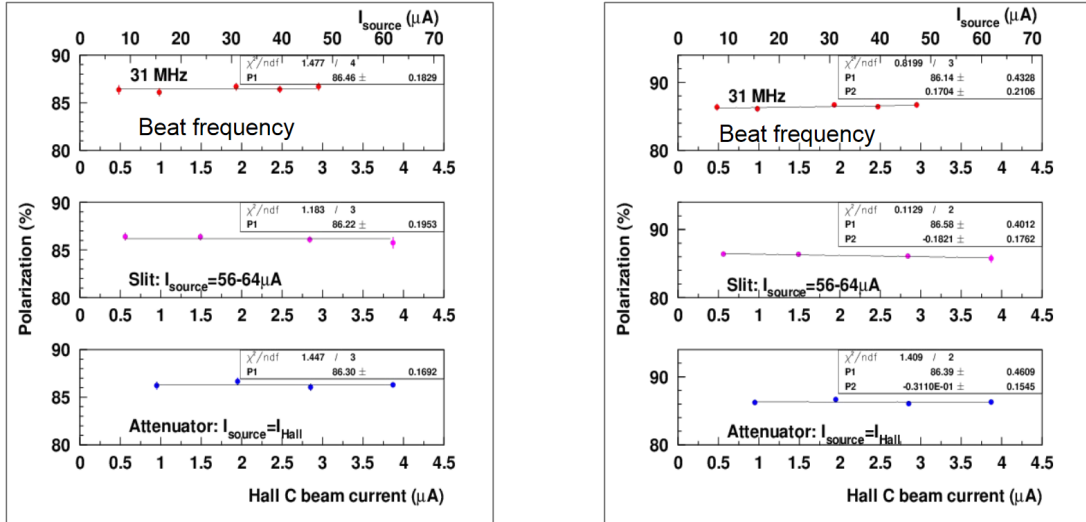


Figure 4.37: Data from a 2007 Hall C study performed to help place limits on systematic concerns about current-dependent polarization changes. The study used three methods for controlling the beam current delivered to the experimental hall. Polarization measurements were taken for each method and zeroth-order fits (left-panel) and first-order polynomial fits (right-panel) were made to the data. [Image of data courtesy of David Gaskell]

transmission of 0.05%; a conservative systematic of 0.1% was assigned for slit dependence for both the Møller polarimetry results for the PREX-II and CREX experiments [70].

Current Dependence a.k.a. High Current Extrapolation

Møller polarimetry measurements are performed at low currents typically around $0.5\mu\text{A}$ compared to the PREX-II and CREX experiments which ran at currents of $70 - 80\mu\text{A}$ and up to $120\mu\text{A}$. Current dependent effects may exist at the cathode level which cause minor changes to the polarization as current increases. There are two considered potential mechanisms for this potential dependence. First may be that the heating of the cathode introduces minute changes to the energy levels and/or P-shell $\frac{3}{2} \rightarrow \frac{1}{2}$ energy gap for which the laser is finely tuned to avoid crossing. The second method concerns correlations to low quantum efficiency (QE) of the cathode and beam polarization; although QE is monitored and PREX-II and CREX did not run during excessively low QE periods.

Again, the 2007 Hall C study data fig. 4.37 will be used to assign a systematic value. The beat-frequency data, attenuator data and slit data were combined to extract an upper

limit on this potential systematic. A final systematic assignment of 0.4% was made for PREX-II polarimetry data and 0.5% for CREX

Null Asymmetry

To check for potential false asymmetries and verify that we indeed get a zero-asymmetry when we should polarization measurements were taken on a Cu foil. The mean polarizations of these measurements as calculated in the MOLANA analysis can be found in tables A.3 and A.4. Results from the Cu foil measurements were fit with a zeroth-order polynomials and were consistent with zero and are shown in figs. 4.38 and 4.39. Systematic uncertainties were assigned as the absolute value of the mean deviation from zero plus the error bar of the fits and divided by a purposefully underestimated Møller asymmetry of 0.53 which serves to slightly overestimate rather than underestimate the systematic. These values were compared as a cross-check data against the assigned systematic uncertainties of 0.11% for PREX-II [71] and 0.22% for CREX [72].

PITA Variation

The main PREX-II and CREX experiments utilizes a active charge feedback system that modifies PITA voltage on the Pockels cell in order to minimize charge asymmetry. While this active charge feedback does not run during Møller polarimetry measurements the last settings of the PITA voltage dictated by the feedback system were still active when the first Møller polarimetry measurement began. The implication of this is that the polarization measurements made may not be wholly representative of the mean polarization during the main experiment's production runs. It was determined that the contribution from PITA variation contributed a 0.1% systematic to the polarimetry measurements for the PREX-II experiment [73] and a 0.6% systematic to the polarimetry measurements for the CREX experiment [74].

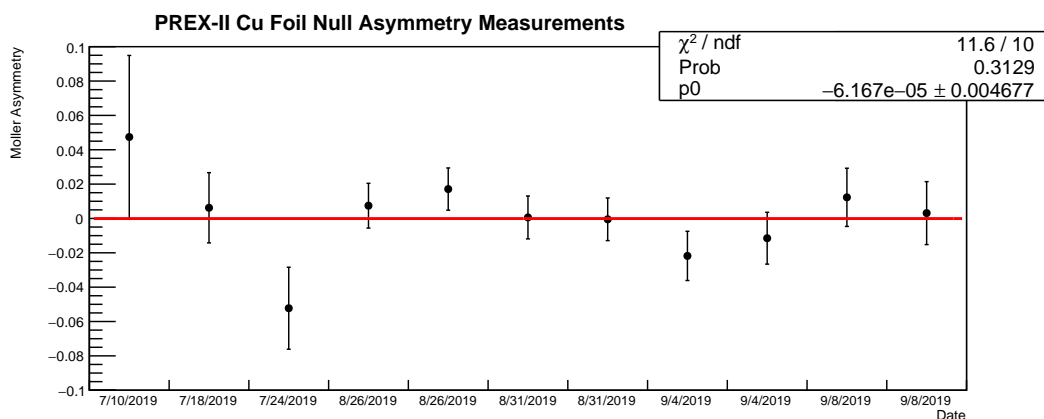


Figure 4.38: Møller asymmetry for Cu foil measurements taken during PREX-II; bins marked by date taken. Measurements are HWP/Wien sign-corrected.

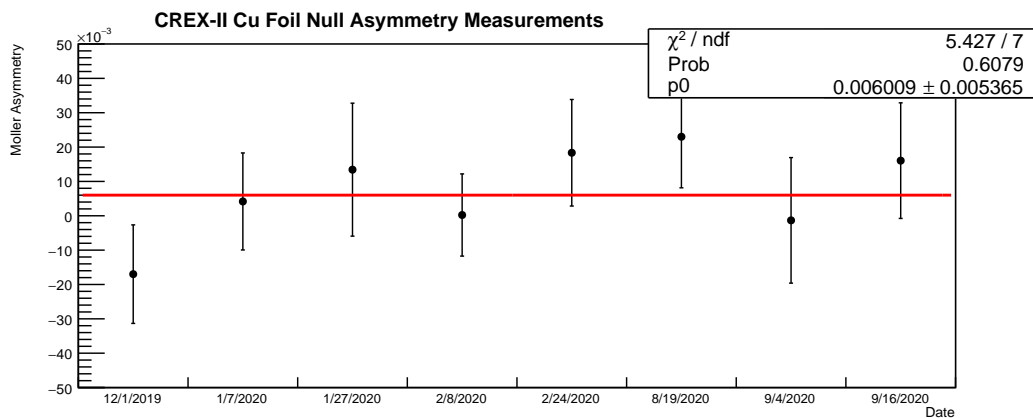


Figure 4.39: Møller asymmetry for Cu foil measurements taken during CREX; bins marked by date taken. Measurements are HWP/Wien sign-corrected.

July Running

Unfortunately, there were no usable/reliable Møller polarimetry measurements taken during the month of July. A collective determination was made that a proportional 1% error bar would be added to the systematics for uncertainty due to these lack of measurements. The PREX-II experiment accumulated 24% of its total good charge during the July time frame; as such, a 0.24% systematic was applied.

4.8.3 Systematics Summary

PREX-II

The analyzing power systematics for PREX-II are summarized in table 4.11; added in quadrature they contribute a 0.36% uncertainty to the analyzing power. Overall, these represent a significant improvement in the understanding of the Møller polarimeter's acceptance and in the control of uncertainties due to the Levchuk effect. Total Møller polarimetry systematics for PREX-II are summarized in table 4.12 and when added in quadrature total 0.89% [percent polarization].

CREX

The Møller polarimetry systematics for the CREX experiment are summarized in tables 4.13 and 4.14. The Møller polarimetry analyzing power systematics for the CREX experiment added in quadrature total to 0.16% and represent a general improvement over the PREX-II systematic uncertainty on the analyzing power. Primarily responsible for the drop in systematics was the partial detector—6PMT usage—setup which eliminated sensitivities to deviations in changes to the cross-section of Møllers which were successfully transported through the optical elements since the detector defined the acceptance. The insertion of an addition wire scanner prior to the polarimeter allowed better control over the beam orbit as it enters the polarimeter; this additional control constrained the uncertainty in the beam orbit sufficiently enough that any likely deviations in orbit

combined with the partial detector setup eliminated sensitivities to both position and angle changes.

There were systematic uncertainty increases for CREX in dead time, null asymmetry and bleed through. The null asymmetry systematic uncertainty increase was an unfortunate carryover effect from limited statistics due to magnet quenching issues which prevented Cu foil measurements from being taken; while the dead time systematic increase (and to a much more limited effect the accidentals systematic) was to be expected from the overall increase in detector rates. Bleed through from Hall C who was running a higher-current experiment at 30μ was an unexpected and undesirable addition. The final systematics assignment for CREX Møller polarimetry was 0.85% [percent polarization].

Table 4.11: Summary of Møller polarimetry analyzing power systematics for the PREX-II experiment.

Uncertainty Source	$\delta A_{zz}/A_{zz}$ (%)
Q1	0.12
Q2/Q4	0.05
Dipole	0.05
Levchuk / Radiative Corrections	0.06
Holding Field Alignment	0.05
Beam Orbit	0.30
Lead Block Bleedover	0.08
Phi Acceptance	0.03
Monte Carlo Statistics	0.09
Total	0.36

Table 4.12: Summary of Møller polarimetry systematics the PREX-II experiment.

Source	Value	$\delta P/P$ (%)
A_{zz}	0.77304	0.36
Foil Polarization	0.08005	0.63
Dead Time Correction	0.00051	0.05
Null Asymmetry (Cu Foil)	0.0	0.10
Accidental Correction	0.0012	0.02
PITA Variation	—	0.10
Spin Precession (dP/P)	—	0.02
High Current Extrapolation	—	0.40
Slit Dependence	—	0.10
July Running	—	0.24
Total		0.89

Table 4.13: Summary of Møller polarimetry analyzing power systematics for the CREX experiment.

Uncertainty Source	$\delta A_{zz}/A_{zz}$ (%)
Q1	0.10
Q2/Q4	0.00
Dipole	0.05
Levchuk / Radiative Corrections	0.04
Holding Field Alignment	0.03
Lead Block Bleedover	0.04
Phi Acceptance	0.01
Monte Carlo Statistics	0.08
Total	0.16

Table 4.14: Summary of Møller polarimetry systematics the CREX experiment.

Source	Value	$\delta P/P$ (%)
A_{zz}	0.75421	0.16
Foil Polarization	0.08005	0.57
Dead Time Correction	0.148%	0.15
Accidental Correction	0.205%	0.04
Charge Normalization	0.029%	0.01
Null Asymmetry (Cu Foil)	0.0%	0.22
PITA Variation	—	0.06
Spin Precession (dP/P)	—	0.04
High Current Extrapolation	—	0.50
Bleed through	—	0.18
Slit Dependence	—	0.10
Total		0.85

Chapter 5

PREX-II Experimental Results

This section will briefly review the results of the PREX-II experiment including an elementary review of important analysis corrections . At the time of writing results from the CREX experiment had yet to be formalized.

5.1 Scattering Angle Determination

5.1.1 Water Cell

Absolute angle determination is made by measuring the energy of electrons scattered off of the constituent hydrogen and oxygen atoms in the water cell target—this is referred to as a ‘pointing’ measurement. A sample of the data used for this calibration is shown in fig. 5.1. The elastic scattering peaks in the data are fit with a Gaussian curve in order to determine the mean values. These mean values E'_O and E'_H along with the masses of scattering nuclei m_O and m_H and beam energy E are then used to determine the scattering angle θ utilizing eq. (5.1).

$$\Delta E' \propto E'_O - E'_H = E \left(\frac{1}{1 + \frac{2E \sin^2(\frac{\theta}{2})}{m_O}} - \frac{1}{1 + \frac{2E \sin^2(\frac{\theta}{2})}{m_H}} \right) \quad (5.1)$$

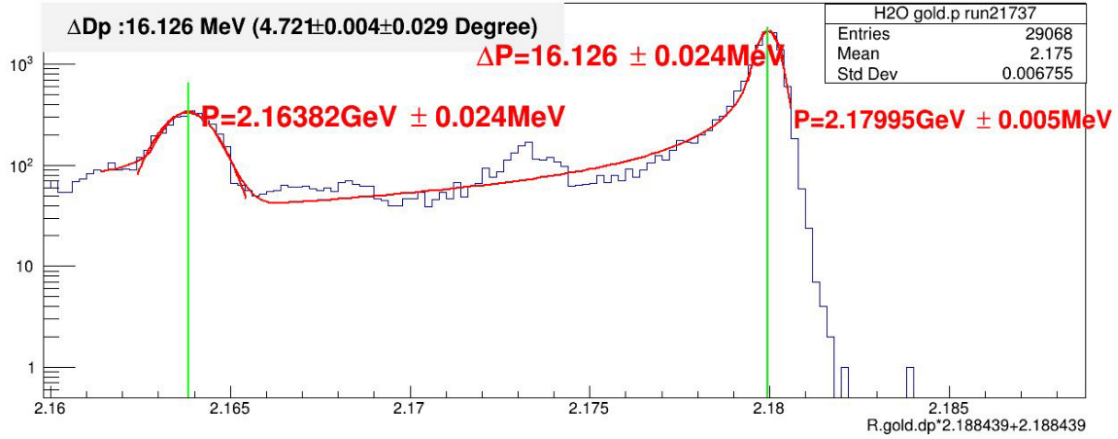


Figure 5.1: Example of data taken on the watercell target during CREX (RHRS arm data shown). Hydrogen scattering peak marked on left at $P = 2.163(24)$ GeV and Oxygen marked on right at $P = 2.179(5)$ GeV. Difference between scattering peaks is 16.126(24) MeV [Image courtesy of Siyu Jian [76]]

5.1.2 Sieve Calibration

Uncertainties on the scattering angles are constrained by using data taken with the sieve discussed in section 2.3.2 and shown in fig. 2.9. Since the sieve is placed before any magnetic elements of the HRS spectrometer scattered electron trajectories from the target to the sieve are straight lines. Reconstruction of vertex angles and positions from the HRS VDC focal plane data is achieved through a transport transformation matrix; both position and angles are reconstructed from this data. A sample of reconstructed sieve data vs. simulated expectations is shown in fig. 5.2. Data is taken at multiple beam-on-target positions. Differences in the reconstruction versus simulation expectations are then used to place a systematic on the angular reconstruction.

5.1.3 Central Angle Results

Results from the water cell momentum measurements and the sieve reconstructions are combined to produce a central angle measurement and associated uncertainty. The average scattering angle was $4.67^\circ \pm 0.02^\circ$ for the Left HRS and $4.71^\circ \pm 0.02^\circ$ for the Right HRS [75].

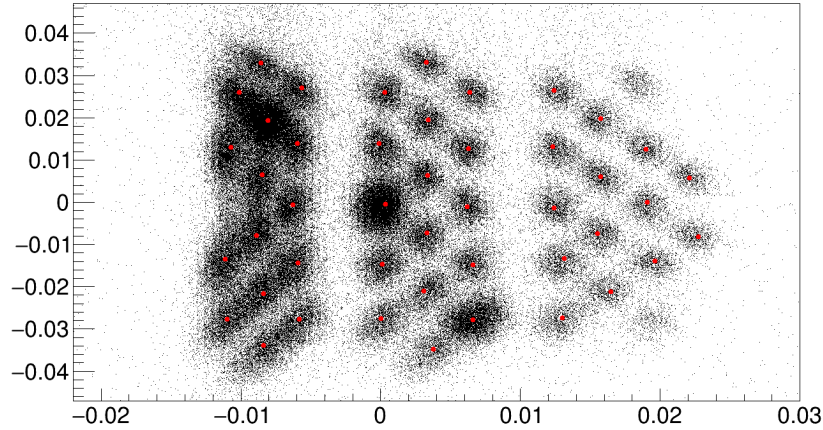


Figure 5.2: Sample data of sieve data angular reconstruction of θ_{targ} vs. ϕ_{targ} [black] vs. simulation expectations [red]. Axes values shown are deviations from expected central angles.

5.2 Q^2 measurements

The precise measurement of Q^2 is a critical measurement since scattering cross sections and atomic form factors are a function of it. The Q^2 for a scatter where E is the pre-scatter energy E' is the post-scatter energy and θ is the scattering angle is given by

$$Q^2 = 2EE'(\sin^2 \frac{\theta}{2}). \quad (5.2)$$

Special Q^2 measurement runs are performed, as the VDCs cannot handle high detection rates, to obtain data; Q^2 was calculated from each of these runs for both the LHRS and RHRS. Since the Q^2 measurement at the HRS VDC focal planes contain the physical effects of post-scatter energy losses additional corrections must be made to these Q_{VDC}^2 must be A Q_{vertex}^2 reconstruction utilizes simulation in order to account for radiative and scattering energy losses which result in minor corrections to Q_{VDC}^2 . Final results for Q^2 measurements gave an $\langle Q^2 \rangle = 0.00616 \pm 0.0004 \text{ GeV}^2$ averaged over the total acceptance [76]. Total systematic uncertainty contributed to the A_{PV} measurement from the angle determination is 3.5 ppb.

5.3 Raw Detector Asymmetry

The raw detector parity-violating asymmetry measurement A_{raw} is calculated from the integrated helicity data on a quartet-by-quartet or octet-by-octet basis. Similar to the way that charge corrections are handled with the Møller asymmetry data the integrated raw parity-violating asymmetry data is normalized to integrated BCM readings. This normalization corrects the parity-violating asymmetry for the charge asymmetry. The PREX-II A_{raw} was 431.64 ppb. This detector measurement A_{raw} contains false asymmetry information which must be subtracted in order to come up with a corrected parity-violating asymmetry.

5.4 Beam Asymmetry Correction

False asymmetries due to helicity-correlated beam fluctuations A_{beam} must be subtracted out from A_{raw} . Beam modulation hardware was described in section 2.2.6. The parity-violating asymmetry measured by the detectors is sensitive to beam parameters; changes in position, angle and energy can affect the number of scattered electrons which reach the detectors and contribute to false asymmetries. These false asymmetries must be well understood and taken into account.

PREX-II combined a regression analysis of measured natural beam motion and data from artificially induced beam orbit and energy modifications made by the beam modulation system described in section 2.2.6. Beam modulation data was used to constrain the regression analysis of natural beam motion using the method of Lagrange multipliers. The resulting correction from the Lagrange multiplier method was consistent with both the individual results of the regression and beam modulation. A_{beam} was determined to be -60.38 ± 2.5 ppb [77].

5.5 Beam Polarization Measurement

Beam polarization measurements were provided by Møller polarimetry for the PREX-II experiment. Final polarizations with statistical errors were outlined in section 4.7.1, the systematic error for PREX-II polarimetry was outlined in section 4.8.3, and are summarized in table 5.1. The final weighted arithmetic mean of the Møller polarization results, weighted by the error in A_{PV} for each HWP state, was $89.67\% \pm 0.1\%$ (rel stat) $\pm 0.89\%$ (rel syst). The beam polarization contributed a correction of 56.8 ppb along with a systematic uncertainty of 5.2 ppb. Systematic uncertainty from polarization is the largest systematic of the experiment.

Table 5.1: Summary table of polarization measurements provided to the PREX-II experiment [errors shown are absolute (Polarization %)].

HWP State	Polarization [%]	Stat Error [%]	Syst Error [%]
HWP In	89.10	± 0.09	± 0.80
HWP Out	90.31	± 0.09	± 0.80

5.6 Transverse Asymmetry Measurement

The electron beam provided by CEBAF would ideally be 100% polarized in the longitudinal direction; this, however, is not the case and there may be a small transverse polarization which results in a scattering asymmetry sensitive to the plane of scatter angle ϕ . This transverse asymmetry, called the “beam normal single spin asymmetry” A_n , is a parity-conserving asymmetry and is therefore a systematic error concern since it can contribute a false asymmetry to the raw parity-violating asymmetry results. This transverse asymmetry for ^{208}Pb is numerically computed to be on the order of 10^{-7} [78] and so must be measured and accounted for.

In the Born approximation with a single photon exchange this asymmetry is equal to

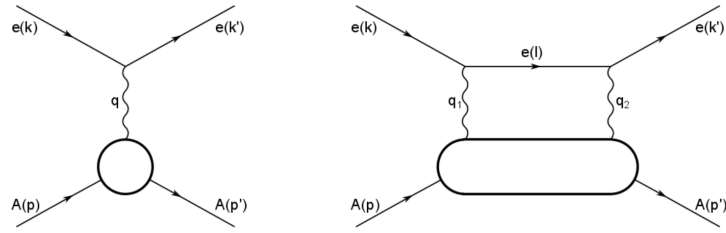


Figure 5.3: Transverse Scattering Diagrams. Left-panel: Single photon exchange between the electron and target nucleus; Right-panel: A double-photon exchange with the target nucleus. Figure taken from [79].

zero. The rarer interaction involving a two-photon exchange which is shown in fig. 5.3 is responsible for the asymmetry. This asymmetry is sensitive to the plane of scatter and scales with target charge Z and beam energy E_e .

$$A_n = \frac{\sigma_{\uparrow} - \sigma_{\downarrow}}{\sigma_{\uparrow} + \sigma_{\downarrow}} \approx 0 + \frac{2\text{Im}(T_{2\gamma} \cdot T_{1\gamma}^*)}{|T_{1\gamma}|^2} \propto Z\alpha \frac{m_e}{E_e} \quad (5.3)$$

During the course of the PREX-II and CREX experiments special transverse polarization data runs were taken. A vertical Wien filter is used at the accelerator to accomplish this task. These data runs were taken for ^{12}C , ^{208}Pb , ^{40}Ca , and ^{48}Ca . These measured parity-conserving transverse asymmetry measurements go through the same analysis and correction process. For PREX-II A_n measurements contributed a correction of 0ppb but contributed 0.26ppb in systematic uncertainty.

5.7 Target Diamond Coating

In order to assist in better heat dissipation for the ^{208}Pb targets the foils were covered in a diamond coating on each side. There is no way of knowing which detected scatter came from ^{208}Pb foil or the ^{12}C so, in reality, the raw measured asymmetry is a sum of the asymmetry of the ^{208}Pb foil and the asymmetry of the ^{12}C diamond coating. As such, particular effort must be made to subtract out the portion of the asymmetry due to carbon pollution. Similar to asymmetry corrections made in the Møller analysis an analytic description of how to correct for this can be derived and is shown in eqs. (5.4)

and (5.5) where A represents asymmetry contributions specified by the superscripts, N are measured rates specified by the superscripts, f are fractional rates specified by the superscripts (both of which must add to unity), and subscripts (where present) represent helicity states.

$$\begin{aligned} A^{\text{meas}} &= \frac{N_1 - N_0}{N_1 + N_0} = \frac{(N_1^{208\text{Pb}} + N_1^{12\text{c}}) - (N_0^{208\text{Pb}} + N_0^{12\text{c}})}{(N_1^{208\text{Pb}} + N_1^{12\text{c}}) + (N_0^{208\text{Pb}} + N_0^{12\text{c}})} \\ &= A^{208\text{Pb}} f^{208\text{Pb}} + A^{12\text{c}} f^{12\text{c}} \end{aligned} \quad (5.4)$$

$$A^{208\text{Pb}} = \frac{A^{\text{meas}} - A^{12\text{c}} f^{12\text{c}}}{1 - f^{12\text{c}}} \quad (5.5)$$

Hence, a correction for the asymmetry from the diamond foil coatings can be calculated from the fractional rate due to the ^{12}C diamond coating and scattering asymmetry of carbon. The carbon asymmetry comes from the formula

$$A = \frac{G_F Q^2}{\pi\alpha\sqrt{2}\sin^2\theta_W}. \quad (5.6)$$

The fractional scattering rate due to the carbon coating was derived from simulations under the conservative limit that the thickness of the Pb foils and diamond coatings was understood to within 5%. The Q^2 measurement for ^{12}C was $Q^2 = 0.0063\text{GeV}^2$. The A_{PV} correction for the background from the diamond coating on the ^{208}Pb foils was 0.7 ppb with a systematic uncertainty of 1.4 ppb [80].

5.8 Acceptance Function

The acceptance function $\epsilon(\theta)$ is the probability that an electron with scattering angle θ will make it to the detector.

$$\langle A_{PV} \rangle = \frac{\int d\theta \sin\theta A(\theta) \frac{d\sigma}{d\omega} \epsilon(\theta)}{\int d\theta \sin\theta \frac{d\sigma}{d\omega} \epsilon(\theta)} \quad (5.7)$$

The acceptance function does not contribute any correction to the measurement but does place a systematic uncertainty on the measurement through the analysis of sensitivities to changes in the Monte Carlo; this is similar to the how calculated uncertainties on the analyzing power for the Møller polarimeter contribute to an overall systematic uncertainty for the polarization measurement. The PREX-II acceptance was modeled in a Geant4 application and $\epsilon(\theta)$ is then used for A_{PV} predictions utilizing different models. In this way the acceptance function provides a comparison of the experimental measurement to the theoretical predictions. The uncertainty in the modeling of $\epsilon(\theta)$ contributed a

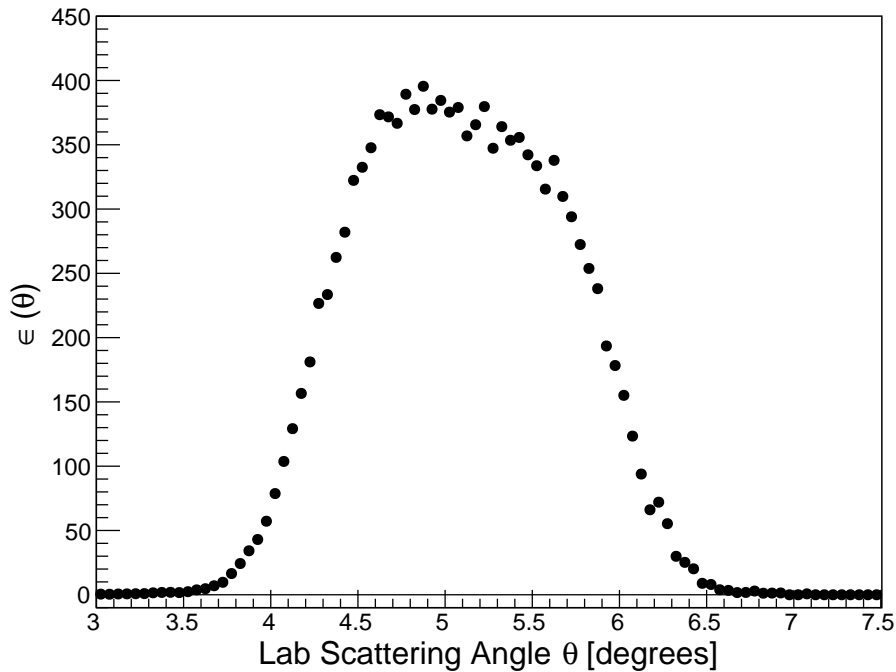


Figure 5.4: PREX-II acceptance function $\epsilon(\theta)$. Figure taken from supplemental materials of [75]

systematic of 2.9 ppb.

5.9 A_{PV} Corrections Summary

Corrections to A_{PV} are summarized in table 5.2. Additional corrections not reviewed were detector non-linearities between the four PREX-II integrating detectors and the BCM monitors which contributed a systematic uncertainty of 2.7 ppb and minor rescattering and inelastic scattering contributions both of which contributed 0.1 ppb in systematic

uncertainty.

Table 5.2: Summary of corrections to the asymmetry along with systematic uncertainties. Total uncertainty in beam polarization is the largest source of error at 5.2ppb. Adapted from [75].

Correction	Absolute [ppb]	Error [ppb]	Relative [%]	Error [%]
Beam asymmetry	-60.4	± 3.0	11.0	± 0.5
Charge Correction	20.7	± 0.2	3.8	± 0.0
Beam polarization	56.8	± 5.2	10.3	± 1.0
Target diamond	0.7	± 1.4	0.1	± 0.3
Spectrometer rescattering	0.0	± 0.1	0.0	± 0.0
Inelastic contributions	0.0	± 0.1	0.0	± 0.0
Transverse asymmetry	0.0	± 0.3	0.0	± 0.1
Detector non-linearities	0.0	± 2.7	0.0	± 0.5
Angle determination	0.0	± 3.5	0.0	± 0.6
Acceptance function	0.0	± 2.9	0.0	± 0.5
Total Correction	17.7	± 8.2	3.2	± 1.5

5.10 PREX-II Experimental Result

The PREX-II experiment amassed a total of 114 Coulombs of charge and a total of approximately 50 million helicity patterns. In order to obtain the corrected asymmetry A_{corr} the beam asymmetry corrections A_{beam} and transverse asymmetry correction A_n (which was 0) must be subtracted from the charge corrected raw asymmetry A_{raw} and corrections for backgrounds must be removed as prescribed in eq. (5.8).

$$A_{PV}^{meas} = \frac{1}{P_{beam}} \frac{A_{corr} - P_{beam} \sum_i A_i f_i}{1 - \sum_i f_i} \quad (5.8)$$

This yields the final parity-violating asymmetry $A_{PV} = 550 \pm 16(\text{stat}) \pm 8(\text{syst})$ ppb.

From this parity-violating asymmetry it is then possible, as previously outlined, to extract measurements for $F_W(Q^2)$, ρ_W^0 and ρ^0 , R_W , and R_{np} . The value of the neutral weak form factor corresponding to a $Q^2 = 0.00616 \text{ GeV}^2$ is

$$F_W^{208\text{Pb}}(Q^2 = 0.00616\text{GeV}^2) = 0.368 \pm 0.013 (\text{exp}) \pm 8 (\text{theo})$$

The extracted interior weak density

$$\rho_W^0 = -0.0798 \pm 0.0038 \text{ (exp)} \pm 0.012 \text{ (theo)} \text{ fm}^{-3}$$

The extracted weak radius

$$R_W^{208\text{Pb}} = 5.795 \pm 0.082 \text{ (exp)} \pm 0.013 \text{ (theo)} \text{ fm}$$

Total interior baryon density

$$\rho_b^0 = 0.1428 \pm 0.0040 \text{ (exp \& theo)} \text{ fm}^{-3}$$

Yielding a neutron skin of

$$R_{np}^{208\text{Pb}} = 0.278 \pm 0.078 \text{ (exp)} \pm 0.012 \text{ (theo)} \text{ fm.}$$

5.11 Experimental Impact on Physics

PREX-II results were in large agreement with the original PREX results. The combined PREX-II and PREX results, weighted by error, yield a neutron skin for ^{208}Pb of 0.283 ± 0.071 fm [75]. The slope of the symmetry energy L corresponding to the measured neutron skin is 106 ± 37 MeV [81]. The PREX-II experimental results yield a neutron skin which is thicker than expected and by correlation in the nuclear EOS being one that represents a stiffer neutron pressure.

The PREX-II results derived from the measurement of A_{PV} are in tension with an alternative method of calculation which relates the electric dipole polarizability α_D to the nuclear EOS—a method of which is described in [82]. Measurements of α_D suggest a softer neutron pressure and a thinner neutron skin. The implications of this tension, and lack of current explanation, are reviewed in detail in [83].

The PREX-II experimental results are also in some tension with measurements of neutron star radii made by NASA's Neutron Star Interior Composition Explorer [NICER] [84] mission designed to measure x-ray emissions from compact sources (such as neutron stars) with high timing precision. Data taken by NICER of pulsar PSR J0030+0451 provide a model-dependent equatorial radius measurement along with a mass measurement [85]. These radius and mass measurements given from NICER data analysis provide constraints on the nuclear EOS which are consistent with PREX-II within a region of error and could potentially be subject to additional theoretical exploration of interior neutron star densities in order to further investigate tension [81].

The tension of the results of various methods seems to suggest the need for the further refinement of measurements through greater statistical precision and lower systematic uncertainties in order to provide unambiguous results which may then require better theoretical explanation.

Chapter 6

Discussion

Noteworthy improvements were made towards high-precision Møller polarimetry during the PREX-II and CREX experiments and there is remaining work required in order to achieve future experimental goals. Additionally, the results of the PREX-II experiment and subsequent tensions with other measurements opens the door to new thought-provoking questions which will require more experimental data to help paint a more complete and more finely-detailed picture. Below are some concluding remarks.

6.1 Møller Polarimetry

There was particular care made in the controlling of systematic uncertainties in order to exceed the proposed 1.1% systematics goals. The effort undertaken to develop a meticulous understanding of the Møller polarimeter along with the conservative systematics scrutiny for the PREX-II and CREX experiments, in some respects, was done to push the envelope towards the high-precision Møller polarimetry that will be required in the future. Planned PVES experiments such as the Measurement Of a Lepton Lepton Electroweak Reaction (MOLLER) [86]—which will be measuring the weak charge of the electron Q_W^e by measuring the A_{PV} of longitudinally-polarized electrons off of liquid hydrogen target—and future PVDIS experiments with the planned SoLID spectrometer [87] have

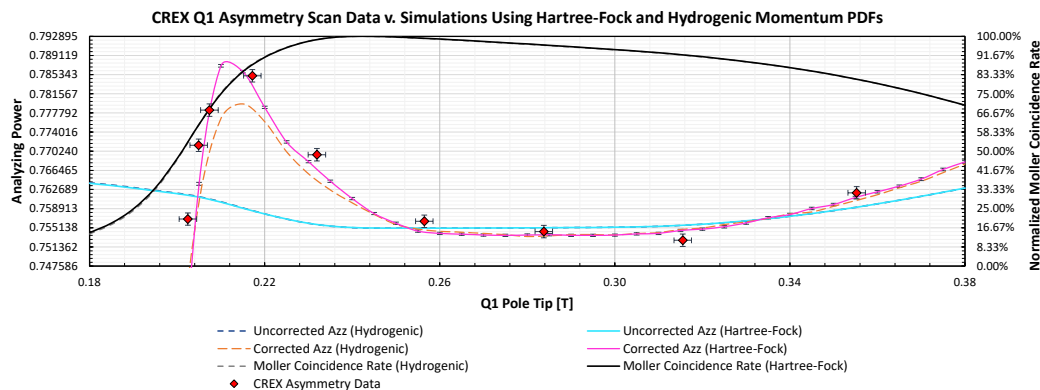


Figure 6.1: Comparison of CREX asymmetry data against simulation results from MolPol using the generally used modified hydrogen wavefunction model (labeled ‘Hydrogenic’ in the graphic above) to generate the momentum spectrum for the bound iron electrons and the momentum spectrum for the bulk-iron electrons generated from Hartree-Fock calculations.

strict polarimetry budgets of 0.45% and 0.4% respectively. As such, our developed methods and keen focus on keeping a tight hand on systematics is paving the way towards future high-precision polarimetry for PVES experiments in Jefferson Lab’s Hall-A.

The following few areas are those which are undergoing improvement, need improvement or which have solutions that simply need to be implemented in the future:

Analyzing Power Levchuk Modeling

The Møller analyzing power systematics for PREX-II table 4.11 and CREX table 4.11 and represent a significant improvement in the understanding of the polarimeter and great progress towards high-precision polarimetry that will be required for future experiments. Improvements on the modeling of the Levchuk Effect section 3.2.1 by utilizing Hartree-Fock generated momentum distributions of the bulk iron electrons. When compared to the CREX asymmetry data taken over a wide spread of magnet detuning the Hartree-Fock modeling shows a dramatic improvement over the long-used Modified Hydrogen modeling.

Bleed through

Bleed through provided an unwelcome 0.2% systematic during the CREX as Hall-C was running a concurrent experiment at a $30\mu\text{A}$ current. Since the polarization of Hall C was

of opposite sign this amplified the issue by a factor of two. In theory, the solution to the bleed through issue requires negotiation and cooperation between Hall-A and Hall-C in the scheduling of Møller polarimetry measurements.

High Current Extrapolation

This is perhaps the most challenging systematic to be studied and is more of an “unsettled concern”. Previous studies performed in Hall-C, data shown in fig. 4.37, have set a maximum limit on this. For future parity-violating experiment requirements a systematic of 0.5% isn’t acceptable within the required systematics budget. In order to settle this concern additional studies, perhaps a repeat of the 2007 Hall-C, will be required.

6.2 Neutron Skin Measurements

The PREX-II experiment results indicate a thicker-than-expected neutron skin; as such, there exists some tension between the PREX-II results and the extrapolated radii of neutron stars (which the PREX-II result would predict under prevailing theoretical assumptions about the extension of the nuclear EOS from nuclei at nuclear saturation all the way up to astrophysical objects). In order to make sense of these tensions additional data will be needed.

On the experimental nuclear physics side, unfortunately, the HRS spectrometers which made the PREX/CREX measurements possible in Jefferson Lab’s Hall A have been decommissioned as the experimental hall transitions towards newer experiments and so the possibility of future neutron skin measurements has evanesced. The next available opportunity to measure the neutron skin of ^{208}Pb will be at the Mainz Energy Recovery Superconducting Accelerator (MESA) which is expected to begin accelerator operations in 2023. One of the experimental units that will be located at the MESA facility is P2 [88]—a PVES-type experiment, which aims to measure $\sin^2 \theta_W$ to a precision of 0.15%. The P2 spectrometer opens the door for new high-precision PVES experiments and within the scope of the P2 experiment is the Mainz Radius Experiment (MREX) which aims

to measure the neutron skin of ^{208}Pb to a precision of 0.52%. The additional neutron skin measurement of ^{208}Pb by MREX will reinforce and further refine the result of the PREX-II experiment.

Chapter 7

GEM Alignment for SoLID

The SoLID spectrometer [89] proposed at the Thomas Jefferson National Accelerator Facility will provide a large-acceptance and high luminosity facility for electron scattering. Experiments include SIDIS, measurement of J/ψ production near threshold, and parity violation in deep inelastic scattering (PVDIS). The PVDIS experiment has a special requirement in the precision of the alignment of tracking GEM chambers in order to provide a precise measurement of the average Q^2 of the events. The goal of the PVDIS experiment is to measure the parity violating asymmetry A_{PV} with a polarized beam and unpolarized target. The experiment will measure A_{PV} over a wide kinematic range with a precision of 0.6%, will search for physics beyond the standard model above the 10 TeV level, study charge symmetry violation at the quark level, search for quark-quark correlations, and with a proton target, can measure the ratio of structure functions for up and down quarks without recourse to nuclear targets. This chapter will discuss work done in developing a method for the radial alignment of GEM detectors for the SoLID spectrometer planned PVDIS experiment [87].

7.1 SoLID Spectrometer

7.1.1 Description

The SoLID spectrometer uses a 1.5 T solenoidal magnet formerly used for the CLEO experiment at Cornell. Its design is such that the spectrometer can achieve both a large acceptance and high luminosity. There are two configurations, one for the SIDIS and J/ψ experiments and one for PVDIS which is shown in fig. 7.1. The momentum of scattered electrons and hadrons is measured by a series of five GEM detectors. There are two Shashlik electromagnetic calorimeters—one large angle calorimeter located near center of the magnet and one forward angle calorimeter located towards the end. The calorimeters are designed to identify scattered electrons over a wide angular range. Hadrons striking the forward calorimeter are identified by two Cerenkov detectors each with different thresholds.

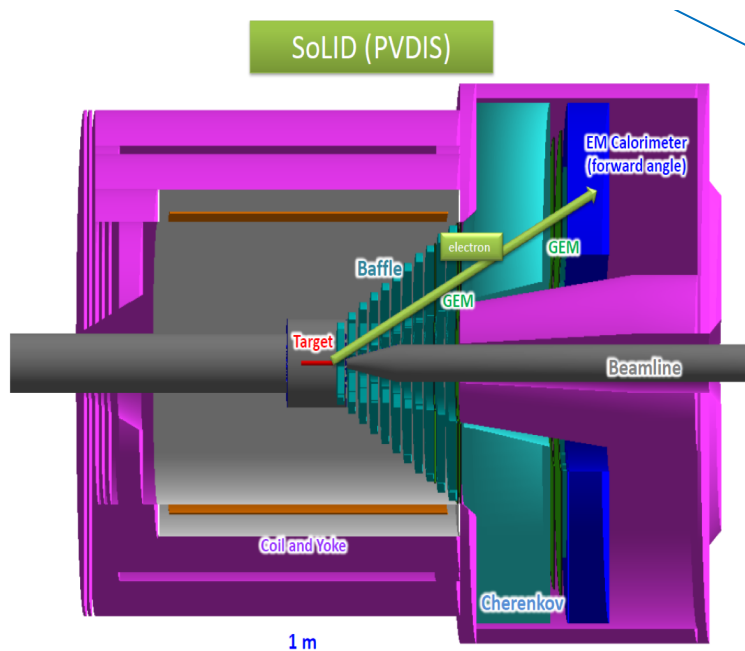


Figure 7.1: SoLID detector configuration for the PVDIS experiment.

For the PVDIS configuration, the 0.5 m liquid deuterium target is located at the center of the magnet. A set of baffles has been designed to allow the clear passage of electrons in the desired kinematic range but are able block most photons, positive pions,

and low energy negative pions. The baffles divide the apparatus into 30 sectors. There is a Cherenkov counter located after the baffling and and Shashlik calorimeter at the end of the spectrometer both to assist with particle identification. The Cherenkov counter, is used to help identify electrons from among the copious pion background. Electrons with a scattering angle between 20° and 35° are detected by 5 GEM trackers—one of which is located within the baffling, two are at located at the end of the baffling before the Cherenkov counter, and the final two are located before the electrons enter the forward Shashlik calorimeter.

7.1.2 Gaseous Electron Multiplier Detectors

Gas Electron Multiplier [GEM] detectors provide high resolution measurements ($\approx 75\mu\text{m}$) of particle trajectories and can accommodate multi MHz rates. A general mock-up and basic description of how a GEM functions are shown in fig. 7.2. In order to take full advantage of the high resolution which can be provided, the GEMs themselves must be aligned to a high precision.

7.1.3 Measurement of the Momentum of the Scattered Electron

The measured asymmetry A_{PV} is proportional to the momentum transfer squared $Q^2 = 4EE' \sin^2 \theta/2$, where in the laboratory frame E is the incident beam energy, E' the energy of the scattered electron, and θ is the scattering angle. In order for the systematic error in the average value of Q^2 below $\sim 0.1\%$, the systematic error in the average of each of these quantities must be below that level. The subject of this paper is how to achieve the required precision on E' , which is the most difficult of the quantities to measure and places the most stringent requirement on the alignment.

The momentum of the scattered electron is measured by measuring the effect of the magnetic field of the solenoid on the trajectory as measured by the GEM's. This is done not by directly measuring the curvature of the track, but rather by fact that the projection

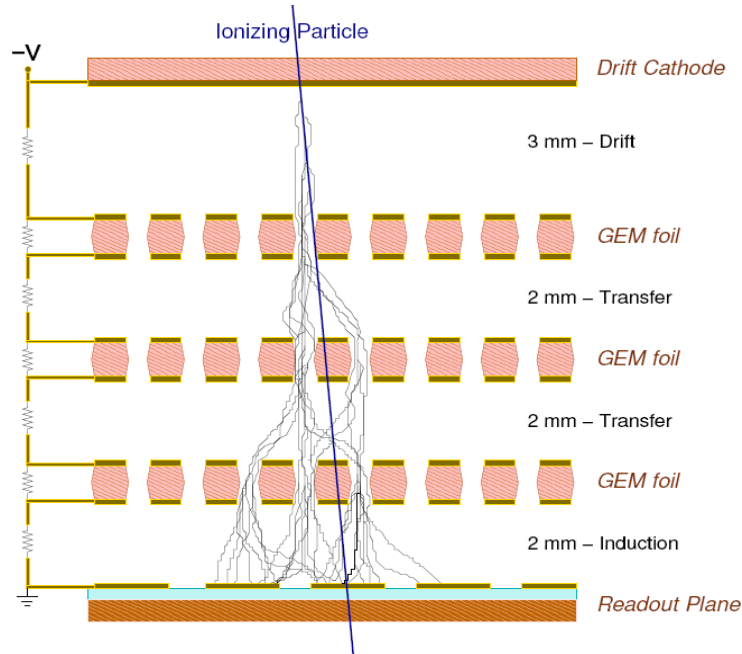


Figure 7.2: Electron cascade within a GEM detector. Between the drift and charge collection cathodes are thin polymer foils which are metal coated on both sides with a high density of holes drilled into the foil. The application of a large potential applied to the foil creates electric field lines such that ionized electrons are directed through the drilled holes and acquire sufficient energy while traveling in the field to cause additional ionizing collisions within the gas causing an electron cascade directed towards charge collection wires. The more numerous the internal GEM foils the larger the cascade. Image adapted from [90]

of the track at the end of the spectrometer back to the target misses the trajectory of the beam by a distance d . For typical tracks, $d \approx 10$ cm. The GEM's must be aligned with sufficient accuracy so that the systematic error in d is less than $100\mu\text{m}$.

7.2 GEM Calibration Method

In order to align the GEM's to the required precision, we plan to take calibration runs with a slightly modified configuration of the apparatus. The beam passes through a thin carbon target (simulation work utilized a 1mm thick target), producing a point source of photons. The target is located slightly upstream of the front of the normal target, which is removed from the beam. There is a small solid angle acceptance for photons produced at this position to pass through the baffles and reach the GEM's.

A set of remotely movable pinhole collimators is added which are designed to produce

pencil beams of photons. There is one collimator for each GEM sector. Signals from these photons interacting in the various GEM's then lie on a straight line pointing at the target. The exact direction of this line not critical, so the alignment of the pinhole is not critical.

The requirements for the configuration are:

- The photons passing through the hole in each collimator must produce a narrow peak in the GEM's, on the order of 1 mm, that can be centered to $\sim 100\mu$.
- The background under the peak must be small.
- The size and mass of the collimators must be as small as possible.

The photons are not directly detected by the GEM's; rather it is the electrons produced by interactions of the photons that are detected. As discussed in the next two sections, it turns out that a clean peak is produced in the GEM's by low-energy electrons produced by the photoelectric effect.

7.3 Sources of Photons and their Energy Spectra

Bremsstrahlung photons from the primary beam are forward peaked and are negligible at the angles relevant for the SoLID spectrometer. Instead, there are two other major sources of low energy photons in the GEM's:

1. Compton scattering of soft bremsstrahlung of the beam electrons. This only occurs for low energy photons; for $E_\gamma \gg m_e$, the scattering angles are again too small.
2. Forward bremsstrahlung from low energy Møller electrons pointing at the GEM's.

The spectra are shown in fig. 7.3. On the log-log plot, the typical $1/E$ spectrum characteristic of bremsstrahlung radiation is a flat line. The low energy cutoff occurs because low energy photons cannot escape the target or are absorbed in the air. The spectrum of Compton photons is reduced at low energies due to the Landau-Pomeranchuk

–Migdal [LPM] effect [91, 92]. The bremsstrahlung which comes from low energy Møller electrons are not suppressed by the LPM effect and those dominate at the lowest photon energies. It is these photons, from the low energy Møller scatters, which the are the most important for our calibration.

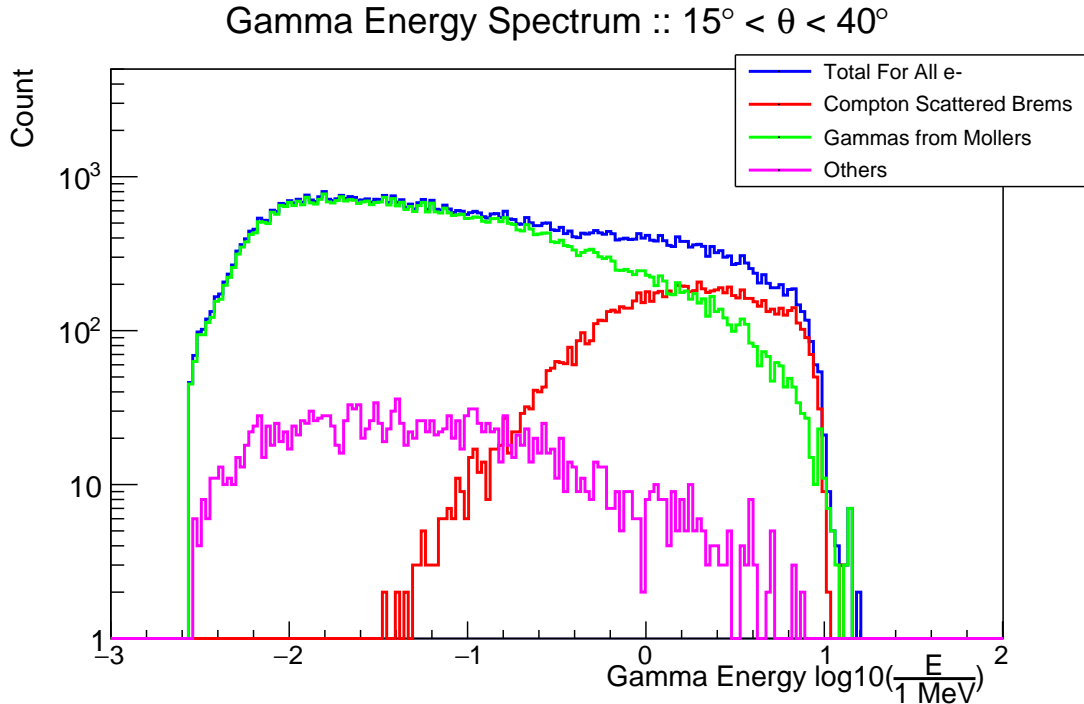


Figure 7.3: Gamma spectrum from 11GeV beam on 1mm thick carbon target detected between 15° and 40° off the beam axis. Compton scattered beam bremsstrahlung, bremsstrahlung from Møller scattered electrons are shown as well as a small contribution of gammas labeled “others” from secondary interactions.

As photons pass through the GEMs in the apparatus additional attenuation of the low energy part of the photon spectrum does occur as shown in fig. 7.4. However, we will show that even for the last GEM, there are sufficient low energy photons available for the calibration.

7.4 Signals in the GEM’s from the Photons

There are two dominant processes by which low energy photons generate signals in the GEM’s

1. Photoelectric effect.

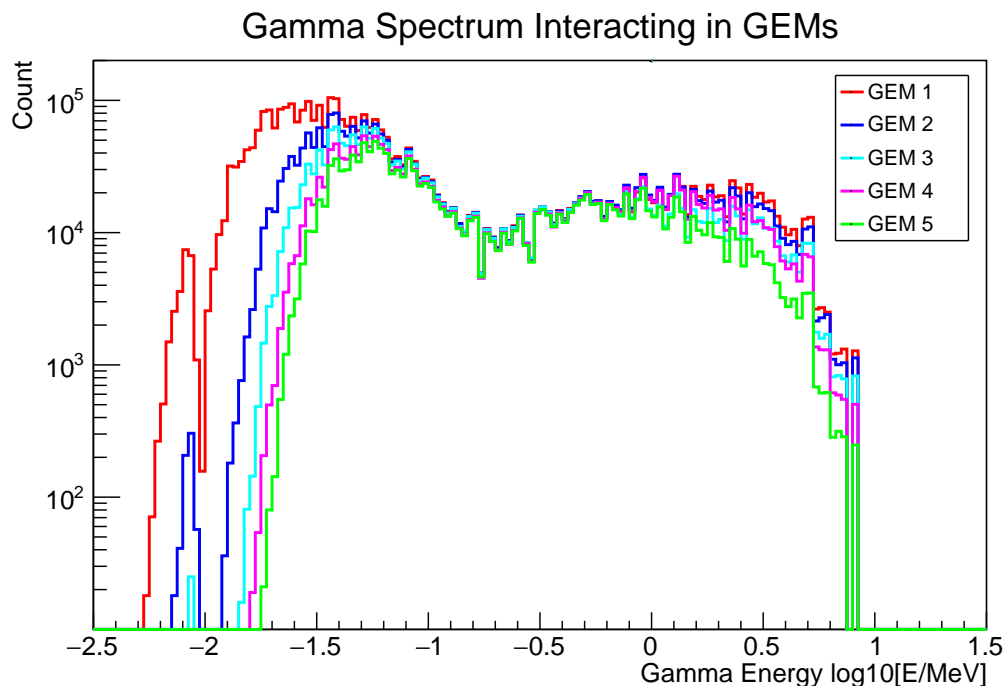


Figure 7.4: Spectrum of gammas which resulted in an interaction in GEMs 1 through 5.

2. Compton scattering

Minimizing-ionizing particles [MIPs] deposit about 1 KeV of energy corresponding to about 300 ion pairs; these are most often the result of Compton scatters that occur within device. The MIP's tend to scatter out roughly 2mm from the original point of interaction as shown in fig. 7.5. Some of the photoelectric effect signal comes from the K-edge of the Argon gas in the GEM, which is about 3 KeV, plus the energy deposited by the remaining low energy electron. For these events, most of the energy is deposited close to the point where the photon interacted, as shown in fig. 7.5. These highly localized signals are important for the calibration.

7.5 Spatial Distribution of Photons in a Pencil Beam

A narrow pencil beam was used to simulate the transverse distribution of the signals in the GEM's. The results are shown in fig. 7.6. Events from photons interacting in the gas in the GEM's are very near the incident photon. These are due to low energy photons

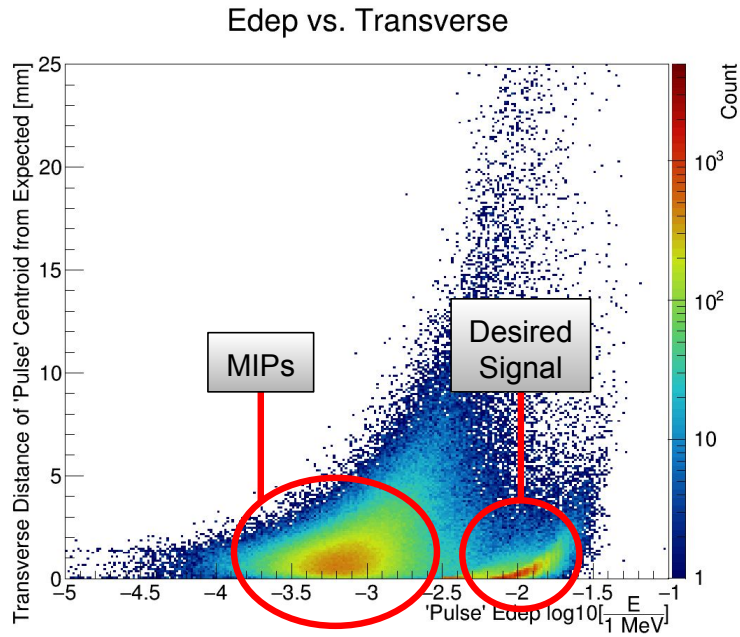


Figure 7.5: Pulse energy deposit vs distance of centroid of energy deposit from entrance point of photon on the GEM detector.

that deposit energy well above the MIP level by the photo-electric effect. Large signals near the photon pencil beam are also produced by photon interactions in the Cu layers on either side of the gap in the GEM. Electrons originating from the front metal cathode layer of the GEM detectors should also help contribute sizable signals for alignment.

7.6 Collimator Design

The collimators used in simulation were tungsten cylinders with a small hole in the center. However, with a small adjustment to the length, the collimators be constructed of lead rather than tungsten. The size of the aperture hold was a compromise to be large enough to provide enough signal yet small enough so that the signal region was small enough so that it could be centered accurately. In particular, there is no reason to have the hole smaller than the spread of the signals discussed in the previous section; this sets a reasonable limit for the minimum size of the collimating hole. The outer diameter of the cylinders was made as small as possible while still maintaining a region of sufficiently low background signal outside the central region. The cylinder had to be thick enough so that

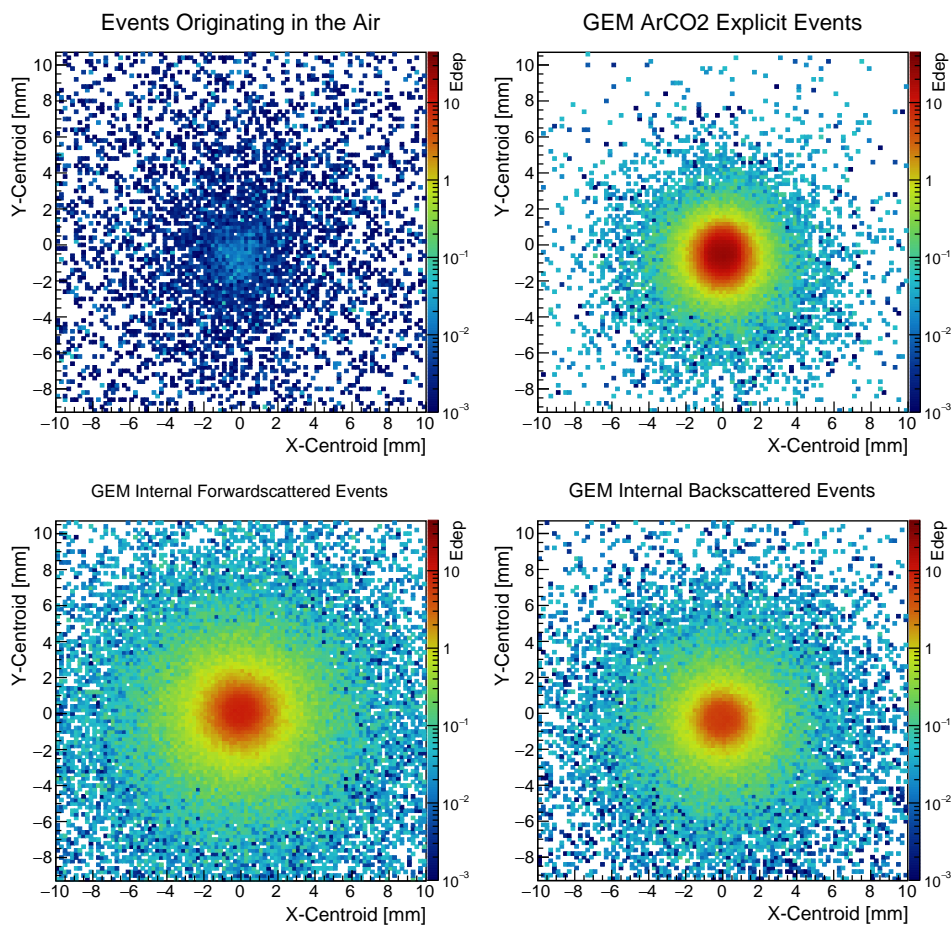


Figure 7.6: Spatial spread of energy deposits in GEM from thin pencil beam composed of spectrum shown in fig. 7.3. Energy deposits are divided into four categories—backgrounds resulting from events which originated in the air in front of the GEM, events which occur within the ArCO₂ gas and forward scattered events from the copper anode and backscattered events from the first internal GEM foil.

it produced a shadow significant enough such that the differentiation between signal and background was easily recognizable. High energy photons showered in Collimators which were too thin and increased the background rates underneath the signal that we were looking for. Toy simulations using plates of lead with a 1mm aperture hole under a 4cm x 4cm beam of gammas were examined to determine optimal thickness. Sample results for lead with a thickness of 2cm and 6cm from these simulations are shown in figs. 7.7 and 7.8 respectively. Signal-to-background improved by an order of magnitude between 2cm Pb and 6cm Pb.

Minimization of the size of the collimators was important as they have to be light enough and small enough so that they could be mounted on simple pneumatic actuators.

Results using a tungsten collimator that is 8 mm in diameter, 3 cm thick, and with a 1 mm hole are shown in fig. 7.9.

A clean, narrow peak can be seen at the center of the distribution. This signal is ideal for aligning the chambers.

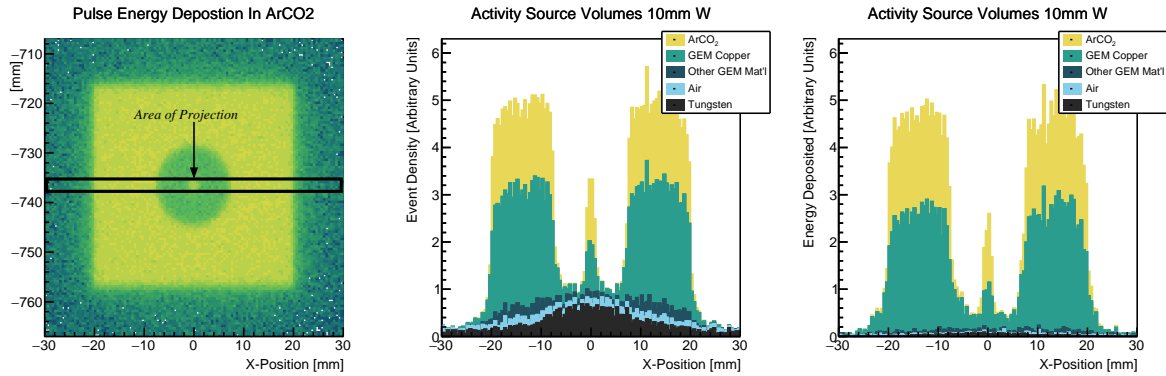


Figure 7.9: Signal and background energy densities from 4cm x 4cm square of incident gammas of spectrum shown in fig. 7.3 on 10mm radius W collimator which is 30mm thick with 1mm hole centered at origin. Left panel shows area of projection for center and right panel histograms. Center panel histogram shows event density along projection stacked by source volume for event. Right panel shows deposited energy in area of projection.

7.7 Results

The optimized cylinders were added to the geometry of the SoLID spectrometer. The GEANT-4 results for all five GEM chambers are given in figs. 7.10 and 7.11. The first is without the magnetic field and the second is with the magnetic field on. Clean signals that are ideal for the calibration are seen in each case. With the magnetic field off, scattered high energy electrons can also be used for the alignment and verify the effectiveness of the photon calibration. Any changes in the alignment when the field is turned on can then be detected by the photons.

Proper alignment of the GEM's and the minimization of the systematic error in the measurement of the radius of curvature of the scattered electrons traveling through the spectrometer will contribute greatly to the reduced systematics of calculating the Q^2 of the events.

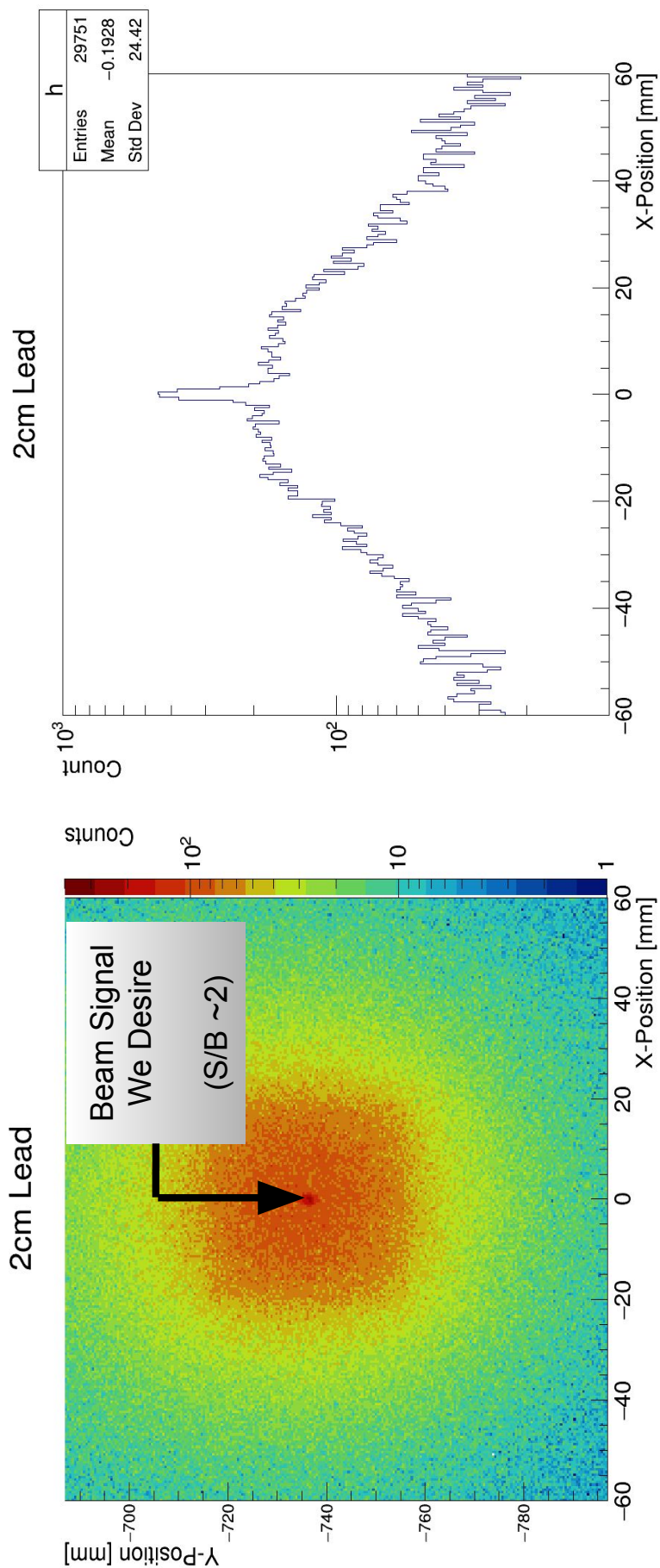


Figure 7.7: Square beam of gammas, 2cm x 2cm, incident on 2cm thick lead plate with 1mm hole centered at origin. Signal to background ratio ≈ 2 .

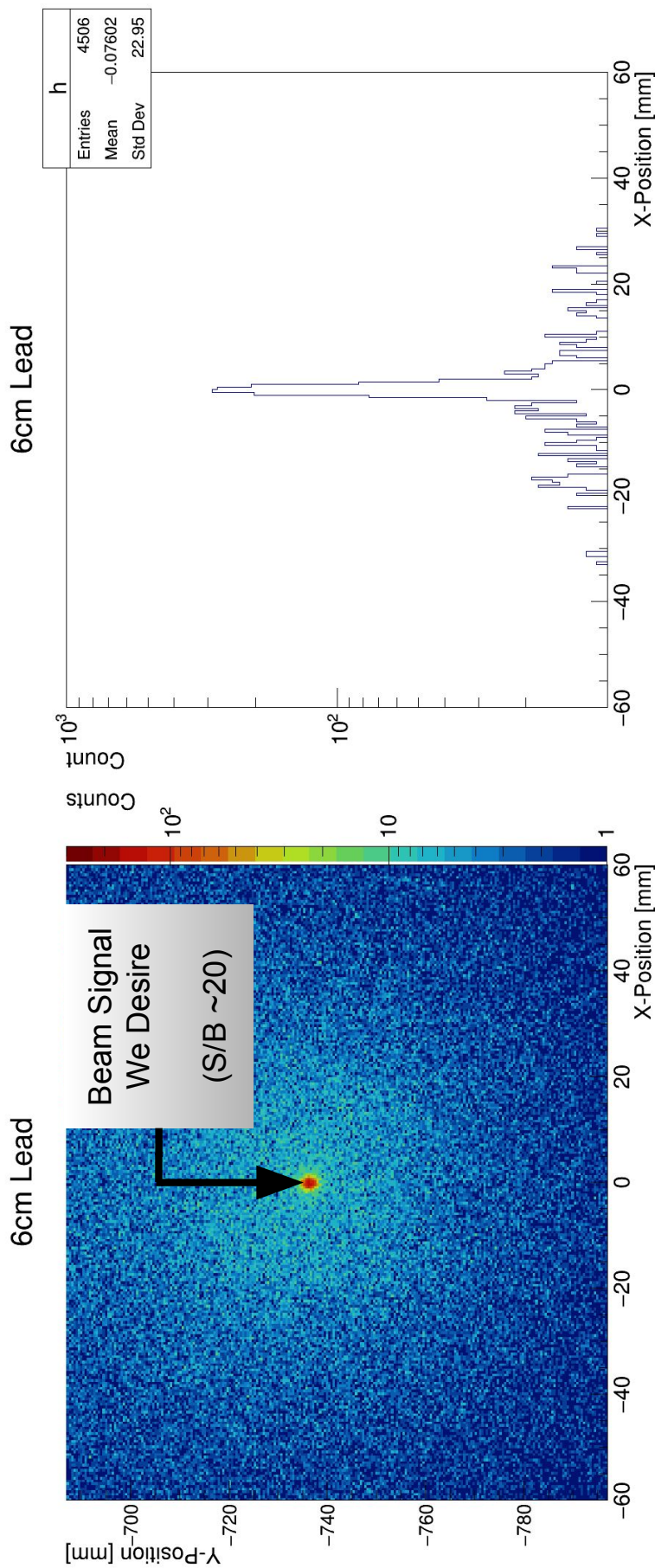


Figure 7.8: Square beam of gammas, 2cm x 2cm, incident on 6cm thick lead plate with 1mm hole centered at origin. Signal to background ratio ≈ 20 ; an order of magnitude improvement from 2cm thick lead plate.

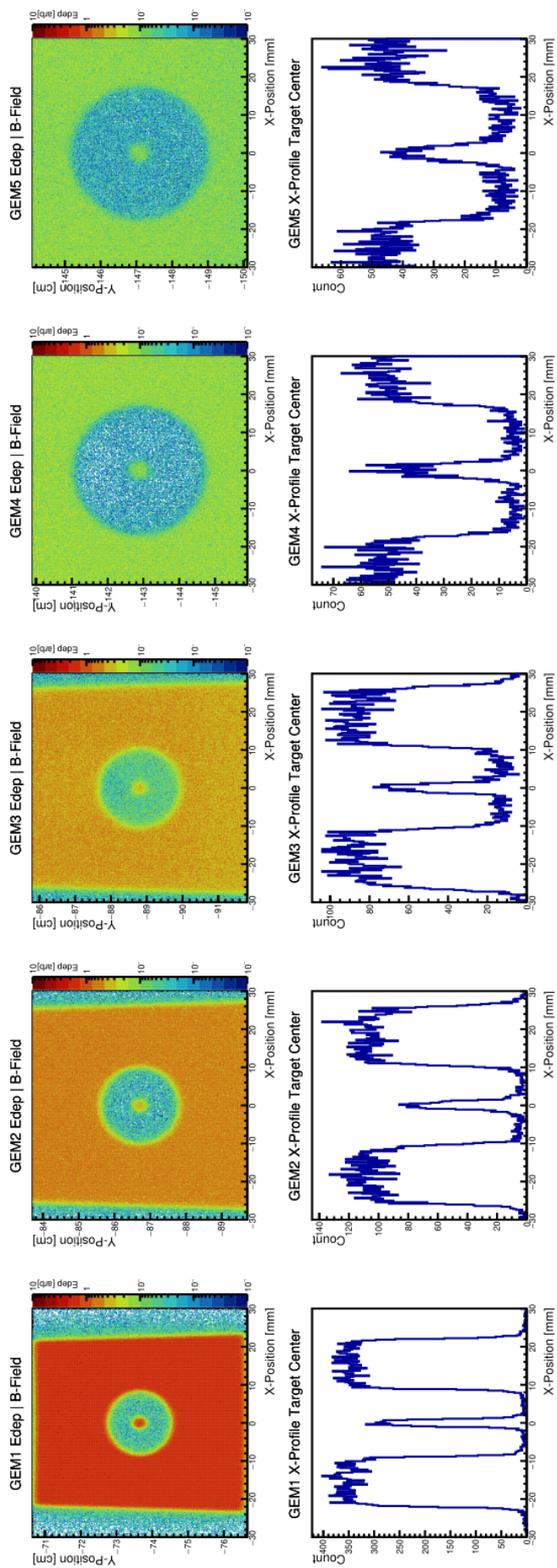


Figure 7.10: Energy deposition by gamma rays produced from beam on Carbon target in the five GEM detectors of the SoLID spectrometer in the PVDIS setup with magnetic field on. A rather clean signal is seen in each GEM.

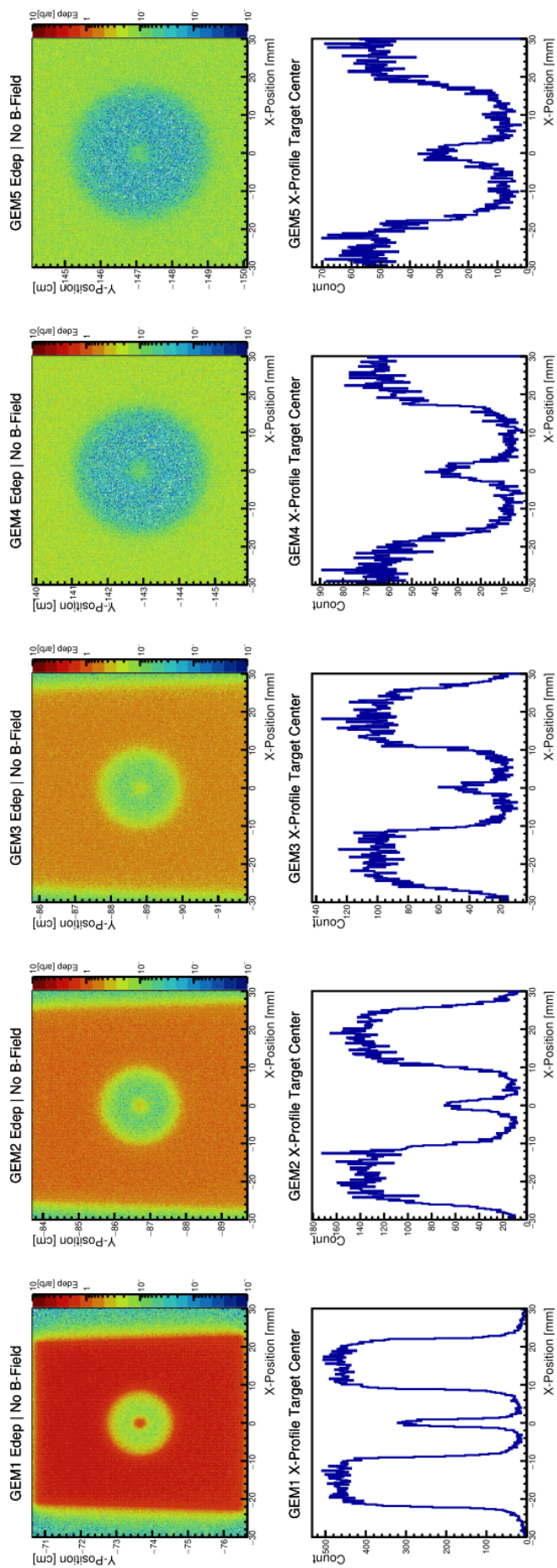


Figure 7.11: Energy deposition by gamma rays produced from beam on Carbon target in the five GEM detectors of the SoLID spectrometer in the PVDIS setup with magnetic field on. A rather clean signal is seen in each GEM.

Chapter 8

Conclusion

Noteworthy improvements were made towards high-precision Møller polarimetry during the PREX-II and CREX experiments and there is remaining work required in order to achieve future experimental goals. Additionally, the results of the PREX-II experiment and subsequent tensions with other measurements opens the door to new thought-provoking questions which will require more experimental data to help paint a more complete and more finely-detailed picture. Below are some concluding remarks.

8.1 Møller Polarimetry

There was particular care made in the controlling of systematic uncertainties in order to exceed the proposed 1.1% systematics goals. The effort undertaken to develop a meticulous understanding of the Møller polarimeter along with the conservative systematics scrutiny for the PREX-II and CREX experiments, in some respects, was done to push the envelope towards the high-precision Møller polarimetry that will be required in the future. Planned PVES experiments such as the Measurement Of a Lepton Lepton Electroweak Reaction (MOLLER) [86]—which will be measuring the weak charge of the electron Q_W^e by measuring the A_{PV} of longitudinally-polarized electrons off of liquid hydrogen target—and future PVDIS experiments with the planned SoLID spectrometer [87] have

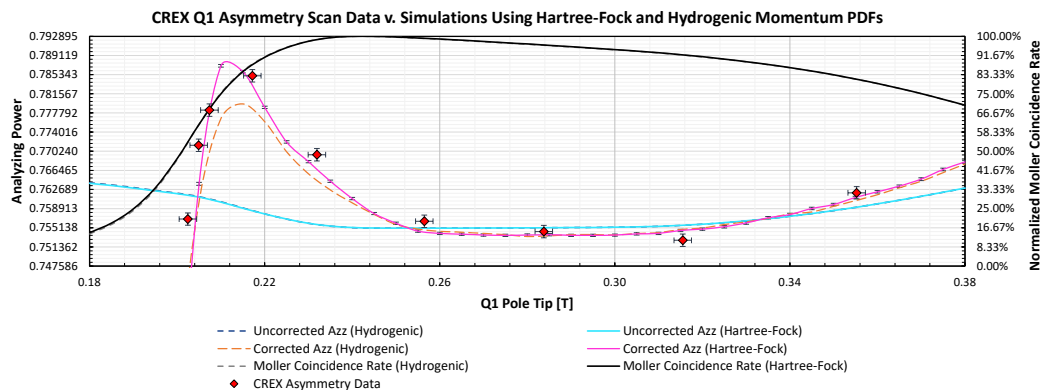


Figure 8.1: Comparison of CREX asymmetry data against simulation results from MolPol using the generally used modified hydrogen wavefunction model (labeled ‘Hydrogenic’ in the graphic above) to generate the momentum spectrum for the bound iron electrons and the momentum spectrum for the bulk-iron electrons generated from Hartree-Fock calculations.

strict polarimetry budgets of 0.45% and 0.4% respectively. As such, our developed methods and keen focus on keeping a tight hand on systematics is paving the way towards future high-precision polarimetry for PVES experiments in Jefferson Lab’s Hall-A.

The following few areas are those which are undergoing improvement, need improvement or which have solutions that simply need to be implemented in the future:

Analyzing Power Levchuk Modeling

The Møller analyzing power systematics for PREX-II table 4.11 and CREX table 4.11 and represent a significant improvement in the understanding of the polarimeter and great progress towards high-precision polarimetry that will be required for future experiments. Improvements on the modeling of the Levchuk Effect section 3.2.1 by utilizing Hartree-Fock generated momentum distributions of the bulk iron electrons. When compared to the CREX asymmetry data taken over a wide spread of magnet detuning the Hartree-Fock modeling shows a dramatic improvement over the long-used Modified Hydrogen modeling.

Bleed through

Bleed through provided an unwelcome 0.2% systematic during the CREX as Hall-C was running a concurrent experiment at a $30\mu\text{A}$ current. Since the polarization of Hall C was

of opposite sign this amplified the issue by a factor of two. In theory, the solution to the bleed through issue requires negotiation and cooperation between Hall-A and Hall-C in the scheduling of Møller polarimetry measurements.

High Current Extrapolation

This is perhaps the most challenging systematic to be studied and is more of an “unsettled concern”. Previous studies performed in Hall-C, data shown in fig. 4.37, have set a maximum limit on this. For future parity-violating experiment requirements a systematic of 0.5% isn’t acceptable within the required systematics budget. In order to settle this concern additional studies, perhaps a repeat of the 2007 Hall-C, will be required.

8.2 Neutron Skin Measurements

The PREX-II experiment results indicate a thicker-than-expected neutron skin; as such, there exists some tension between the PREX-II results and the extrapolated radii of neutron stars (which the PREX-II result would predict under prevailing theoretical assumptions about the extension of the nuclear EOS from nuclei at nuclear saturation all the way up to astrophysical objects). In order to make sense of these tensions additional data will be needed.

On the experimental nuclear physics side, unfortunately, the HRS spectrometers which made the PREX/CREX measurements possible in Jefferson Lab’s Hall A have been decommissioned as the experimental hall transitions towards newer experiments and so the possibility of future neutron skin measurements has evanesced. The next available opportunity to measure the neutron skin of ^{208}Pb will be at the Mainz Energy Recovery Superconducting Accelerator (MESA) which is expected to begin accelerator operations in 2023. One of the experimental units that will be located at the MESA facility is P2 [88]—a PVES-type experiment, which aims to measure $\sin^2 \theta_W$ to a precision of 0.15%. The P2 spectrometer opens the door for new high-precision PVES experiments and within the scope of the P2 experiment is the Mainz Radius Experiment (MREX) which aims

to measure the neutron skin of ^{208}Pb to a precision of 0.52%. The additional neutron skin measurement of ^{208}Pb by MREX will reinforce and further refine the result of the PREX-II experiment.

Appendix A

Polarization Data Summaries

This appendix contains tabled results of grouped Møller polarimetry measurements that were taken for either beam polarization measurements or systematics studies and presented elsewhere in the paper either graphically or brief table.

A.1 PREX-II Spin Dance Results

Summary of Hall A spin dance measurements taken on July 24, 2019 in the commissioning of the PREX-II experiment. Polarization can be extracted using eq. (3.12) with $P_{targ} = 0.08005$. Data shown in left panel of fig. 4.10. The -60° Wien angle data was omitted from the final fit.

Table A.1: Summary of PREX-II Møller polarimetry spin dance measurements taken on July 24, 2019.

Group	Type	Date	Wien Flip	iHWP	Target	A_{zz}	Asymmetry	Asym Error	Wien Angle	χ^2/NDF
1012	spin_dance	2019-07-24	RIGHT	IN	4um	0.77103	0.053634	0.000220	-15.5°	1.06
1013	spin_dance	2019-07-24	RIGHT	IN	4um	0.77103	0.050784	0.000242	$+7^\circ$	1.26
1014	spin_dance	2019-07-24	RIGHT	IN	4um	0.77103	0.039112	0.000230	$+30^\circ$	1.10
1015	spin_dance	2019-07-24	RIGHT	IN	4um	0.77103	0.049956	0.000238	-35°	0.87
1016	spin_dance	2019-07-24	RIGHT	IN	4um	0.77103	0.035077	0.000267	-60°	1.05
1017	spin_dance	2019-07-24	RIGHT	IN	4um	0.77103	0.053863	0.000302	-12.2°	0.97
1018	spin_dance	2019-07-24	RIGHT	IN	4um	0.77103	0.053886	0.000338	-5°	0.89

A.2 CREX Spin Dance Results

Summary of Hall A spin dance measurements taken on January 17, 2020 during the commissioning of the CREX. Polarization can be extracted using eq. (3.12) with $P_{targ} = 0.08005$. Data shown in left panel of fig. 4.10.

Table A.2: Summary of CREX Møller polarimetry spin dance measurements taken on January, 7 2020.

Group	Type	Date	Wien Flip	iHWP	Target	A_{zz}	Asymmetry	Asym Error	Wien Angle	χ^2/NDF
3007	spin_dance	2020-01-07	RIGHT	IN	10um	0.75421	0.052262	0.000119	-26.4°	0.98
3008	spin_dance	2020-01-07	RIGHT	IN	10um	0.75421	0.042874	0.000118	+5°	0.84
3009	spin_dance	2020-01-07	RIGHT	IN	10um	0.75421	0.047004	0.000131	-55°	1.36
3010	spin_dance	2020-01-07	RIGHT	IN	10um	0.75421	0.051584	0.000125	-40°	0.72
3011	spin_dance	2020-01-07	RIGHT	IN	10um	0.75421	0.049168	0.000121	-10°	0.72

A.3 PREX-II Cu Foil Measurements

Summary of copper foil measurements taken during the PREX-II experiment. Polarization can be extracted using eq. (3.12) with $P_{targ} = 0.08005$. Data shown in fig. 4.39.

Table A.3: Summary of PREX-II Møller polarimetry Cu foil null asymmetry measurements.

Group	Type	Date	Wien Flip	iHWP	Target	A_{zz}	Asymmetry	Asym Error	Chi2/NDF
1002	false_asym	2019-07-10	RIGHT	OUT	Cu	0.77103	-0.000474	0.000474	0.81
1011	false_asym	2019-07-18	RIGHT	IN	Cu	0.77103	0.000062	0.000204	0.72
1020	false_asym	2019-07-24	RIGHT	IN	Cu	0.77103	-0.000522	0.000238	0.93
1052	false_asym	2019-08-26	LEFT	IN	Cu	0.77304	-0.000074	0.000130	1.33
1055	false_asym	2019-08-26	LEFT	OUT	Cu	0.77304	-0.000171	0.000123	0.63
1067	false_asym	2019-08-31	LEFT	OUT	Cu	0.77304	0.000005	0.000125	0.92
1068	false_asym	2019-08-31	LEFT	IN	Cu	0.77304	0.000004	0.000124	0.96
1082	false_asym	2019-09-04	LEFT	OUT	Cu	0.77304	-0.000218	0.000143	0.66
1083	false_asym	2019-09-04	LEFT	IN	Cu	0.77304	0.000115	0.000151	0.81
1095	false_asym	2019-09-08	LEFT	IN	Cu	0.77304	-0.000122	0.000169	1.38
1096	false_asym	2019-09-08	LEFT	OUT	Cu	0.77304	0.000031	0.000183	0.94

A.4 CREX Cu Foil Measurements

Summary of copper foil measurements taken during the CREX experiment. Polarization can be extracted using eq. (3.12) with $P_{targ} = 0.08005$. Data shown in fig. 4.39.

Table A.4: Summary of CREX Møller polarimetry Cu foil null asymmetry measurements.

Group	Type	Date	Wien Flip	iHWP	Target	A_{zz}	Asymmetry	Asym Error	Chi2/NDF
3004	false_asym	2019-12-01	RIGHT	IN	Cu	0.75421	-0.000170	0.000143	0.73
3014	false_asym	2020-01-07	RIGHT	OUT	Cu	0.75421	-0.000042	0.000141	1.03
3024	false_asym	2020-02-08	RIGHT	IN	Cu	0.75421	0.000002	0.000120	0.61
3040	false_asym	2020-02-24	LEFT	OUT	Cu	0.75421	0.000183	0.000155	0.99
3047	false_asym	2020-08-19	RIGHT	OUT	Cu	0.75421	-0.000230	0.000149	1.09
3050	false_asym	2020-09-04	RIGHT	IN	Cu	0.75421	-0.000013	0.000183	1.11
3054	false_asym	2020-09-16	RIGHT	IN	Cu	0.75421	0.000160	0.000168	0.98

A.5 Foil Jogging Study

Listed below are results of polarization measurements taken for the $10\mu\text{m}$ and $4\mu\text{m}$ foil jogging systematic study on 9/4/2019. Target ladder was jogged $\pm 2\text{mm}$ off center for both foils. Polarization can be extracted using eq. (3.12) with $P_{\text{targ}} = 0.08005$. Data visualized in fig. 4.16.

Table A.5: Summary of PREX-II Møller polarimetry foil jogging systematic study measurements.

Group	Type	Date	Wien Flip	iHWP	Target	A_{zz}	Asymmetry	Asym Error	Jogged	Chi2/NDF
1080	beam_pol	2019-09-04	LEFT	OUT	10um	0.77304	0.055643	0.000150	Center	0.97
1081	beam_pol_sys	2019-09-04	LEFT	OUT	10um	0.77304	0.055632	0.000146	+2 mm	0.91
1085	beam_pol_sys	2019-09-04	LEFT	OUT	4um	0.77304	0.055677	0.000168	+2 mm	1.12
1086	beam_pol_sys	2019-09-04	LEFT	OUT	4um	0.77304	0.055161	0.000175	Center	1.06
1087	beam_pol_sys	2019-09-04	LEFT	OUT	4um	0.77304	0.055937	0.000195	-2 mm	1.01
1088	beam_pol_sys	2019-09-04	LEFT	OUT	10um	0.77304	0.055898	0.000155	-2 mm	1.59

A.6 PREX-II Asymmetry Scan

Table A.6: Summary of PREX-II Møller polarimetry asymmetry scan measurements taken on 8/10/2019. Percent detuned off of optimal optics setting in shown.

Group	Type	Date	Wien Flip	iHWP	Target	A_{zz}	Asymmetry	Asym Error	Jogged	Chi2/NDF
1030	beam_pol	2019-08-10	LEFT	IN	4um	0.77304	-0.054960	0.000190	—	0.86
1032	beam_pol_sys	2019-08-10	LEFT	IN	4um	0.77382	-0.054801	0.000170	-5%	0.92
1033	beam_pol_sys	2019-08-10	LEFT	IN	4um	0.78328	-0.055774	0.000174	-2%	0.97
1034	beam_pol_sys	2019-08-10	LEFT	IN	4um	0.77380	-0.054844	0.000176	+2%	0.95

A.7 CREX Asymmetry Scan

CREX asymmetry scan data Polarization can be extracted using eq. (3.12) with $P_{targ} = 0.08005$. Data visualized in fig. 4.30.

Table A.7: Summary of CREX Møller polarimetry asymmetry scan measurements taken on 2/8/2020. Percent detuned off of optimal optics setting in shown.

Group	Type	Date	Wien Flip	iHWP	Target	A_{zz}	Asymmetry	Asym Error	Detuned	Chi2/NDF
3023	beam_pol	2020-02-08	RIGHT	IN	10um	0.754210	0.052417	0.000118	—	0.95
3027	beam_pol_sys	2020-02-08	RIGHT	IN	10um	0.762041	0.052914	0.000116	+50.45%	1.06
3028	beam_pol_sys	2020-02-08	RIGHT	IN	10um	0.755203	0.052409	0.000111	+33.45%	0.71
3029	beam_pol_sys	2020-02-08	RIGHT	IN	10um	0.754804	0.052600	0.000102	+8.37%	1.05
3030	beam_pol_sys	2020-02-08	RIGHT	IN	10um	0.764595	0.053536	0.000102	-2.09%	1.06
3031	beam_pol_sys	2020-02-08	RIGHT	IN	10um	0.778045	0.054553	0.000111	-8.37%	0.88
3032	beam_pol_sys	2020-02-08	RIGHT	IN	10um	0.773246	0.054095	0.000127	-12.55%	0.96
3033	beam_pol_sys	2020-02-08	RIGHT	IN	10um	0.757760	0.053572	0.000119	-13.59%	0.85
3034	beam_pol_sys	2020-02-08	RIGHT	IN	10um	0.742275	0.052551	0.000151	-14.64%	0.88

A.8 PREX-II Beam Polarization Measurements

Table summary of all beam polarization measurements taken during the PREX-II experiment. Polarization group measurement 1098 was accidentally grouped with another experiment on 8/31/2019 and assigned its own group number after the experiment had terminated; as such, this measurement group number appears chronologically out of order. Polarization can be extracted using eq. (3.12) with $P_{targ} = 0.08005$. Data graphically shown in figs. 4.11, 4.14, 4.15, 4.17, 4.18 and 4.22.

Table A.8: Summary of PREX-II Moller Polarimetry Group Measurements.

Group	Type	Date	Wien Flip	iHWP	Target	A_{zz}	Asymmetry	Asym Error	Chi2/NDF
1023	beam_pol	2019-08-04	LEFT	IN	4um	0.77304	-0.054571	0.000189	1.42
1024	beam_pol	2019-08-04	LEFT	IN	4um	0.77304	-0.054955	0.000322	1.07
1027	beam_pol	2019-08-04	LEFT	OUT	4um	0.77304	0.055107	0.000244	1.26
1030	beam_pol	2019-08-10	LEFT	IN	4um	0.77304	-0.054960	0.000190	0.86
1031	beam_pol	2019-08-10	LEFT	OUT	4um	0.77304	0.055222	0.000193	0.92
1038	beam_pol	2019-08-18	RIGHT	IN	4um	0.77304	0.054456	0.000181	0.94
1039	beam_pol	2019-08-18	RIGHT	OUT	4um	0.77304	-0.055673	0.000182	1.08
1042	beam_pol	2019-08-21	RIGHT	IN	4um	0.77304	0.054435	0.000177	1.15
1043	beam_pol	2019-08-21	RIGHT	OUT	4um	0.77304	-0.055183	0.000288	1.09
1044	beam_pol	2019-08-21	RIGHT	IN	4um	0.77304	0.054419	0.000291	0.84
1045	beam_pol	2019-08-21	RIGHT	OUT	4um	0.77304	-0.055543	0.000288	1.02
1050	beam_pol	2019-08-26	LEFT	OUT	4um	0.77304	0.055258	0.000181	0.91
1051	beam_pol	2019-08-26	LEFT	IN	4um	0.77304	-0.054525	0.000170	0.96
1053	beam_pol	2019-08-26	LEFT	IN	10um	0.77304	-0.055065	0.000163	1.36
1054	beam_pol	2019-08-26	LEFT	OUT	10um	0.77304	0.056008	0.000173	0.92
1062	beam_pol	2019-08-31	LEFT	OUT	10um	0.77304	0.055751	0.000145	1.03
1063	beam_pol	2019-08-31	LEFT	IN	10um	0.77304	-0.055049	0.000151	1.10
1065	beam_pol	2019-08-31	LEFT	IN	4um	0.77304	-0.054500	0.000169	0.99
1066	beam_pol	2019-08-31	LEFT	OUT	4um	0.77304	0.055015	0.000213	1.04
1070	beam_pol	2019-08-31	LEFT	IN	4um	0.77304	-0.054326	0.000169	1.00
1071	beam_pol	2019-08-31	LEFT	OUT	4um	0.77304	0.055149	0.000166	1.09
1073	beam_pol	2019-08-31	LEFT	OUT	10um	0.77304	0.055662	0.000200	1.21

Table A.8: Summary of PREX-II Moller Polarimetry Group Measurements.

Group	Type	Date	Wien Flip	iHWP	Target	A_{zz}	Asymmetry	Asym Error	Chi2/NDF
1074	beam_pol	2019-08-31	LEFT	OUT	10um	0.77304	0.056172	0.000178	1.16
1077	beam_pol	2019-09-04	LEFT	OUT	4um	0.77304	0.055405	0.000173	0.98
1078	beam_pol	2019-09-04	LEFT	IN	4um	0.77304	-0.054344	0.000170	0.97
1079	beam_pol	2019-09-04	LEFT	IN	10um	0.77304	-0.055017	0.000167	1.26
1080	beam_pol	2019-09-04	LEFT	OUT	10um	0.77304	0.055643	0.000150	0.97
1093	beam_pol	2019-09-08	LEFT	OUT	10um	0.77304	0.055844	0.000146	0.73
1094	beam_pol	2019-09-08	LEFT	IN	10um	0.77304	-0.055149	0.000144	0.97
1097	beam_pol	2019-09-08	LEFT	OUT	4um	0.77304	0.055314	0.000177	1.13
1098	beam_pol	2019-08-31	LEFT	OUT	4um	0.77304	0.055480	0.000272	0.91

A.9 CREX Beam Polarization Measurements

Table summary of all beam polarization measurements taken during the CREX experiment. Polarization can be extracted using eq. (3.12) with $P_{target} = 0.08005$.

Table A.9: Summary of CREX Møller Polarimetry Group Measurements

Group	Type	Date	iHWP	Wien State	A_{zz}	Asymmetry	Asym Error	Chi2/NDF
3002	beam_pol	2019/12/01	OUT	RIGHT	0.75421	-0.052538	0.000123	1.34
3003	beam_pol	2019/12/01	IN	RIGHT	0.75421	0.052314	0.000114	0.72
3012	beam_pol	2020/01/07	IN	RIGHT	0.75421	0.052529	0.000115	1.12
3013	beam_pol	2020/01/07	OUT	RIGHT	0.75421	-0.052433	0.000116	0.80
3017	beam_pol	2020/01/27	IN	RIGHT	0.75421	0.052160	0.000100	0.93
3019	beam_pol	2020/01/27	OUT	RIGHT	0.75421	-0.052589	0.000303	1.19
3022	beam_pol	2020/02/08	OUT	RIGHT	0.75421	-0.052512	0.000122	0.79
3023	beam_pol	2020/02/08	IN	RIGHT	0.75421	0.052417	0.000118	0.95
3038	beam_pol	2020/02/24	IN	LEFT	0.75421	-0.052067	0.000098	0.72
3039	beam_pol	2020/02/24	OUT	LEFT	0.75421	0.052396	0.000097	0.94
3042	beam_pol	2020/03/18	OUT	LEFT	0.75421	0.052573	0.000140	0.83
3045	beam_pol	2020/08/19	IN	RIGHT	0.75421	0.052780	0.000120	0.91
3046	beam_pol	2020/08/19	OUT	RIGHT	0.75421	-0.052933	0.000119	0.92
3048	beam_pol	2020/09/04	OUT	RIGHT	0.75421	-0.052794	0.000095	0.80
3049	beam_pol	2020/09/04	IN	RIGHT	0.75421	0.052818	0.000100	0.92
3052	beam_pol	2020/09/16	OUT	RIGHT	0.75421	-0.052899	0.000110	0.89
3053	beam_pol	2020/09/16	IN	RIGHT	0.75421	0.052591	0.000106	1.11

Bibliography

Cited References

- [1] J. J. Thomson M.A. F.R.S. “XL. Cathode Rays”. In: *The London, Edinburgh, and Dublin Philosophical Magazine and Journal of Science* 44.269 (1897), pp. 293–316. DOI: 10.1080/14786449708621070.
- [2] J.J. Thomson F.R.S. “XXIV. On the structure of the atom: an investigation of the stability and periods of oscillation of a number of corpuscles arranged at equal intervals around the circumference of a circle; with application of the results to the theory of atomic structure”. In: *The London, Edinburgh, and Dublin Philosophical Magazine and Journal of Science* 7.39 (1904), pp. 237–265. DOI: 10.1080/14786440409463107.
- [3] Professor E. Rutherford F.R.S. “LXXIX. The scattering of α and β particles by matter and the structure of the atom”. In: *The London, Edinburgh, and Dublin Philosophical Magazine and Journal of Science* 21.125 (1911), pp. 669–688. DOI: 10.1080/14786440508637080.
- [4] Sir Ernest Rutherford F.R.S. “LVII. The structure of the atom”. In: *The London, Edinburgh, and Dublin Philosophical Magazine and Journal of Science* 27.159 (1914), pp. 488–498. DOI: 10.1080/14786440308635117.
- [5] N. Bohr Dr. phil. “I. On the constitution of atoms and molecules”. In: *The London, Edinburgh, and Dublin Philosophical Magazine and Journal of Science* 26.151 (1913), pp. 1–25. DOI: 10.1080/14786441308634955.

- [6] Professor Sir E. Rutherford F.R.S. “LIV. Collision of α particles with light atoms. IV. An anomalous effect in nitrogen”. In: *The London, Edinburgh, and Dublin Philosophical Magazine and Journal of Science* 37.222 (1919), pp. 581–587. DOI: 10.1080/14786440608635919.
- [7] E. Schrödinger. “Quantisierung als Eigenwertproblem”. In: *Annalen der Physik* 384.4 (1926), pp. 361–376. DOI: 10.1002/andp.19263840404.
- [8] James Chadwick. “The existence of a neutron”. In: *Proceedings of the Royal Society of London. Series A, Containing Papers of a Mathematical and Physical Character* 136.830 (June 1932), pp. 692–708. DOI: 10.1098/rspa.1932.0112.
- [9] E. Rutherford M.A. B.Sc. “VIII. Uranium radiation and the electrical conduction produced by it”. In: *The London, Edinburgh, and Dublin Philosophical Magazine and Journal of Science* 47.284 (1899), pp. 109–163. DOI: 10.1080/14786449908621245.
- [10] Thaddeus J. Trenn. “Rutherford on the Alpha-Beta-Gamma Classification of Radioactive Rays”. In: *Isis* 67.1 (1976), pp. 61–75. ISSN: 00211753, 15456994.
- [11] G. Gamow. “Zur Quantentheorie des Atomkernes”. In: *Zeitschrift für Physik* 51.3-4 (Mar. 1928), pp. 204–212. DOI: 10.1007/bf01343196.
- [12] Enrico Fermi. “Tentativo di una Teoria Dei Raggi β ”. In: *Il Nuovo Cimento* 11.1 (Jan. 1934), pp. 1–19. DOI: 10.1007/bf02959820.
- [13] Fred L. Wilson. “Fermi’s Theory of Beta Decay”. In: *American Journal of Physics* 36.12 (Dec. 1968), pp. 1150–1160. DOI: 10.1119/1.1974382.
- [14] E. Noether. “Invariante Variationsprobleme”. ger. In: *Nachrichten von der Gesellschaft der Wissenschaften zu Göttingen, Mathematisch-Physikalische Klasse* 1918 (1918), pp. 235–257.
- [15] T. D. Lee and C. N. Yang. “Question of Parity Conservation in Weak Interactions”. In: *Phys. Rev.* 104 (1 Oct. 1956), pp. 254–258. DOI: 10.1103/PhysRev.104.254.
- [16] C. S. Wu et al. “Experimental Test of Parity Conservation in Beta Decay”. In: *Phys. Rev.* 105 (4 Feb. 1957), pp. 1413–1415. DOI: 10.1103/PhysRev.105.1413.

- [17] Blecknehaus—Wikimedia Commons. *Principle of the Wu Experiment*. URL: [https://en.wikipedia.org/wiki/File:Parity_violation_principle_Wu_experiment_\(English\).jpg](https://en.wikipedia.org/wiki/File:Parity_violation_principle_Wu_experiment_(English).jpg).
- [18] Sheldon L. Glashow. “Partial-Symmetries of Weak Interactions”. In: *Nuclear Physics* 22.4 (1961), pp. 579–588. ISSN: 0029-5582. DOI: [https://doi.org/10.1016/0029-5582\(61\)90469-2](https://doi.org/10.1016/0029-5582(61)90469-2).
- [19] Steven Weinberg. “A Model of Leptons”. In: *Phys. Rev. Lett.* 19 (21 Nov. 1967), pp. 1264–1266. DOI: [10.1103/PhysRevLett.19.1264](https://doi.org/10.1103/PhysRevLett.19.1264).
- [20] Abdus Salam. “Weak and Electromagnetic Interactions”. In: *Conf. Proc. C 680519* (1968), pp. 367–377. DOI: [10.1142/9789812795915_{_}0034](https://doi.org/10.1142/9789812795915_{_}0034).
- [21] Peter W. Higgs. “Broken Symmetries and the Masses of Gauge Bosons”. In: *Phys. Rev. Lett.* 13 (16 Oct. 1964), pp. 508–509. DOI: [10.1103/PhysRevLett.13.508](https://doi.org/10.1103/PhysRevLett.13.508).
- [22] M. Tanabashi et al. “Review of Particle Physics”. In: *Phys. Rev. D* 98 (3 Aug. 2018), p. 030001. DOI: [10.1103/PhysRevD.98.030001](https://doi.org/10.1103/PhysRevD.98.030001).
- [23] “Observation of single isolated electrons of high transverse momentum in events with missing transverse energy at the CERN pp collider”. In: *Physics Letters B* 122.5 (1983), pp. 476–485. ISSN: 0370-2693. DOI: [https://doi.org/10.1016/0370-2693\(83\)91605-2](https://doi.org/10.1016/0370-2693(83)91605-2).
- [24] “Experimental observation of isolated large transverse energy electrons with associated missing energy at s=540 GeV”. In: *Physics Letters B* 122.1 (1983), pp. 103–116. ISSN: 0370-2693. DOI: [https://doi.org/10.1016/0370-2693\(83\)91177-2](https://doi.org/10.1016/0370-2693(83)91177-2).
- [25] F.J. Hasert et al. “Observation of neutrino-like interactions without muon or electron in the gargamelle neutrino experiment”. In: *Physics Letters B* 46.1 (1973), pp. 138–140. ISSN: 0370-2693. DOI: [https://doi.org/10.1016/0370-2693\(73\)90499-1](https://doi.org/10.1016/0370-2693(73)90499-1).
- [26] F.J. Hasert et al. “Search for elastic muon-neutrino electron scattering”. In: *Physics Letters B* 46.1 (1973), pp. 121–124. ISSN: 0370-2693. DOI: [https://doi.org/10.1016/0370-2693\(73\)90494-2](https://doi.org/10.1016/0370-2693(73)90494-2).

- [27] C.Y. Prescott et al. “Parity non-conservation in inelastic electron scattering”. In: *Physics Letters B* 77.3 (1978), pp. 347–352. ISSN: 0370-2693. DOI: [https://doi.org/10.1016/0370-2693\(78\)90722-0](https://doi.org/10.1016/0370-2693(78)90722-0).
- [28] MissMJ—Wikimedia Commons. *Standard Model of Elementary Particles*. URL: https://en.wikipedia.org/wiki/File:Standard_Model_of_Elementary_Particles.svg.
- [29] H. De Vries, C.W. De Jager, and C. De Vries. “Nuclear charge-density-distribution parameters from elastic electron scattering”. In: *Atomic Data and Nuclear Data Tables* 36.3 (1987), pp. 495–536. ISSN: 0092-640X. DOI: [https://doi.org/10.1016/0092-640X\(87\)90013-1](https://doi.org/10.1016/0092-640X(87)90013-1).
- [30] G. W. Greenless, G. J. Pyle, and Y. C. Tang. “Physical Significance of Optical-Model Parameters”. In: *Phys. Rev. Lett.* 17 (1 July 1966), pp. 33–36. DOI: 10.1103/PhysRevLett.17.33.
- [31] Shufang Ban, C J Horowitz, and R Michaels. “Parity violating electron scattering measurements of neutron densities”. In: *Journal of Physics G: Nuclear and Particle Physics* 39.1 (Nov. 2011), p. 015104. DOI: 10.1088/0954-3899/39/1/015104.
- [32] M Thiel et al. “Neutron skins of atomic nuclei: per aspera ad astra”. In: *Journal of Physics G: Nuclear and Particle Physics* 46.9 (Aug. 2019), p. 093003. DOI: 10.1088/1361-6471/ab2c6d.
- [33] T.W. Donnelly, J. Dubach, and Ingo Sick. “Isospin dependences in parity-violating electron scattering”. In: *Nuclear Physics A* 503.3 (1989), pp. 589–631. ISSN: 0375-9474. DOI: [https://doi.org/10.1016/0375-9474\(89\)90432-6](https://doi.org/10.1016/0375-9474(89)90432-6).
- [34] C. J. Horowitz et al. “Parity violating measurements of neutron densities”. In: *Phys. Rev. C* 63.2 (2 Jan. 2001), p. 025501. ISSN: 1089490X. DOI: 10.1103/PhysRevC.63.025501. arXiv: 1010.3246.
- [35] C. J. Horowitz. “Parity violating elastic electron scattering and Coulomb distortions”. In: *Phys. Rev. C* 57 (6 June 1998), pp. 3430–3436. DOI: 10.1103/PhysRevC.57.3430.

- [36] C. J. Horowitz and J. Piekarewicz. “Neutron Star Structure and the Neutron Radius of ^{208}Pb ”. In: *Phys. Rev. Lett.* 86 (25 June 2001), pp. 5647–5650. DOI: 10.1103/PhysRevLett.86.5647.
- [37] The Jefferson Lab Qweak Collaboration. “Precision measurement of the weak charge of the proton”. In: *Nature* 557.7704 (May 2018), pp. 207–211. DOI: 10.1038/s41586-018-0096-0.
- [38] C. J. Horowitz, J. Piekarewicz, and Brendan Reed. “Insights into nuclear saturation density from parity-violating electron scattering”. In: *Phys. Rev. C* 102 (4 Oct. 2020), p. 044321. DOI: 10.1103/PhysRevC.102.044321.
- [39] C. J. Horowitz and J. Piekarewicz. “Neutron radii of ^{208}Pb and neutron stars”. In: *Phys. Rev. C* 64 (6 Nov. 2001), p. 062802. DOI: 10.1103/PhysRevC.64.062802.
- [40] James M. Lattimer. “The Nuclear Equation of State and Neutron Star Masses”. In: *Annual Review of Nuclear and Particle Science* 62.1 (2012), pp. 485–515. DOI: 10.1146/annurev-nucl-102711-095018. eprint: <https://doi.org/10.1146/annurev-nucl-102711-095018>.
- [41] B. Alex Brown. “Neutron Radii in Nuclei and the Neutron Equation of State”. In: *Phys. Rev. Lett.* 85 (25 Dec. 2000), pp. 5296–5299. DOI: 10.1103/PhysRevLett.85.5296.
- [42] James M. Lattimer and Madappa Prakash. “The equation of state of hot, dense matter and neutron stars”. In: *Physics Reports* 621 (2016). Memorial Volume in Honor of Gerald E. Brown, pp. 127–164. ISSN: 0370-1573. DOI: <https://doi.org/10.1016/j.physrep.2015.12.005>.
- [43] James M. Lattimer and Madappa Prakash. “Nuclear matter and its role in supernovae, neutron stars and compact object binary mergers”. In: *Physics Reports* 333-334 (2000), pp. 121–146. ISSN: 0370-1573. DOI: [https://doi.org/10.1016/S0370-1573\(00\)00019-3](https://doi.org/10.1016/S0370-1573(00)00019-3).

- [44] X Roca-Maza et al. “Neutron Skin of Pb^{208} , Nuclear Symmetry Energy, and the Parity Radius Experiment”. In: *Physical Review Letters* 106.25 (2011). DOI: 10.1103/PhysRevLett.106.252501. arXiv: 1103.1762.
- [45] Douglas W. Higinbotham. “Using Polarimetry To Determine The CEBAF Beam Energy ”. In: *Proceedings of XVth International Workshop on Polarized Sources, Targets, and Polarimetry — PoS(PSTP2013)*. Vol. 182. 2014, p. 014. DOI: 10.22323/1.182.0014.
- [46] Daniel T. Pierce and Felix Meier. “Photoemission of spin-polarized electrons from GaAs”. In: *Phys. Rev. B* 13 (12 June 1976), pp. 5484–5500. DOI: 10.1103/PhysRevB.13.5484.
- [47] K. D. Paschke. “Controlling helicity-correlated beam asymmetries in a polarized electron source”. In: *The European Physical Journal A* 32.4 (June 2007), pp. 549–553. DOI: 10.1140/epja/i2006-10442-8.
- [48] G.D. Cates et al. “The bates polarized electron source”. In: *Nuclear Instruments and Methods in Physics Research Section A: Accelerators, Spectrometers, Detectors and Associated Equipment* 278.2 (1989), pp. 293–317. ISSN: 0168-9002. DOI: [https://doi.org/10.1016/0168-9002\(89\)90846-2](https://doi.org/10.1016/0168-9002(89)90846-2).
- [49] D.W. Higinbotham and T. Keppel for the Hall A Collaboration. *2017 Version: Jefferson Lab Hall A Standard Equipment Manual*. Last accessed on 7-14-2021. URL: <https://hallaweb.jlab.org/github/halla-osp/version/Standard-Equipment-Manual.pdf>.
- [50] G. A. Krafft et al. “Measuring and Controlling the Energy Spread in CEBAF”. In: (2000). eprint: arXiv:physics/0009087.
- [51] R. Dickson and V. Lebedev. “Fast feedback system for energy and beam stabilization”. In: *Conf. Proc. C* 991004 (1999). Ed. by D. Bulfone and A. Daneels, pp. 245–247.

- [52] J.L. McCarter et al. “A low-voltage retarding-field Mott polarimeter for photocathode characterization”. In: *Nuclear Instruments and Methods in Physics Research Section A: Accelerators, Spectrometers, Detectors and Associated Equipment* 618.1 (2010), pp. 30–36. ISSN: 0168-9002. DOI: <https://doi.org/10.1016/j.nima.2010.02.123>.
- [53] T. J. Gay and F. B. Dunning. “Mott electron polarimetry”. In: *Review of Scientific Instruments* 63.2 (1992), pp. 1635–1651. DOI: 10.1063/1.1143371. eprint: <https://doi.org/10.1063/1.1143371>.
- [54] Nicolas Falletto et al. “Compton scattering off polarized electrons with a high-finesse Fabry-Perot Cavity at Jlab”. In: *Nuclear Instruments and Methods in Physics Research Section A* 459.3 (Mar. 2001).
- [55] J. Alcorn et al. “Basic instrumentation for Hall A at Jefferson Lab”. In: *Nuclear Instruments and Methods in Physics Research Section A: Accelerators, Spectrometers, Detectors and Associated Equipment* 522.3 (2004), pp. 294–346. ISSN: 0168-9002. DOI: <https://doi.org/10.1016/j.nima.2003.11.415>.
- [56] Jens Erler et al. “Weak Polarized Electron Scattering”. In: *Annual Review of Nuclear and Particle Science* 64.1 (2014), pp. 269–298. DOI: 10.1146/annurev-nucl-102313-025520. eprint: <https://doi.org/10.1146/annurev-nucl-102313-025520>.
- [57] H. Frauenfelder et al. “Parity and Electron Polarization: Møller Scattering”. In: *Phys. Rev.* 107 (2 July 1957), pp. 643–644. DOI: 10.1103/PhysRev.107.643.
- [58] P. S. Cooper et al. “Polarized Electron-Electron Scattering at GeV Energies”. In: *Phys. Rev. Lett.* 34 (25 June 1975), pp. 1589–1592. DOI: 10.1103/PhysRevLett.34.1589.
- [59] A. V. Glamazdin et al. “Electron Beam Møller Polarimeter at Jlab Hall a”. In: (1999). eprint: [arXiv:hep-ex/9912063](https://arxiv.org/abs/hep-ex/9912063).
- [60] Donald Jones. *Target Foil Polarization for Møller Polarimetry in Hall A*. Internal working group tech note. Last Accessed: 7/20/2021. Sept. 2017.

- [61] Christian Møller. “Zur Theorie des Durchgangs schneller Elektronen durch Materie”. In: *Annalen der Physik* 406.5 (1932), pp. 531–585. DOI: <https://doi.org/10.1002/andp.19324060506>. eprint: <https://onlinelibrary.wiley.com/doi/pdf/10.1002/andp.19324060506>.
- [62] M. Swartz et al. “Observation of target electron momentum effects in single-arm Møller polarimetry”. In: *Nuclear Instruments and Methods in Physics Research Section A: Accelerators, Spectrometers, Detectors and Associated Equipment* 363.3 (1995), pp. 526–537. ISSN: 0168-9002. DOI: [https://doi.org/10.1016/0168-9002\(95\)00384-3](https://doi.org/10.1016/0168-9002(95)00384-3).
- [63] L.G. Levchuk. “The intra-atomic motion of bound electrons as a possible source of the systematic error in electron beam polarization measurements by means of a Möller polarimeter”. In: *Nuclear Instruments and Methods in Physics Research Section A: Accelerators, Spectrometers, Detectors and Associated Equipment* 345.3 (1994), pp. 496–499. ISSN: 0168-9002. DOI: [https://doi.org/10.1016/0168-9002\(94\)90505-3](https://doi.org/10.1016/0168-9002(94)90505-3).
- [64] James P. Alexander et al. “Radiative corrections to the Z^0 resonance”. In: *Phys. Rev. D* 37 (1 Jan. 1988), pp. 56–70. DOI: [10.1103/PhysRevD.37.56](https://doi.org/10.1103/PhysRevD.37.56).
- [65] “PRECISION MØLLER POLARIMETRY AND APPLICATIONS AT JEFFERSON LABORATORY”. 2019. DOI: [doi:10.2172/1574104](https://doi.org/10.2172/1574104).
- [66] Joe Grames. *Status update...busy morning*. Last Accessed: 3/13/2021. 2019. URL: <https://logbooks.jlab.org/entry/3729120>.
- [67] Ciprian Gal. *Mott Polarimeter summary and results*. Last Accessed: 3/13/2021. 2019. URL: <https://logbooks.jlab.org/entry/3722467>.
- [68] Caryn Palatchi. *PITA "scan" Moller/Parity*. Last accessed: 8/1/2021. URL: <https://logbooks.jlab.org/entry/3721958>.
- [69] M. Poelker et al. “Generation of electron bunches at low repetition rates using a beat-frequency technique”. In: *Phys. Rev. ST Accel. Beams* 10 (5 May 2007), p. 053502. DOI: [10.1103/PhysRevSTAB.10.053502](https://doi.org/10.1103/PhysRevSTAB.10.053502).

- [70] Donald Charles Jones. *Polarization dependence on slit and current from 2007 and 2009 studies*. Last accessed: 7/16/2021. URL: [methodhttps://hallcweb.jlab.org/elogs/Hall+A+Moller/201012%7B%5C_%7D112112/Polarization%7B%5C_%7Ddependence%7B%5C_%7Don%7B%5C_%7Dslit%7B%5C_%7Dand%7B%5C_%7Dcurrent.pdf](https://hallcweb.jlab.org/elogs/Hall+A+Moller/201012%7B%5C_%7D112112/Polarization%7B%5C_%7Ddependence%7B%5C_%7Don%7B%5C_%7Dslit%7B%5C_%7Dand%7B%5C_%7Dcurrent.pdf).
- [71] Donald Charles Jones. *Null asymmetry for PREX-2*. Last Accessed: 5/20/2021. 2020. URL: <https://hallcweb.jlab.org/elogs/Hall+A+Moller/166>.
- [72] Donald Charles Jones. *Null asymmetry (Cu foil) for CREX*. Last Accessed: 5/20/2021. 2020. URL: <https://hallcweb.jlab.org/elogs/Hall+A+Moller/188>.
- [73] Donald Charles Jones. *Møller Polarimetry Systematic Error from PITA Feedback*. Last accessed 8-1-2021. URL: https://hallcweb.jlab.org/elogs/Hall+A+Moller/201016_123149/PITAsystematic.pdf.
- [74] Donald Charles Jones. *Moller Polarimetry PITA Systematic Uncertainty for CREX*. Last accessed: 7/16/2021. URL: [https://hallcweb.jlab.org/elogs/Hall+A+Moller/201102_125202/Moller_Polarimetry_PITA_Systematic_Uncertainty_for_CREX\(1\).pdf](https://hallcweb.jlab.org/elogs/Hall+A+Moller/201102_125202/Moller_Polarimetry_PITA_Systematic_Uncertainty_for_CREX(1).pdf).
- [75] D. Adhikari et al. “Accurate Determination of the Neutron Skin Thickness of ^{208}Pb through Parity-Violation in Electron Scattering”. In: *Phys. Rev. Lett.* 126.17 (2021), p. 172502. DOI: 10.1103/PhysRevLett.126.172502. arXiv: 2102.10767 [nucl-ex].
- [76] Siyu Jian. *HRS Calibration for PRex-II experiment*. Internal collaboration document.
- [77] Tao Ye. *Calibrating the Sensitivity of High-rate Asymmetry Measurements to Beam Motion*. Last accessed: 6/1/2021. URL: <https://prex.jlab.org/cgi-bin/DocDB/private/ShowDocument?docid=478>.
- [78] E. D. Cooper and C. J. Horowitz. “Vector analyzing power in elastic electron-nucleus scattering”. In: *Phys. Rev. C* 72 (3 Sept. 2005), p. 034602. DOI: 10.1103/PhysRevC.72.034602.

- [79] Weibin Zhang. *Transverse Asymmetry Measurement in PREX-II and CREX*. APS April 2021 Meeting. Last accessed 6/21/2021.
- [80] Devi Lal Adhikari. *Diamond Dilution Correction for PREX-2 and CREX Transverse Data*. Internal tech note. Feb. 2021.
- [81] Brendan T. Reed et al. “Implications of PREX-2 on the Equation of State of Neutron-Rich Matter”. In: *Phys. Rev. Lett.* 126 (17 Apr. 2021), p. 172503. DOI: 10.1103/PhysRevLett.126.172503.
- [82] Zhen Zhang and Lie-Wen Chen. “Electric dipole polarizability in ^{208}Pb as a probe of the symmetry energy and neutron matter around $\rho_0/3$ ”. In: *Phys. Rev. C* 92 (3 Sept. 2015), p. 031301. DOI: 10.1103/PhysRevC.92.031301.
- [83] J. Piekarewicz. “Implications of PREX-2 on the electric dipole polarizability of neutron-rich nuclei”. In: *Phys. Rev. C* 104 (2 Aug. 2021), p. 024329. DOI: 10.1103/PhysRevC.104.024329.
- [84] Gregory Prigozhin et al. “NICER instrument detector subsystem: description and performance”. In: *Space Telescopes and Instrumentation 2016: Ultraviolet to Gamma Ray*. Ed. by Jan-Willem A. den Herder, Tadayuki Takahashi, and Marshall Bautz. SPIE, July 2016. DOI: 10.1117/12.2231718.
- [85] M. C. Miller et al. “PSR J0030+0451 Mass and Radius from NICER Data and Implications for the Properties of Neutron Star Matter”. In: *The Astrophysical Journal* 887.1 (Dec. 2019), p. L24. DOI: 10.3847/2041-8213/ab50c5.
- [86] MOLLER Collaboration et al. *The MOLLER Experiment: An Ultra-Precise Measurement of the Weak Mixing Angle Using Møller Scattering*. 2014. eprint: arXiv:1411.4088.
- [87] P. A. Souder. “Precision Measurement of Parity-violation in Deep Inelastic Scattering Over a Broad Kinematic Range, PAC 34 PR-09-012”. In: ().

- [88] Dominik Becker et al. “The P2 experiment: A future high-precision measurement of the weak mixing angle at low momentum transfer”. In: *European Physical Journal. A* 54.11 (Nov. 2018). DOI: 10.1140/epja/i2018-12611-6.
- [89] J. P. Chen et al. *A White Paper on SoLID (Solenoidal Large Intensity Device)*. 2014. eprint: arXiv:1409.7741.
- [90] Fabio Sauli. “The gas electron multiplier (GEM): Operating principles and applications”. In: *Nuclear Instruments and Methods in Physics Research Section A: Accelerators, Spectrometers, Detectors and Associated Equipment* 805 (2016). Special Issue in memory of Glenn F. Knoll, pp. 2–24. ISSN: 0168-9002. DOI: <https://doi.org/10.1016/j.nima.2015.07.060>.
- [91] Pisin Chen and Spencer Klein. “The Landau-Pomeranchuk-Migdal effect and suppression of beamstrahlung and Bremsstrahlung in linear colliders”. In: *AIP Conference Proceedings* (1992). DOI: 10.1063/1.44055.
- [92] A. Mangiarotti et al. “Implementation of the LPM effect in the discrete-bremsstrahlung simulation of GEANT 3 and GEANT 4”. In: *Nuclear Instruments and Methods in Physics Research Section B: Beam Interactions with Materials and Atoms* 266.23 (2008), pp. 5013–5019. DOI: 10.1016/j.nimb.2008.09.009.

Vita

Name of Author

[David] Eric King Jr.

Degrees Awarded

- M.S. Computational Science (2015), Stockton University, Pomona, NJ
- B.S. Applied Physics (2013), Stockton University, Pomona, NJ

Teaching History

- Physics II (Calc), T.A. Recitation, Fall 2016, Syracuse University
- Physics II (Calc), T.A. Recitation, Summer-2 2016, Syracuse University
- Physics I Lab, Instructor, Summer-1 2016, Syracuse University
- Physics I Lab, T.A. Laboratory, Spring 2016, Syracuse University
- Physics I Lab, T.A. Laboratory, Fall 2015, Syracuse University
- Physics I Lab, Instructor, Spring 2015, Stockton University
- Physics I Lab, Instructor, Fall 2014, Stockton University

Conferences & Talks

- **Challenges to Reaching High-Precision 0.4 % Møller Polarimetry in Hall A at Jefferson Lab for 12 GeV Experimentation.** (2021). Fall 2021 Meeting of the Division of Nuclear Physics of the American Physical Society

- **A path to $\pm 0.4\%$ High-Precision Møller Polarimetry in Hall A at Jefferson Lab During the 12 GeV Era.** (2021). Spring 2021 Meeting of the Division of Nuclear Physics of the American Physical Society
- **Møller Polarimetry in Hall-A Jefferson Lab.** (2021). Jefferson Lab Hall-A Winter 2021 Collaboration Meeting.
- **Key Møller Polarimetry Systematics for the PREX-II/CREX Experiments.** (2020). Fall 2020 Meeting of the Division of Nuclear Physics of the American Physical Society
- **Møller Polarimetry Simulation for Jefferson Lab Hall A.** (2019). PSTP 2019: The 18th International Workshop on Polarized Sources, Targets, and Polarimetry
- **Møller Polarimetry—CREX Optic Options for Our Upcoming Running.** (2019). PREX-II/CREX Collaboration Meeting October 2019.
- **Møller Polarimetry—Optics for PREX.** (2019). PREX-II/CREX February 2019 Collaboration Meeting.

Publications — Author

- The PREX and CREX Collaborations. **New Measurements of the Beam-Normal Single Spin Asymmetry in Elastic Electron Scattering Over a Range of Spin-0 Nuclei.**
 - Timounay, Y., Hartwell, A.R. He, M., King D.E, Murphy, L.K., Demery, V. & Paulsen J.D. (2021). **Sculpting Liquids with Ultrathin Shells.**
DOI:10.1103/PhysRevLett.127.108002
 - The PREX Collaboration. (2021). **An Accurate Determination of the Neutron Skin Thickness of ^{208}Pb through Parity-Violation in Electron Scattering**
DOI:10.1103/PhysRevLett.126.172502

Publications — External Contributor

- MARATHON Collaboration. (2021). **Measurement of the Nucleon F_2^n/F_2^p Structure Function Ratio by the Jefferson Lab MARATHON Tritium/Helium-3 Deep Inelastic Scattering Experiment.** arXiv: 2104.05850 [hep-ex]

- Jefferson Lab Hall A Tritium Collaboration. (2020). **Probing Few-Body Nuclear Dynamics via H3 and He3 (e,e'p) pn Cross-Section Measurements.**

DOI:10.1103/physrevlett.124.212501

- Jefferson Lab Hall A Tritium Collaboration. (2020). **Comparing proton momentum distributions in A=2 and 3 nuclei via ^2H ^3H and ^3He ($e, e'p$) measurements.**

DOI:10.1016/j.physletb.2019.134890